INPUT-OUTPUT ANALYSIS OF HIGH-SPEED TURBULENT JET NOISE

A THESIS

SUBMITTED TO THE FACULTY OF THE GRADUATE SCHOOL

OF THE UNIVERSITY OF MINNESOTA

BY

Jinah Jeun

IN PARTIAL FULFILLMENT OF THE REQUIREMENTS

FOR THE DEGREE OF

DOCTOR OF PHILOSOPHY

Joseph W. Nichols, Advisor

June, 2018

Acknowledgements

First and foremost, I would like to express my special appreciation and thanks to my advisor, Professor Joseph Nichols for his guidance, support, patience, and encouragement throughout my studies. He was always an enthusiastic, accessible, and caring mentor during the entire years of my graduate program, and none of this work would have been possible without his help. His deep understanding of fluids and passion for research gave me an inspiration for my work and has driven me to keep pursuing a dream of being a better researcher. I have been indeed lucky to have an opportunity to work with him.

I would like to extend my sincere gratitude to my committee members, Professors Maziar Hemati, Mihailo Jovanović, and Ellen Longmire. I would also like to thank Professor Graham Candler for serving on my doctoral preliminary oral examination committee and for reviewing my dissertation. They all provided me with invaluable comments to improve my research and dissertation.

Computing resources for high-fidelity simulations were provided by the United States Army Engineer Research and Development Center (ERDC) and the United States Air Force Research Laboratory (AFRL) supercomputing centers. Also, I would like to acknowledge partial financial support from the Amelia Earhart Fellowship.

Lastly, I am forever grateful to my family, Haewoon Jeun, Bogrye Lee, and Jinu Jeun, to whom my dissertation is dedicated, for their endless love and support.

To my family

Abstract

We use input-output analysis to predict and understand the aeroacoustics of high-speed turbulent jets. We consider linear perturbations about Reynolds-averaged Navier-Stokes (RANS) solutions of ideally expanded, axisymmetric, compressible turbulent jets under various operating conditions. For jet noise, a key aspect of our method is the ability to spatially separate near-field input forcing (driven by nonlinear turbulence) from far-field acoustic output. Precisely the same idea, namely the separation of sources and outputs, forms the basis of traditional acoustic analogies. Different from the usual statistical descriptions of the acoustic source terms, input-output analysis provides a dynamical description based on modes correlated over significant distances within the flow. Specifically, we compute optimal and sub-optimal harmonic forcing functions and their corresponding linear responses governed either by the linearized Euler equations (LEE) or by the linearized Navier-Stokes (LNS) equations, using singular value decomposition of the resolvent operator. For supersonic jets, the optimal response closely resembles a wavepacket in both the near-field and the far-field such as those obtained by the parabolized stability equations (PSE), and this mode dominates the response. For subsonic jets, however, the singular values indicate that the contributions of sub-optimal modes to noise generation are nearly equal to that of the optimal mode, explaining why the PSE do not fully capture the far-field sound in this case. Furthermore, we utilize a

high-fidelity large-eddy simulation (LES) data to assess the prevalence of sub-optimal modes in the unsteady data. By projecting the LES source term data onto input modes and the LES acoustic far-field onto output modes, respectively, we demonstrate that sub-optimal modes of both types are physically relevant.

Far-field acoustics generated from turbulent jets are further modeled, using a Ffowcs Williams-Hawkings (FW-H) solver implemented directly within linear input-output analysis framework. Our hybrid input-output/FW-H method efficiently connects input fluctuations embedded in the jet turbulence to pressure outputs in the far-field, and recovers a significant portion of the LES acoustic energy. By repeating input-output analysis over a wide range of frequencies, we find that the far-field acoustic spectra broaden with increasing the radiation angles, as observed in experiments.

To distill acoustically relevant sources, input forcings are further restricted by introducing a new weighting matrix, which selects forcing functions only in the region that contains high turbulent kinetic energy (TKE). We then find that input modes correspond exactly to wavepackets with asymmetric pseudo-Gaussian envelope functions. Furthermore, wavepackets obtained by input-output analysis collapse to a single shape when scaled by $St^{-0.5}$, where St is the jet Strouhal number. This explains the success of recent theoretical models based on stochastic similarity wavepackets.

Contents

List of Tables

List of Figures

Chapter 1

Introduction

1.1 Motivation

Noise reduction is now an important design parameter in the research and development of aircraft. The rapid growth of global aviation industry, from the development of high-performance military aircraft to the increase of civil aircraft traffic, has drawn public awareness to noise pollution from aircraft. It is not only a hazard to health of people working in close proximity but also causes a nuisance to nearby communities. For these reasons, the Federal Aviation Administration has enforced increasingly strict noise regulations, expecting continuous expansion of the aviation industry in the foreseeable future [5].

In addition to the civil and industrial domains, military branches such as the U.S. Air Force and the U.S. Navy have funded several programs to suppress noise from their tactical aircraft [6, 7]. Flight-deck crews on aircraft carriers are subject to significant hearing health risks. High bypass ratio engines are impractical on supersonic aircraft. Furthermore, tactical aircraft must take-off at full military power to become airborne from the carrier deck. This creates an extreme acoustic environment, which renders

even the best hearing protection ineffective. Therefore, designing quieter jet engines is necessary.

Jet noise remains one of the most significant contributors to overall aviation noise. Even though exhaust jets are terrifyingly loud, the energy associated with acoustic radiation is small, compared to the aerodynamic energy contained in the turbulence of engine exhausts [8]. Because of this, predicting noise depends critically upon capturing the physics of the turbulence that produces it. Simulating turbulence, however, is challenging because it is a highly nonlinear, multi-scale, chaotic phenomenon.

Understanding the aeroacoustics of high-speed engine exhausts is important because it guides us to effective noise control/reduction strategies. The knowledge of jet aeroacoustics, however, is also valuable because it can provide new and profound understanding of the fluid turbulence that generates the noise. Turbulence is sometimes mistaken for a random process that can only be described using statistical methods. The study of jet noise supports an alternative view; specifically, the acoustic field surrounding a turbulent jet is exceedingly sensitive to both spatial and temporal coherence that is otherwise hidden in the turbulence. These coherent parts of turbulence are precisely those for which dynamical mechanisms can be identified and potentially controlled. In essence, jet noise is order that arises out of chaos. For example, figure 1.1 shows instantaneous pressure (gray) and temperature (color) fields of a Mach 1.5 turbulent jet. While the near-field aerodynamics appear complex and chaotic, involved with a wide range of length scales, acoustic radiation in the far-field is relatively directional and organized.

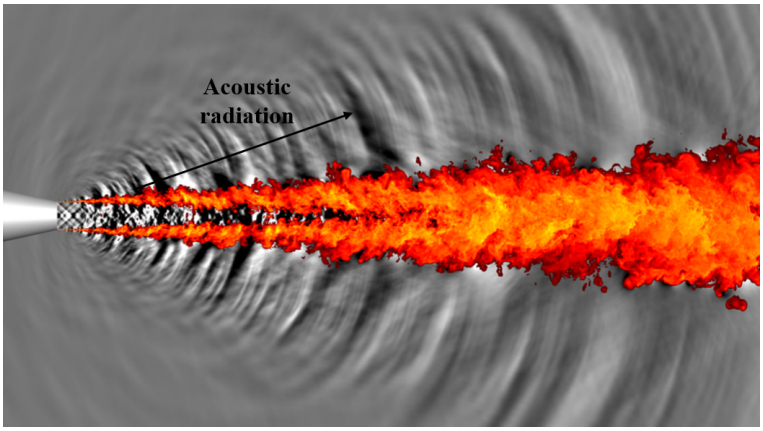

Figure 1.1: Instantaneous pressure (gray) and temperature (color) field for a Mach 1.5 isothermal, ideally-expanded, compressible turbulent jet predicted Brès et al. [1].

1.2 Review of literature on jet noise prediction and modeling

1.2.1 Acoustic analogy

Jet noise modeling was pioneered by Lighthill's acoustic analogy [9], which rearranges the full Navier-Stokes equations exactly into an inhomogeneous wave equation so that a wave propagation operator appears on the left hand side and an external fluctuating stress on the other side as follows:

$$\frac{\partial^2 \rho}{\partial t^2} - c_\infty^2 \nabla^2 \rho = \frac{\partial^2 T_{ij}}{\partial x_i x_j}, \tag{1.1}$$

for the density ρ. The Lighthill stress tensor T_{ij} is

$$T_{ij} = \rho u_i u_j + \left[(p - p_\infty) - c_\infty^2 (\rho - \rho_\infty) \right] \delta_{ij} - \tau_{ij}, \tag{1.2}$$

where u_i is the velocity in the x_i direction, p the static pressure, and c_∞ the ambient speed of sound. Similarly, the superscript ∞ denotes the ambient properties. Furthermore, δ_{ij} represents the Kronecker delta, and any repeated index in a single term indicates Einstein summation. Lastly, τ_{ij} is the viscous stress tensor. The acoustic analogy exactly separates aerodynamic sources of sound from its propagation away from the jet. Input-output analysis continues such legacy as will be discussed later.

The source terms on the right hand side are expressed in terms of local derivatives. This suggests that the sources of sound are compact. Non-compact effects, however, can be recovered by two-point two-time correlations between source terms in convolution with an adjoint Green's function of the wave propagation operator [10, 11]. Rearrangements of the Navier-Stokes equations, however, are not unique, as pointed out by Phillips [12]; Lighthill's theory has been thus improved and generalized by many others such as Curle [13], Phillips [12], Ffowcs Williams [14], Lilley [15], and Goldstein [16], by more strictly isolating nonlinear interactions within the right hand side from an convective or moving-medium wave operator.

1.2.2 Large-scale numerical simulations

The growth of large-scale supercomputers allows direct simulation of the near-field hydrodynamics of turbulent jets and the noise they produce in the far-field. Direct numerical simulation (DNS) is now well-established at low Reynolds numbers [17, 18], enabling reliable predictions of turbulent jets and associated sound radiation. Reynolds numbers associated with real engine exhausts are so large that simulations require a huge amount of computational resources to accurately resolve them. This is because there is a wide range of scales in high Reynolds number flows. Therefore, DNS is not a feasible option as a prediction tool for industrial design at current status of computational resources.

On the other hand, high-fidelity large-eddy simulation (LES) provides accurate predictions of noise radiation at significantly reduced cost for both subsonic jets [19, 20, 21] and supersonic jets [1, 22, 23] at moderate to high Reynolds numbers. In an LES only large-scale turbulent motions are directly computed, while the effect of small-scale motions on the flow is modeled. Still, it captures the far-field acoustics of turbulent jets well, suggesting that noise radiation is connected to large-scale flow features in jet turbulence. LES is also capable of predicting flow fields in complex configurations such as chevroned [24, 25] or military style faceted [26] engines. Changing the geometry of the engine nozzle can alter both the amplitude and the directivity of jet noise. The current applications of LES for predictions of turbulent jet noise are reviewed comprehensively by Bodony and Lele [27].

Noise prediction via high-fidelity simulations, however, is still too expensive and limited to the regions, close to the jet. Typically, far-field acoustics are measured at the distance of 100 diameters away from the nozzle exit. LES must be coupled with a projection method such as the Kirchhoff method [18, 28, 29, 30] or the Ffowcs Williams-Hawkings (FW-H) method [1, 31, 32, 33, 34, 35] as will be discussed in section 2.4.5. In addition, simulations offer neither jet noise models nor noise control strategies grounded on the physical mechanisms of noise generation. To investigate the noise generation mechanisms of turbulent jets and to ultimately design quieter jet engines in practical sense, developing new reduced-order models is necessary.

1.2.3 Wavepackets

Mollo-Christensen first reported the existence of highly-organized vortical structures within a seemingly chaotic turbulent flow and their link to jet noise radiation in the early 1960s [36, 37]. These wave-like large-scale structures, now known as wavepackets, have been also confirmed by other researchers [2, 3, 38, 39, 40, 41].

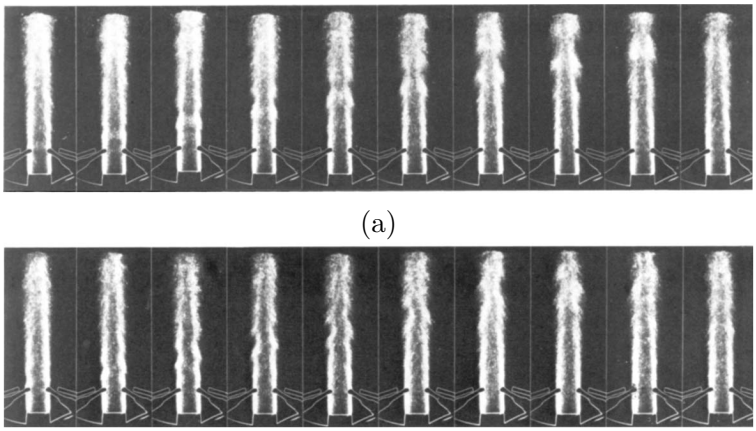

(a)

(b)

Figure 1.2: Visualizations of large-scale coherent structures in Mach 0.83 turbulent jets by Moore [2]: (a) the axisymmetric mode and (b) the first helical azimuthal mode.

Crow and Champagne [3] observed the linear growth of the fluctuation amplitudes up to near or slightly exceeding the end of the jet potential core. Evidence of linear behavior of large-scale structures encouraged attempts to represent them as linear instability waves, which were highly successful [42, 43, 44, 45, 46, 47, 48]. For example, Moore [2] provided visualization of coherent structures for the axisymmetric (figure 1.2 (a)) and the first helical (figure 1.2 (b)) azimuthal modes within unforced and forced turbulent jets at low to high subsonic speeds in conjunction with their noise radiation. His measurements were also compared with the results of linear stability theory by Michalke [49], showing good agreement.

Crow and Champagne [3] also observed that coherent puffs form intermittently in a jet at an average Strouhal number of about 0.3 based on the jet exit diameter and velocity as shown in figure 1.3. The intermittent nature of large-scale structures are believed to enhance the acoustic efficiency of turbulent jets, and noise source models accounting for intermittency, or jitter, show encouraging predictions [4, 39, 50, 51, 52] particularly in subsonic jets, as will be discussed more in detail in chapter 5.

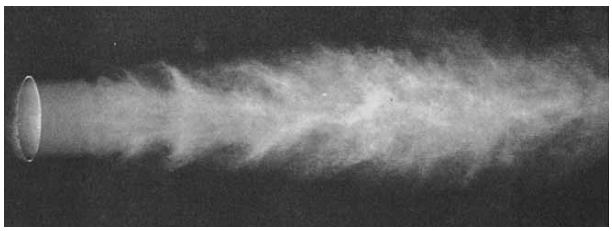

Figure 1.3: Flow visualizations of large-scale coherent structures in turbulent jets. Taken from Crow and Champagne [3].

The coherence of large-scale structures in unforced subsonic jets were quantified by Fuchs [38, 39], based on the measurements of pressure and velocity correlations. In these measurements strong coherence was seen over an axial length scale much larger than the local integral scale of turbulence. Furthermore, Michalke [42] and Michalke and Fuchs [53] expanded azimuthal Fourier modes of the source term in Lighthill's acoustic analogy and measured azimuthal correlations of pressure and axial velocities in subsonic jets. It was found that the axisymmetric pressure fluctuations contain almost 42% of the overall energy, and the first three to four azimuthal modes dominates the pressure field for low Strouhal numbers ranging from 0.2 to 1. Armstrong et al. [41] extended the measurements of the azimuthal coherence for higher Mach numbers and still observed dominance of low azimuthal modes.

Because wavepackets carry a significant portion of the total turbulent energy, they are believed to be closely connected to noise radiation. In fact, their spatio-temporal modulation is what enables a supersonic phase velocity relative to the ambient speed of sound, leading to far-field sound radiation [47, 50, 52, 53, 54, 55]. In contrast to Lighthill's acoustic analogy [9], which requires additional treatment to describe non-compact effects, jet noise modeling based on instability wavepackets is inherently associated with non-compact sources.

Instability wavepackets captured by the linearized Euler equations (LEE) [56, 57] or

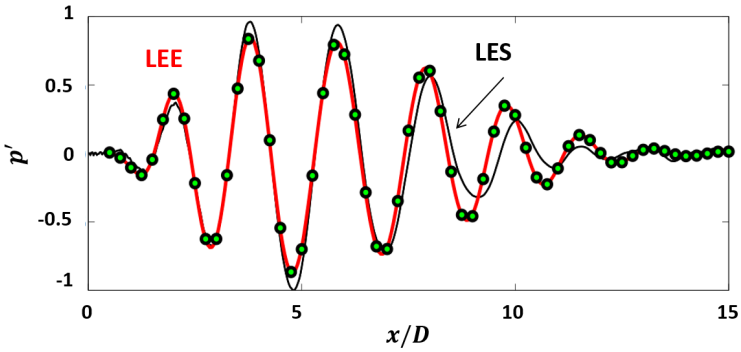

Figure 1.4: Wavepackets captured by LES and LEE at $St = 0.35$. The real part of the pressure eigenfunctions are shown. Taken from Jordan et al. [4].

parabolized stability equations (PSE) [52, 58, 59, 60, 61] match wavepackets measured in experiments [48, 62, 63] and simulations [4, 18, 51, 64]. For example, figure 1.4 shows almost perfect agreement between wavepackets captured by LEE and high-fidelity LES. PSE analysis captures far-field acoustics of supersonic jets successfully, but noise radiation from subsonic or heated supersonic jets is severely underpredicted, particularly in the sideline direction that is perpendicular to the jet axis. In subsonic jets, wavepackets are associated with energetically dominant motions, but only their supersonic portions radiate the far-field sound. The slight mismatch in figure 1.4 may in fact change the acoustic efficiency significantly because it alters the asymmetry of the wavepacket.

In this dissertation we apply input-output analysis [65, 66, 67, 68] to study the sensitivity of acoustically relevant dynamics in such jets. The resolvent analysis of energy amplification was introduced to wall-bounded turbulent shear flows [69, 70, 71, 65, 66, 72] and recently extended to high-speed turbulent jets [67, 68, 73]. Similarly, our method computes optimal and sub-optimal forcings, which correspond to noise-producing wavepackets in turbulent jets. We examine whether a set of few input-output modes can accurately predict the far-field sound of turbulent jets and thus may be used

as a basis for reduced-order models for turbulent jet noise.

1.3 Overview of contributions

The objective of the present research is to develop a new acoustic source model for turbulent jet noise that accurately predicts noise radiation from turbulent jets, based on a new understanding of their physical mechanisms. The major contributions of this dissertation are summarized as follows.

- As described in chapter 2, mathematical representations of input-output analysis and the numerical approach are established. Input-output analysis separates acoustic sources contained in the vicinity of jet turbulence from sound they produce in the far-field. It is in part inspired by the acoustic analogy in the context of the (spatial) separation of acoustic sources and noise propagation, but different in that our method provides dynamical description of sources radiating jet noise.

  it studies sensitivity of a linear operator corresponding to a given base flow to a volumetric external forcing.

- Chapter 3 describes input-output modes of subsonic and supersonic isothermal jets. The contributions of the optimal and sub-optimal modes to the far-field noise are quantified, and their roles in noise generation are discussed in detail in the same chapter. Also, it is shown that far-field acoustics of a $M_j = 1.5$ supersonic jet predicted by a high-fidelity LES is successfully reconstructed by superposing few input-output modes. The relevance of sub-optimal modes is further assessed through analysis of unsteady LES database.

- A new hybrid input-output/FW-H method is developed in chapter 4 and verified in appendix B for several cases where the analytic solutions are available. Using

this, the directivity of the acoustic far-field for a $M_j = 1.5$ supersonic jet is recovered similarly to that predicted by a high-fidelity LES. By repeating input-output analysis over a range of frequencies, far-field acoustic spectra is obtained, indicating broadening at high radiation angles for high frequencies.

- In chapter 5, input forcings are further weighted by the TKE to distill acoustically relevant aerodynamic sources. We find that resulting optimal input modes correspond to wavepackets with asymmetric pseudo-Gaussian functions. They remain similar in shape over a wide range of frequencies, scaled by $St^{-0.5}$. Furthermore, we show that sub-optimal modes are associated with jitter or decoherence of wavepackets.

- The robustness of input-output analysis is demonstrated regardless of the jet Mach number, applied heating, eddy viscosity, and azimuthal wavenumber modes through parametric studies in chapter 6.

Chapter 2

Mathematical models and numerical methods

2.1 Flow configuration

A schematic diagram of high-speed turbulent jets we consider in this study is shown in figure 2.1 in cylindrical coordinates (x, r, θ), respectively denoting the axial, radial, and azimuthal directions. In this figure a gray rectangle represents a thick straight cylindrical nozzle, extending from $x/R = -20$ to 0 where R is the jet diameter. An axisymmetric turbulent jet coming out of the nozzle discharges into quiescent ambient air at $x/R = 0$ and forms a shear layer, radiating sound into the far-field. As the jet spreads downstream, the jet exit velocity is maintained uniform for several diameters of the jet until it finally collapses. Such spatial duration, which is called the potential core length, may change based on the jet Mach number or jet-to-ambient temperature ratio as will be seen in later chapters. The computational domain ranges from $x/R = -20$ to 70 in the axial direction and $r/R = 0$ to 50 in the radial direction, respectively

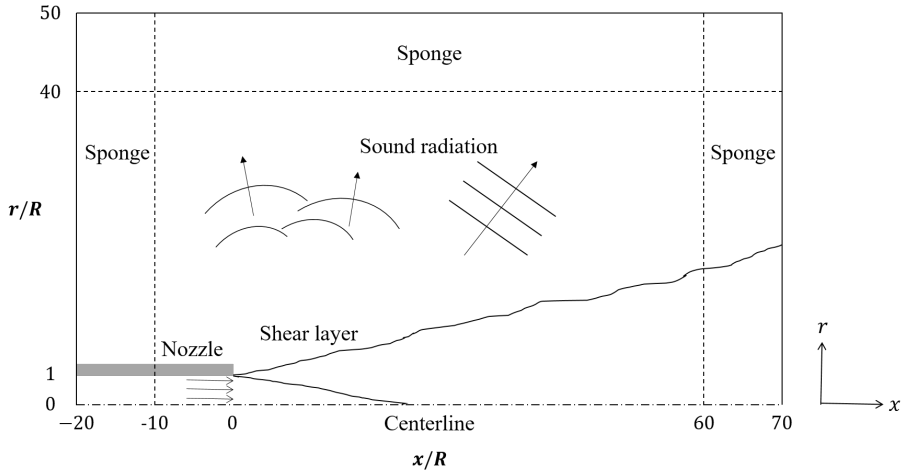

Figure 2.1: A schematic diagram of a turbulent jet in cylindrical coordinates. A gray rectangle represents a straight cylindrical nozzle, which discharges turbulent jets at $x/R = 0$ into a quiescent fluid. A dot-dashed line at $r/R = 0$ denotes the jet centerline, and dashed lines at $x/R = -10$, 60, and $r/R = 40$ are sponge layers employed to avoid unphysical reflection into the domain.

(unless otherwise stated). To approximate the Sommerfeld radiation condition, numerical sponge layers [74, 75, 76] are employed at the upstream, downstream, and lateral boundaries, absorbing outgoing waves to avoid unphysical reflection.

In this dissertation we study the dynamic of small disturbances about a mean field (a base flow), which are governed by the linearized Navier-Stokes (LNS) equations as will be described in the following sections. As base flows, we use Reynolds-averaged Navier-Stokes (RANS) solutions of ideally expanded, axisymmetric, compressible, turbulent jets. More details of each RANS base flow will be given in later chapters, depending on its operating conditions.

2.2 Governing equations

2.2.1 The Navier-Stokes equations

In this study the dynamics of the system state for a jet and associated sound radiation are governed by either the Euler equations or the Naiver-Stokes equations. While the Euler equations solve the motion of inviscid fluids, the Naiver-Stokes equations extensively describe viscous fluid flow. In other words, the Euler equation are derived easily by excluding viscous terms in the Navier-Stokes equations. In this section we therefore discuss the Naiver-Stokes equations only.

For an ideal gas, the conservations of mass, momentum, and energy are written as:

$$\frac{\partial \rho}{\partial t} + \boldsymbol{\nabla} \cdot \rho \boldsymbol{u} = 0 \,, \tag{2.1}$$

$$\frac{\partial \rho \boldsymbol{u}}{\partial t} + \boldsymbol{\nabla} \cdot \rho \boldsymbol{u}\boldsymbol{u} = -\boldsymbol{\nabla} p + \boldsymbol{\nabla} \cdot \boldsymbol{\tau} \,, \tag{2.2}$$

$$\frac{\partial \rho E}{\partial t} + \boldsymbol{\nabla} \cdot \rho E \boldsymbol{u} = -\boldsymbol{\nabla} \cdot p \boldsymbol{u} + \lambda \boldsymbol{\nabla}^2 T \,, \tag{2.3}$$

respectively, where ρ represents the fluid density and $\boldsymbol{u}$ is the fluid velocity. In equation (2.2) the fluid pressure is denoted by p. Furthermore, $\boldsymbol{\tau}$ represents the viscous stress tensor, which is expressed as:

$$\boldsymbol{\tau} = 2\mu \left[\boldsymbol{\nabla} \boldsymbol{u} + (\boldsymbol{\nabla} \boldsymbol{u})^T \right] - \frac{1}{3} (\boldsymbol{\nabla} \cdot \boldsymbol{u}) \boldsymbol{I}, \tag{2.4}$$

where μ denotes the dynamic viscosity that remains constant throughout the domain, and $\boldsymbol{I}$ is the identity matrix. Equation (2.3) describes the conservation of the total energy per unit mass of a moving fluid E, which is given by the sum of the internal energy per unit mass e and the kinetic energy per unit mass $k = \frac{1}{2} |\boldsymbol{u}|^2$ such that $E = e + k$. In this equation λ denotes the thermal conductivity, which is assumed to be

constant throughout the domain, and T represents the fluid temperature. In addition, the equation of the state is written as $p = \rho \mathcal{R} T$, where $\mathcal{R}$ is the gas constant.

We are now ready to rewrite the conservation equations for the system state in which we are more interested. First, taking a dot product of equation (2.2) with the velocity vector $\boldsymbol{u}$ yields the conservation of the kinetic energy k as:

$$\frac{\partial \rho k}{\partial t} + \boldsymbol{\nabla} \cdot \rho k \boldsymbol{u} \; = \; -\boldsymbol{u} \cdot \boldsymbol{\nabla} p - \Phi \; . \tag{2.5}$$

Here, the viscous dissipation tensor Φ is defined by $\boldsymbol{\tau} \; : \; \boldsymbol{\nabla} \boldsymbol{u}$, where the operator : represents the contraction of tensors. The conservation of the internal energy is then obtained by subtracting this from the total energy equation (equation (2.3)) as follows:

$$\frac{\partial \rho e}{\partial t} + \boldsymbol{\nabla} \cdot \rho e \boldsymbol{u} \; = \; -p \boldsymbol{\nabla} \cdot \boldsymbol{u} + \Phi \; . \tag{2.6}$$

Meanwhile, under the assumption of calorically perfect gas, we express the internal energy e as $e = c_v T$, where c_v is the specific heat of an ideal gas at constant volume. For the specific heat of an ideal gas at constant pressure c_p, the ratio of specific heats is defined as $\gamma = \frac{c_p}{c_v}$. The gas constant $\mathcal{R}$, which appears in the equation of state, is given by $\mathcal{R} = c_p - c_v$ so c_v may be further re-written as $c_v = \frac{\mathcal{R}}{\gamma - 1}$. Therefore, by manipulating the conservation of internal energy (equation (2.6)) and the equation of state, we form a conservation equation for the pressure as:

$$\frac{\partial p}{\partial t} + \boldsymbol{u} \cdot \boldsymbol{\nabla} p + \rho c^2 \boldsymbol{\nabla} \cdot \boldsymbol{u} \; = \; (\gamma - 1) \left[\lambda \boldsymbol{\nabla}^2 T + \Phi \right] \; , \tag{2.7}$$

where $c = \sqrt{\gamma p / \rho}$ is the speed of sound.

Next, a conservation equation for entropy of a system may be introduced by recalling the Gibbs equation, which describes change in internal energy in terms of changes in

entropy s and specific volume v of a system such that:

$$T\frac{Ds}{Dt} = \frac{De}{Dt} + p\frac{Dv}{Dt} . \tag{2.8}$$

Since $v = 1/\rho$, it may be further re-written as:

$$T\frac{Ds}{Dt} = \frac{De}{Dt} - \frac{p}{\rho}\frac{D\rho}{Dt} . \tag{2.9}$$

Moreover, by rearranging equation (2.1) as:

$$\frac{1}{\rho}\frac{D\rho}{Dt} = -\boldsymbol{\nabla}\cdot\boldsymbol{u} , \tag{2.10}$$

we may express the first term on the right hand side of equation (2.6) as:

$$-p\boldsymbol{\nabla}\cdot\boldsymbol{u} = \frac{p}{\rho}\frac{D\rho}{Dt} . \tag{2.11}$$

Finally, substituting this and equation (2.9) into the conservation of internal energy (equation (2.6)) gives the conservation of entropy such that:

$$\rho T\left(\frac{\partial s}{\partial t} + \boldsymbol{u}\cdot\boldsymbol{\nabla}s\right) = \lambda\boldsymbol{\nabla}^2 T + \Phi . \tag{2.12}$$

To summarize, for the system state $\mathbf{q} = \left[p;\, \mathbf{u}^T;\, s\right]^T$, the fully compressible Navier-Stokes equations are given in forms of:

$$\frac{\partial p}{\partial t} + \boldsymbol{u}\cdot\boldsymbol{\nabla}p + \rho c^2\boldsymbol{\nabla}\cdot\boldsymbol{u} = (\gamma - 1)\left[\lambda\boldsymbol{\nabla}^2 T + \Phi\right] , \tag{2.13}$$

$$\frac{\partial \rho \boldsymbol{u}}{\partial t} + \boldsymbol{\nabla} \cdot \rho \boldsymbol{u}\boldsymbol{u} = -\boldsymbol{\nabla} p + \boldsymbol{\nabla} \cdot \boldsymbol{\tau} \ , \tag{2.14}$$

$$\rho T \left(\frac{\partial s}{\partial t} + \boldsymbol{u} \cdot \boldsymbol{\nabla} s \right) = \lambda \boldsymbol{\nabla}^2 T + \Phi \ . \tag{2.15}$$

2.2.2 Scaling

In the previous section we obtained fully compressible Naiver-Stokes equations that govern motions of any compressible fluid flows. Nevertheless, since each of those flow systems has different physical scales, equations (2.13)-(2.15), which are still given in a dimensional form, may fail to directly tell the relative importance of each term. In this regards, this section aims to non-dimensionalize the governing equations using proper scaling factors. Non-dimensionalized equations then may introduce several dimensionless parameters, which allow us to better understand the relative significances of terms for systems under various conditions.

The flow configurations of a round jet naturally suggest fundamental scales based on the nozzle radius R, the jet velocity u_j, density ρ_j, and temperature T_j at the nozzle exit. In this way, we define dimensionless variables, which are denoted by superscript $*$, such as:

$$\nabla^* = R\nabla \ , \tag{2.16}$$

$$\boldsymbol{u}^* = \frac{\boldsymbol{u}}{u_j} \ , \tag{2.17}$$

$$t^* = \frac{t}{R/u_j} \ , \tag{2.18}$$

$$\rho^* = \frac{\rho}{\rho_j} \ , \tag{2.19}$$

$$p^* = \frac{p}{\rho_j u_j^2} \,, \tag{2.20}$$

$$T^* = \frac{T}{T_j} \,, \tag{2.21}$$

$$s^* = \frac{s}{u_j^2/T_j} \,, \tag{2.22}$$

$$c^* = \frac{c}{u_j} \,, \tag{2.23}$$

$$\tau^* = \frac{\tau}{\mu u_j/R} \,. \tag{2.24}$$

By substituting these variables into equations (2.13)-(2.15), the non-dimensional fully compressible Navier-Stokes equations for the system state $\boldsymbol{q} = \left[p; \boldsymbol{u}^T; s\right]^T$ are given in the following equations:

$$\frac{\partial p}{\partial t} + \boldsymbol{u} \cdot \boldsymbol{\nabla} p + \rho c^2 \boldsymbol{\nabla} \cdot \boldsymbol{u} = \frac{1}{Re} \left[\frac{1}{M_j^2 Pr} \boldsymbol{\nabla}^2 T + (\gamma - 1)\Phi \right] \,, \tag{2.25}$$

$$\frac{\partial \boldsymbol{u}}{\partial t} + \frac{1}{\rho} \boldsymbol{\nabla} p + \boldsymbol{u} \cdot \boldsymbol{\nabla} \boldsymbol{u} = \frac{1}{Re} \frac{1}{\rho} \boldsymbol{\nabla} \cdot \boldsymbol{\tau} \,, \tag{2.26}$$

$$\frac{\partial s}{\partial t} + \boldsymbol{u} \cdot \boldsymbol{\nabla} s = \frac{1}{Re} \frac{1}{\rho T} \left[\frac{1}{(\gamma - 1) M_j^2 Pr} \boldsymbol{\nabla}^2 T + \Phi \right] \,. \tag{2.27}$$

Note that, for simplicity, we have dropped the superscripts * in the above equations. Here, the entropy is defined by:

$$s = \ln(T)/((\gamma - 1)M_j^2) - \ln(p)/(\gamma M_j^2) \tag{2.28}$$

so that $s = 0$ is satisfied when $p = 1$ and $T = 1$ [77, 78]. Here, Re represents the Reynolds number defined as $Re = \rho_j u_j R/\mu$. The Prandtl number Pr is defined as $Pr = c_p \mu/\lambda$ and assumed to be constant throughout the computational domain. With

this non-dimensionalization process, the equation of state for an ideal gas becomes

$$\gamma M_j^2 p = \rho T. \tag{2.29}$$

The jet Mach number is defined as $M_j = u_j/c_j$ in terms of the speed of sound at the nozzle exit $c_j = \sqrt{\gamma p_j/\rho_j}$ where the ratio of specific heats γ has constant value 1.4.

2.2.3 Linearization

To examine the behavior of small perturbations about a base flow, the fully compressible Navier-Stokes equations are linearized. Using the standard Reynolds decomposition, we decompose the system state $\boldsymbol{q}$ into mean $\bar{()}$ and fluctuating parts $()'$, i.e., $\boldsymbol{q} = \bar{\boldsymbol{q}} + \boldsymbol{q'}$. After keeping the first-order terms only, we form the LNS equations as:

$$\begin{aligned}
&\frac{\partial p'}{\partial t} + \bar{\boldsymbol{u}} \cdot \boldsymbol{\nabla} p' + \boldsymbol{u'} \cdot \boldsymbol{\nabla} \bar{p} + \bar{\rho}\bar{c}^2 \boldsymbol{\nabla} \cdot \boldsymbol{u'} + \gamma(\boldsymbol{\nabla} \cdot \bar{\boldsymbol{u}}) p' = \\
&\quad \frac{1}{Re}\left[\frac{1}{{M_j}^2 Pr}\lambda \boldsymbol{\nabla}^2 T' + (\gamma - 1)\big(\bar{\boldsymbol{\tau}} : \boldsymbol{\nabla} \boldsymbol{u'} + \boldsymbol{\tau'} : \boldsymbol{\nabla} \bar{\boldsymbol{u}}\big)\right],
\end{aligned} \tag{2.30}$$

$$\frac{\partial \boldsymbol{u'}}{\partial t} + \frac{1}{\bar{\rho}}\boldsymbol{\nabla} p' + \frac{\rho'}{\bar{\rho}}\boldsymbol{\nabla}\bar{p} + \bar{\boldsymbol{u}} \cdot \boldsymbol{\nabla}\boldsymbol{u'} + \boldsymbol{u'} \cdot \boldsymbol{\nabla}\bar{\boldsymbol{u}} = \frac{1}{Re}\frac{1}{\bar{\rho}}\left(\boldsymbol{\nabla} \cdot \boldsymbol{\tau'} - \frac{\rho'}{\bar{\rho}}\boldsymbol{\nabla} \cdot \bar{\boldsymbol{\tau}}\right), \tag{2.31}$$

$$\begin{aligned}
&\frac{\partial s'}{\partial t} + \bar{\boldsymbol{u}} \cdot \boldsymbol{\nabla} s' + \boldsymbol{u'} \cdot \boldsymbol{\nabla} \bar{s} = \\
&\quad \frac{1}{Re}\frac{1}{\bar{\rho}\bar{T}}\left[\frac{1}{(\gamma - 1){M_j}^2 Pr}\left(\lambda \boldsymbol{\nabla}^2 T' - \frac{p'}{\bar{p}}\lambda \boldsymbol{\nabla}^2 \bar{T}\right) + \bar{\boldsymbol{\tau}} : \boldsymbol{\nabla}\boldsymbol{u'} + \boldsymbol{\tau'} : \boldsymbol{\nabla}\bar{\boldsymbol{u}} - \frac{p'}{\bar{p}}\bar{\boldsymbol{\tau}} : \boldsymbol{\nabla}\bar{\boldsymbol{u}}\right].
\end{aligned} \tag{2.32}$$

Similarly, we linearize the equation of state as:

$$\frac{\rho'}{\bar{\rho}} = \frac{p'}{\bar{p}} - \frac{T'}{\bar{T}}, \tag{2.33}$$

where

$$T' = (\gamma - 1)M_j^2 \left(\bar{T}s' + \frac{p'}{\bar{\rho}} \right). \tag{2.34}$$

In matrix form, the LNS equations for the perturbation system state q are re-written as:

$$\frac{\partial q}{\partial t} = Aq. \tag{2.35}$$

Here, the linear operator A corresponds to the governing equations, which is determined uniquely by a base flow. Again, for simplicity, we have dropped the primes and bold font.

2.2.4 Adjoint equations

The optimal forcing approach including input-output analysis finds flow fields, which optimally amplify small disturbances about a base flow under constraints such that solutions are governed by the LNS equations and given boundary and initial conditions. Lagrange multipliers are introduced to impose these constraints, yielding a system of equations called adjoint equations [71, 79, 80].

We begin by defining an inner product between any two state vectors q_1 and q_2 as:

$$\langle q_1, q_2 \rangle \equiv \int_V q_1^* q_2 dV, \tag{2.36}$$

where a superscript $*$ indicates the complex-conjugate transpose, and dV is a differential volume element. From this definition, Lagrange multipliers $q^\dagger$ satisfy the Lagrange identity such that:

$$\left\langle q^\dagger, Aq \right\rangle = \left\langle A^\dagger q^\dagger, q \right\rangle, \tag{2.37}$$

with respect to the linear operator A corresponding to the direct LNS equations and any state vector q. Then, manipulation of equations (2.30)-(2.32) using suitable integration

by parts leads to the adjoint equations, denoted by an operator $A^\dagger$ in the above relations.

2.3 Input-output analysis

The high-speed jets we consider in the present study are globally stable; they are, however, highly unstable to convective perturbations in the form of wavepackets [52]. We therefore treat these jets as amplifiers, which take external disturbances as inputs and give back the far-field acoustics as outputs. This behavior is much different from that of globally unstable flows, which support self-sustained oscillations, and thus it is best studied by investigating the sensitivity to an external forcing.

To understand how an input forcing maps onto output quantities of interests, we modify the original linear system in equation (2.35) by introducing an external forcing f as follows:

$$\dot{q} = Aq + Bf, \tag{2.38}$$

$$y = Cq, \tag{2.39}$$

where y represents output quantities, and matrices B and C are determined depending on inputs and outputs of interests, respectively. For example, we specify B to select forcings applied to the velocity equations near the jet turbulence while C is chosen to specify noise in the region far away from sources. The choice of specifying matrices B and C makes our analysis unique compared to other approaches, which consider the entire system state to evaluate the gain.

In this study we seek wave-like solutions by taking the wavepacket ansatz as:

$$q(x, r, \theta, t) = \hat{q}(x, r)e^{\mathrm{i}(m\theta - \omega t)}, \tag{2.40}$$

where m is an integer azimuthal wavenumber and ω is the temporal frequency.

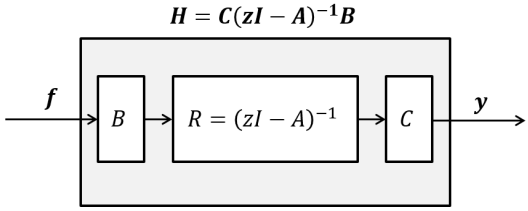

Figure 2.2: Schematic of the linear system for turbulent jet noise modeled using the wavepacket ansatz. External forcings f are mapped onto output y through the transfer function H, which includes the resolvent operator $R = (zI - A)^{-1}$.

Moreover, by assuming harmonically forced perturbations such that $f = \hat{f}e^{zt}$ and $y = \hat{y}e^{zt}$, substituting the wavepacket ansatz into equations (2.38) and (2.39) yields a transfer function H from inputs f to outputs y for a given temporal frequency ω as:

$$H = C(zI - A)^{-1}B, \tag{2.41}$$

where $z = -\mathrm{i}\omega$. Note that the transfer function H consists of the resolvent operator $R = (zI - A)^{-1}$. Figure 2.2 visualizes a schematic of such linear system with wave-like external forcings.

By taking the singular value decomposition at a given frequency, the transfer function H may be further decomposed into:

$$H = U\Sigma V^*, \tag{2.42}$$

where U and V are unitary matrices. Diagonal elements of a matrix Σ consist of singular values σ in descending order, which represent the gain in amplitude from input to output defined as:

$$\sigma = \frac{\|\boldsymbol{y}\|}{\|\boldsymbol{f}\|}, \tag{2.43}$$

where $\|\cdot\|$ means the L^2 norm such as $\|\cdot\|^2 = \langle \cdot, \cdot \rangle$ with an inner product defined as

equation (2.36).

Alternatively, the transfer function may be written as:

$$HV = U\Sigma. \tag{2.44}$$

The above system is thus interpreted such that each column of V, i.e., an input vector is amplified by the corresponding singular value and mapped to the corresponding column of U, i.e., an output vector through the transfer function H [71].

As written in equation (2.37) the Lagrange identity gives the following relations for the adjoint $A^\dagger$ of the linear operator as follows:

$$\left\langle A^\dagger q_1, q_2 \right\rangle = \langle q_1, Aq_2 \rangle \,, \tag{2.45}$$

where q_1 and q_2 are any two state vectors. After discretization, we may represent this in matrix form as:

$$(A^\dagger q_1)^* W q_2 = q_1^* W A q_2, \tag{2.46}$$

where W is a real diagonal matrix of quadrature weights. This implies that the adjoint of a discretized version of the operator A is:

$$A^\dagger = W^{-1} A^* W. \tag{2.47}$$

We use these definitions to find the singular values and the right-singular vectors of H through the eigenvalue decomposition of $H^\dagger H$ such that:

$$H^\dagger H = B^*(z^* I - A^\dagger)^{-1} C^\dagger C (zI - A)^{-1} B. \tag{2.48}$$

Here, the eigenvalues of $H^\dagger H$ are the squares of the corresponding singular values σ of

H.

One advantage of input-output analysis is that the matrices B and C may be selected depending on inputs and outputs of interest. For example, in the present study, we have chosen B to force the velocity equations (2.31) in the immediate vicinity of jet ($r/R < 2.90$) and C to select far-field pressure in the region where $r/R > 8.70$ or along an arc 200 radii far way from the jet exit. The spatial separation of input and output domains is motivated in part by the acoustic analogy approach [9, 16] where acoustic sources are separated from acoustic propagation through an exact rearrangement of the compressible Navier-Stokes equations. In this view, acoustic sources are associated with unsteady turbulent flow, and thus are restricted in space to the immediate vicinity of the jet. The effects, however, occur far away from the jet where acoustic propagation is important, but acoustic sources are inactive. Recently, statistical models of acoustic source terms, calibrated by high-fidelity simulation data and laboratory measurements, have been shown to successfully predict noise from high-speed jets after convolution with an appropriate adjoint Green's function [11, 81]. Our analysis is in concert with this idea, but instead of analyzing two-point two-time fourth order statistical correlations, we use input-output analysis of the linearized equations to identify dynamic structure in the acoustic sources.

2.4 Numerical methods

2.4.1 Computational grids

Throughout this dissertation, grid points are distributed with uniform spacing in the axial direction but are refined and clustered in the radial direction along the nozzle lipline to resolve the boundary layer and thin shear layer formed near the nozzle lip. To ensure the independence of our analysis on grids, we test four different grid resolutions

in appendix A.1. Based on this test, the number of grid points in the axial and radial directions are determined by $N_x = 576$ and $N_r = 288$, respectively, unless otherwise noted. In chapter 5 we extend the numerical domain to $x/R = 80$, or $x/D = 40$ based on the jet diameter, in the axial direction while keeping the radial extent of the domain unchanged such that $r/D = 25$. In this case we increase the number of axial grids to $N_x = 801$ so that a uniform spacing $\Delta x = 0.125$ is achieved.

2.4.2 Discretization

The LNS equations are discretized by fourth-order five-point stencil centered finite differences, yielding a large sparse matrix. Near the region where the five-point stencil are not applicable, such as along the nozzle wall, jet centerline, and boundaries of the numerical domain, we choose one-sided finite difference methods using the three-point stencil. Since grids are stretched in the radial direction to cluster grid points about the nozzle lipline while they are uniform in the axial direction, finite difference approximations of radial derivatives should consider appropriate weights such that:

$$\frac{\partial f}{\partial r} = \frac{\partial f}{\partial \eta}\frac{\partial \eta}{\partial r}, \tag{2.49}$$

$$\frac{\partial^2 f}{\partial r^2} = \frac{\partial^2 f}{\partial \eta^2}\frac{\partial^2 \eta}{\partial r^2}, \tag{2.50}$$

for a state variable f, where η is a weighting function.

Since the centered finite difference scheme is non-dissipative, a scale-selective fourth-order numerical filter is added to damp unphysical waves at the highest wavenumbers. In appendix A we show that this filter does not affect modes we are interested in once a mesh is well-resolved.

2.4.3 ARPACK

The largest eigenvalues of $H^\dagger H$ are computed using the implicitly restarted Arnoldi method (IRAM) as implemented by the software package ARPACK [82]. We compute the matrix inversion associated with the resolvent operator using the sparse direct solver PARDISO, which is part of the Intel Math Kernel Library. In cases of higher azimuthal wavenumber modes where more intensive computational resources are required, we use the massively parallel SuperLU package [83] to find the LU-decomposition of the sparse matrix. Because the iterative Arnoldi method requires many evaluations of the resolvent at a fixed frequency, the resolvent matrix may be factorized only once. After this, the factors are applied to efficiently perform repeated evaluations of the resolvent. Compared to global mode analysis where non-normality of the system matrix A may impede convergence of the Arnoldi method, the eigenvectors of $H^\dagger H$ form an orthogonal set of input modes, so the Arnoldi method converges rapidly.

2.4.4 Discrete adjoint vs. continuous adjoint approaches

The adjoint of the transfer function $H^\dagger$, which maps outputs back onto inputs, may be evaluated in two different ways. For example, the discrete adjoint approach first discretizes the continuous equations and then derives the adjoint through a matrix transpose. Alternatively, in the continuous adjoint approach, equations adjoint to the linearized governing equations are first derived through integration by parts and then discretized later to find a matrix that approximates A^*. The continuous adjoint approach, however, allows specification of one-sided differences consistent with continuous derivatives near to wall boundaries, such as the cylindrical nozzle. The discrete approach, on the other hand, does not guarantee consistency near boundaries, resulting in large numerical errors as shown in figure 2.3. For this reason, we adopt the continuous

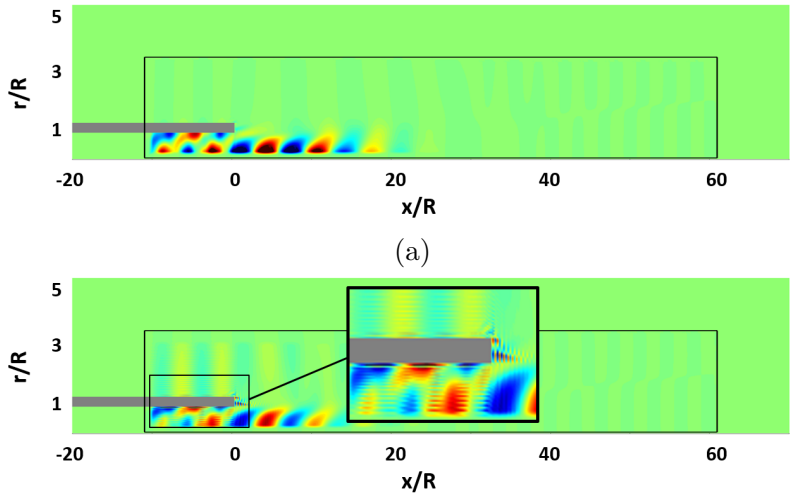

Figure 2.3: (a) The continuous adjoint approach allows one-sided differences consistent with continuous derivatives near to wall boundaries, removing large numerical errors that may appear in (b) the discrete adjoint approach.

adjoint approach in the present investigation [84, 85, 86, 87, 88].

2.4.5 Kirchhoff vs. Ffowcs Williams-Hawkings (FW-H) methods

To directly compute the near-field jet turbulence and its radiated sound in the far-field (typically, 100 diameters away from the nozzle exit) together would be too expensive. Instead, the development of projection methods such as the Kirchhoff method [18, 28, 29, 30] and the FW-H method [1, 22, 32, 33, 35, 89] greatly reduces the computational cost of predicting far-field acoustics by allowing much smaller computational domains. In these methods we may collect the near-field flow data only, which are extrapolated to much farther region through surface and/or volume integrals along a projection surface. It is therefore important to locate a projection surface properly so that it can enclose acoustic sources as much as possible while not sacrificing the computational efficiency.

The Kirchhoff formula is equivalent to the wave equation. A projection surface

thus should be placed in the linear flow region for accurate predictions in this case. Compared to the FW-H method, the Kirchhoff method is easy to implement since it involves surface source terms only. By taking a cylindrical projection surface at $r = R_0$ whose axis lies along the jet centerline, far-field pressure in the frequency domain is given by:

$$p_n(k, r, \omega) = \begin{cases} p_n(k, R_0, \omega) {H_n}^{(1)} \left(r\sqrt{\omega^2 - k^2} \right) / {H_n}^{(1)} \left(R_0\sqrt{\omega^2 - k^2} \right), & \text{if } \omega > 0, \\ p_n(k, R_0, \omega) {H_n}^{(2)} \left(r\sqrt{\omega^2 - k^2} \right) / {H_n}^{(2)} \left(R_0\sqrt{\omega^2 - k^2} \right), & \text{if } \omega < 0, \end{cases} \tag{2.51}$$

where ${H_n}^{(1)}$ and ${H_n}^{(2)}$ are Henkel functions of the first and second kind, respectively [18]. The above equation implies that only modes involving supersonic phase speed, i.e., $\omega > k$ radiate sound. Thanks to its simplicity, we have used this formula in the early stages of the present study, which are given in chapters 3 and 6.

Even though the Kirchhoff method has some advantages, particularly in the context of ease in implementation, the FW-H method is more preferred in many cases. Because it is based on the Navier-Stokes equations, a projection surface may be positioned much closer to jet turbulence than a Kirchhoff projection surface should be. It also separates source terms into two surface source terms and one volume source term, which respectively correspond to monopole, dipole, and quadrupole forms [14, 31, 32, 33]. The volume integrations (quadrupoles) require severe computational work, but when quadrupoles are omitted, the FW-H formulation may be calculated as efficiently as the Kirchhoff method. Errors due to neglecting quadrupole terms may not be very substantial, provided that an FW-H surface is chosen carefully. Furthermore, using a closed outflow surface disk or even averaging over outflow disks (end-cap averaging) [1, 22, 35, 89] may alleviate the errors. The FW-H method and its linearized version are discussed in chapters 4 and 5. Detailed validations are further provided in appendix B.

Chapter 3

Input-output modes of high-speed turbulent jets

In this chapter we apply input-output analysis to high-speed supersonic and subsonic turbulent jets. We present resulting pairs of input-output modes and acoustic gains, and discuss their characteristics. The physical relevance of sub-optimal input-output modes are assessed by projecting a high-fidelity LES database onto them. This chapter is reproduced from [68], with the permission of AIP Publishing.

3.1 Base flows

Throughout this study, we consider the dynamic of small disturbances about RANS base flows of ideally expanded, axisymmetric, compressible, turbulent jets. We use RANS solutions as base flows, which are computed using a modified $k - \varepsilon$ turbulence model with coefficients suggested by Thies and Tam [90] for high-speed jets. While the base flows are solutions to the RANS equations, we treat small perturbations about these base flows as governed by the LEE. Even though the RANS solutions are not

equilibrium solutions to the Euler equations, the wave-like perturbations that we obtain below and that are connected to acoustic radiation, are correlated over length scales much larger than the integral length scales of the turbulence. These modes then do not contribute significantly to the modification of the turbulent mean profile which is instead supported by Reynolds stresses involving much shorter length scales. Because of this scale separation, previous studies have found that linear analysis about turbulent mean base flows is able to predict experimental observations of coherent structures in jets rather closely [45, 52].

Figure 3.1 shows contours of axial velocity from a RANS calculation of $M_j = 1.5$ supersonic jet. A white line from $x/R = -20$ to $x/R = 0$ in this figure corresponds to a straight cylindrical nozzle with radius $R = 1$ and wall thickness $t = 0.3R$. A RANS solution for a $M_j = 1.5$ jet corresponds to the operating conditions of an LES performed previously [1], including a weak co-flow surrounding the main jet. The magnitude of the co-flow in this case is set to 6.7% of nozzle exit velocity, and this co-flow is enforced at the upstream boundary outside of the nozzle. In addition to the RANS solution for the $M_j = 1.5$ jet, we also produce RANS solutions for a $M_j = 0.9$ subsonic jet. In each case, unless otherwise specified, we consider ideally expanded and isothermal jets such that $T_j/T_\infty = 1$, $p_j/p_\infty = 1$, and the Reynolds number $Re = \rho_j u_j R/\mu = 10^6$ where μ is the dynamic viscosity, which we assume to be constant throughout the domain. Here, the subscripts j and ∞ represent properties at the nozzle exit and in the ambient fluid, respectively. While figure 3.1 shows only part of it, the actual computational domain extended from $x/R = -20$ to $x/R = 70$ in the axial direction and from $r/R = 0$ to $r/R = 50$ in the radial direction.

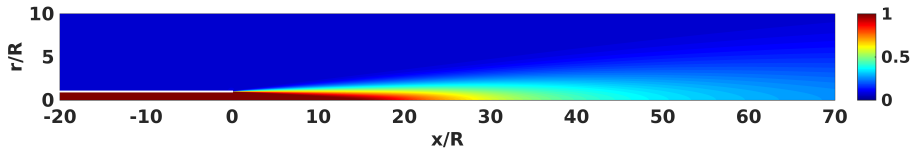

Figure 3.1: Contours of axial velocity from a RANS solution of a round $M_j = 1.5$ supersonic jet. The velocity contours are normalized by the velocity at the nozzle exit at $x/R = 0$. The cylindrical nozzle is represented by the white line extending from $x/R = -20$ to $x/R = 0$ at $r/R = 1$.

3.2 Optimal and sub-optimal modes

3.2.1 $M_j = 1.5$ supersonic jet

At every temporal frequency ω, we obtain orthonormal sets of input and output modes, ordered by the corresponding gains. In what follows, we denote this ordering by the mode number n. Figure 3.2 shows the first 50 gains for the $M_j = 1.5$ supersonic jet at frequency $St = f(2R)/u_j = 0.33$ where $f = \omega/(2\pi)$. Mode number $n = 1$ is associated with the maximum gain, which was found to be $\sigma_1 = 1.35 \times 10^2$. Figure 3.3(a) shows the corresponding optimal forcing mode and figure 3.4(a) shows the resulting output mode. As indicated by the rectangle in figure 3.3, we have restricted the input forcing to be inside the region $-10 < x/R < 60$ and $0.29 < r/R < 2.90$. The output, however, is restricted to be pressure perturbations inside the region $-10 < x/R < 60$ and $8.70 < r/R < 39.2$, as indicated by the rectangle in figure 3.4(a). This choice is motivated by the goal of understanding how forcing the velocity equations inside the jet produces sound in the far-field. We use these input and output domains throughout this chapter and in chapter 6. To avoid numerical errors due to sharp transitions at the boundaries of the input and output domains, input modes are gradually reduced to zero over several grid points.

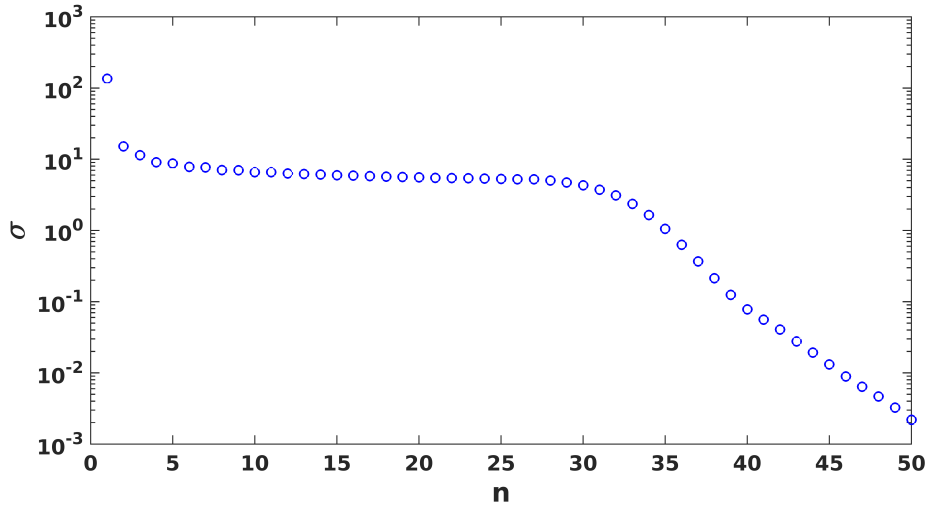

Figure 3.2: Singular values vs. mode number for the $M_j = 1.5$ supersonic jet with forcing frequency $St = 0.33$.

The input modes are visualized by contours of the real part of the input axial velocity forcing restricted in the near-field, and the output modes are visualized by contours of the real part of the output pressure in the far-field. For this supersonic jet, the output pressure agrees well with the acoustic far-field of a wavepacket computed using PSE or global mode analysis. It consists of a single acoustic beam radiating at an angle of 30° in the direction of peak jet noise. We also observe that the input is mostly concentrated near the nozzle lip. For supersonic jets, instability waves are linked to the acoustic far-field through the Mach wave mechanism [91]. According to this mechanism, a small disturbance upstream can trigger a supersonic instability wave downstream which then generates noise. This instability process is captured well by the PSE [60].

In addition to the optimal mode, input-output analysis of jet noise yields several sub-optimal modes. These sub-optimal modes follow a pattern as shown in figure 3.4. Whereas the optimal output mode ($n = 1$) consists of a single acoustic beam, the first sub-optimal output mode ($n = 2$) is comprised of two acoustic beams radiating away

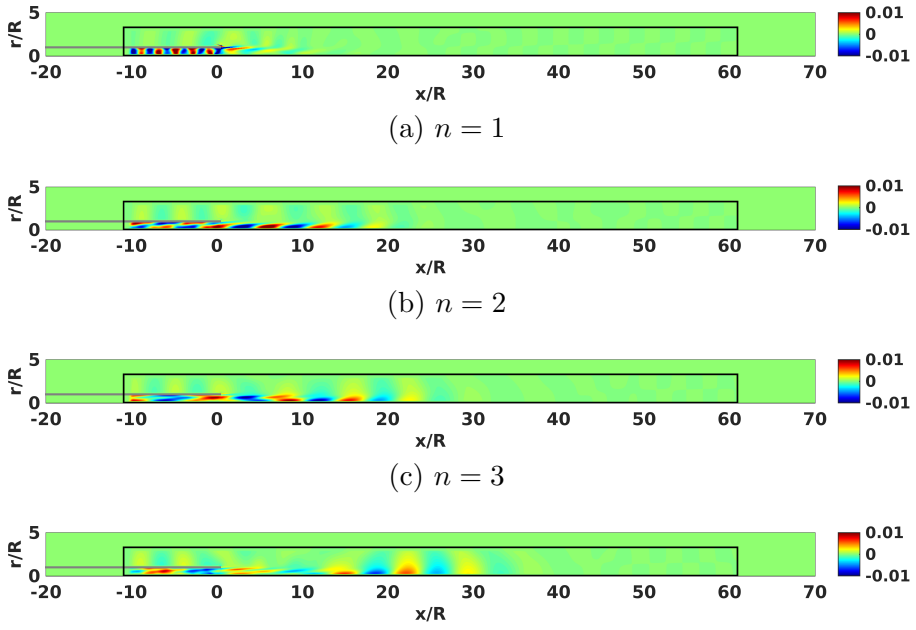

(a) $n = 1$

(b) $n = 2$

(c) $n = 3$

(d) $n = 4$

Figure 3.3: The first four input modes of the $M_j = 1.5$ supersonic jet for forcing frequency $St = 0.33$. Contours of the real part of the normalized axial velocity forcing are shown.

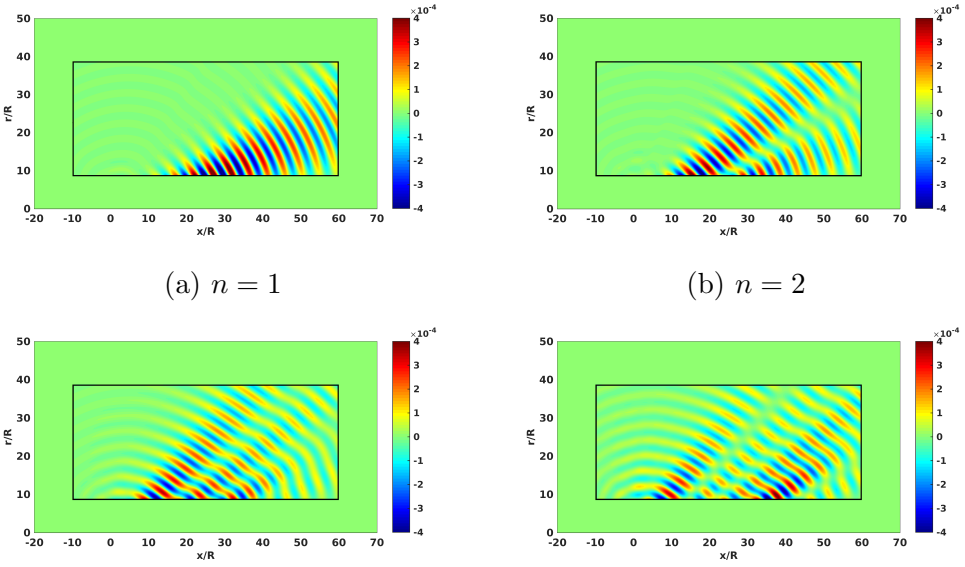

(a) $n = 1$ (b) $n = 2$

(c) $n = 3$ (d) $n = 4$

Figure 3.4: The first four output modes of the $M_j = 1.5$ supersonic jet for forcing frequency $St = 0.33$. Contours of the real part of normalized output pressure fluctuations are shown.

from the jet. Note that in the first sub-optimal mode, one beam radiates at a slightly larger angle with respect to the centerline than does the single beam in the optimal mode. The other acoustic beam in the first sub-optimal mode propagates at a slightly smaller angle with respect to the centerline than the single beam in the optimal mode. Similarly, the third output mode ($n = 3$) contains three acoustic beams: one at a yet larger radiation angle, one at a smaller radiation angle, and one at an intermediate angle. These three acoustic beams follow the edges of the two acoustic beams associated with the first sub-optimal mode. The higher modes continue to follow this tendency of incorporating additional beams that radiate at larger angles with respect to the downstream jet axis.

While the optimal input mode is concentrated inside the nozzle and at the jet exit, the sub-optimal input mode shapes shown in figure 3.3 extend increasingly far downstream as the mode number increases. For $n = 4$, the peak input forcing is located at $x/R \approx 20$ downstream inside the jet.

3.2.2 $M_j = 0.9$ subsonic jet

We repeat the input-output analysis for a $M_j = 0.9$ isothermal jet with forcing frequency $St = 0.56$. As discussed below, this jet Strouhal number yields the same acoustic Strouhal number $St_a = StM_a = 0.50$, where $M_a = u_j/c_\infty$ is the acoustic Mach number defined in terms of the ambient speed of sound c_∞. For isothermal jets, $c_\infty = c_j$, so $M_a = M_j$. Figures 3.5 and 3.6 show the first two input and output modes, respectively. In contrast to the supersonic jet, the optimal input for the subsonic jet extends further downstream from the nozzle exit. The output modes, however, follow a similar pattern to the supersonic case. The optimal mode has a single acoustic beam radiating away from the jet, while the second mode (first sub-optimal) has an additional beam. The radiation angles for the subsonic jet output modes are greater than for the supersonic

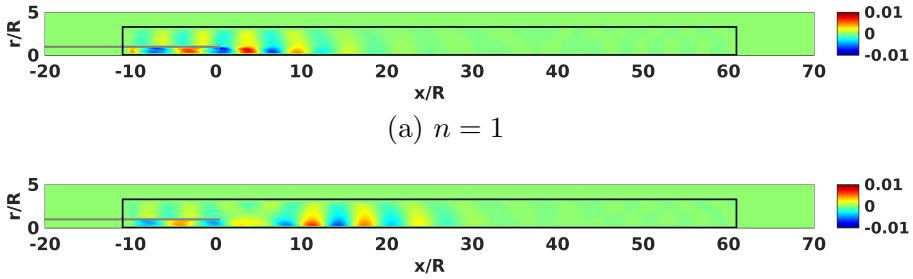

(a) $n = 1$

(b) $n = 2$

Figure 3.5: The first two input modes of the $M_j = 0.9$ subsonic jet for forcing frequency $St = 0.56$. Contours show the real part of axial velocity forcing as in figure 3.3.

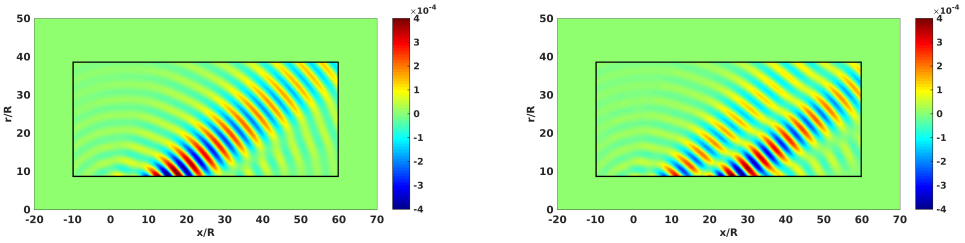

(a) $n = 1$ (b) $n = 2$

Figure 3.6: The first two output modes of the $M_j = 0.9$ subsonic jet for forcing frequency $St = 0.56$. Contours show the real part of pressure fluctuations as in figure 3.4.

case.

Figure 3.7 shows singular values for the $M_j = 0.9$ subsonic jet. For the supersonic jet, the largest singular value, representing the maximum gain by the optimal mode, was two orders of magnitude greater than the gain obtained for the first sub-optimal mode. In the subsonic jet, however, the second singular value is comparable to the most significant singular value. This suggests that while the optimal mode dominates the acoustics in the supersonic jet, the contribution of sub-optimal modes should not be neglected in predicting the subsonic jet noise.

To quantify the importance of the sub-optimal modes, note that the sum of the

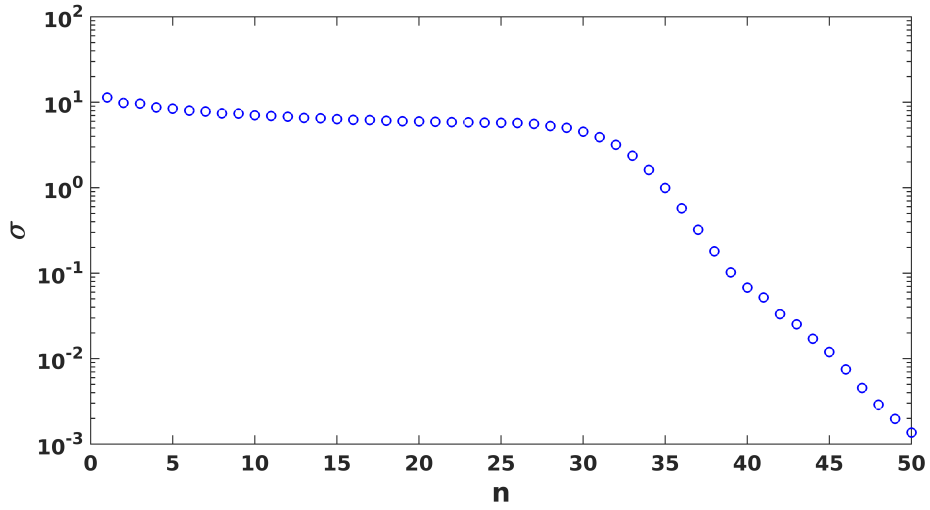

Figure 3.7: Singular values vs. mode number for the $M_j = 0.9$ subsonic jet with forcing frequency $St = 0.56$.

squares of the singular values is proportional to the total acoustic intensity of output modes in response to white noise forcing. The acoustic intensity of the optimal output mode is proportional to the square of the first singular value, alone. Therefore, the decibel increase in sound pressure level (ΔSPL) obtained by including the sub-optimal modes vs. retaining only the optimal mode is:

$$\Delta SPL = 10 \log_{10} \left(\frac{\sum \sigma_i^2}{\sigma_1^2} \right). \tag{3.1}$$

For the supersonic jet at $St_a = 0.50$, we find a marginal increase of $0.33dB$, owing to the dominance of the optimal mode. For the subsonic case, however, including the sub-optimal modes results in a $10.6dB$ increase in SPL.

3.3 Role of sub-optimal modes

3.3.1 Large-eddy simulations (LES) of a $M_j = 1.5$ supersonic jet

Since input-output analysis is linear, the amplitudes of the input and output modes are arbitrary, and are in fact normalized with respect to the inner product (equation (2.36)). The increase in noise ΔSPL computed using equation (3.1) assumes that all modes are forced equally with unit energy. In other words, this assumes the forcing supplied by the jet turbulence to the input modes is equivalent to white noise. It is well-known, however, that the statistics of turbulent fluctuations are not equivalent to white noise. In this section, we therefore investigate whether the sub-optimal modes remain relevant when realistic forcing from an LES is projected onto their input singular directions.

For this purpose, an LES database for an isothermal jet with jet Mach number $M_j = 1.5$ and 6.7% axial co-flow was obtained using an unstructured finite-volume compressible flow solver. For further details about this LES, we refer the reader to Brès et al. [1]. The LES base flow was computed as the time average of $10,000$ snapshots taken from the LES spaced at time intervals of $0.02D/c_\infty$. Since we consider an axisymmetric jet in the present study, the base flow is also averaged in the azimuthal direction. Figure 3.8 shows contours of axial velocity for the base flow taken from the LES.

Compared to the RANS calculations, the LES was conducted for a smaller numerical domain, ranging from $x/R = 0$ to 40 and $r/R = 0$ to 10, in the axial and lateral directions, respectively. The LES base flow was extrapolated to the RANS domain so that input-output analysis using both base flows could be appropriately compared. Considering the spatial restriction of the original LES domain, we also restricted the input and output domains to $x/R = 40$ in the streamwise direction, but other parameters remained unchanged. Due to slightly mismatched conditions between two base flows, an exact comparison is not possible. Nevertheless, the singular values for both cases

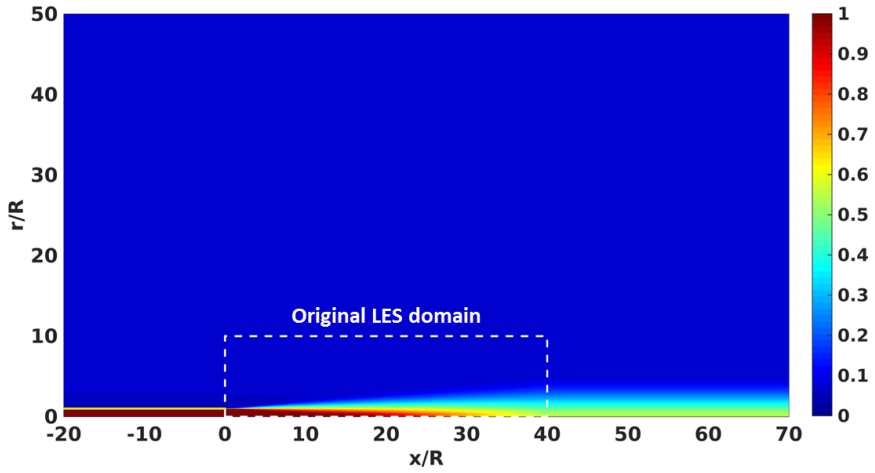

Figure 3.8: Contours of time-averaged axial velocity from a LES of a $M_j = 1.5$ supersonic jet. The white dashed lines indicate the extent of the computational domain of the LES. As discussed in the text, the resulting base flow was then extended to the larger domain used for calculations based on RANS solutions.

agree remarkably well, as shown in figure 3.9. The only discrepancy is observed for the first singular value, which is 1.77 times larger for the LES base flow than for the RANS base flow. We note, however, that the singular directions (not shown) for these two cases are nearly identical.

The discrepancy in optimal gain is in part related to the convergence levels of the RANS and LES base flows. Since RANS calculations are not computationally expensive, they are converged to machine precision. On the other hand, even though the LES base flow is formed from an average of 10,000 snapshots, small residual errors remain that are larger than those associated with RANS. Therefore, the LES base flow is less smooth than the RANS base flow, with enhanced spatial gradients leading to enhanced gain. Confirming this, we also find that averaging fewer snapshots leads to a slightly greater optimal gain. The input and output modes, however, remain essentially unchanged. The robustness of the input and output modes highlights the fact that input-output

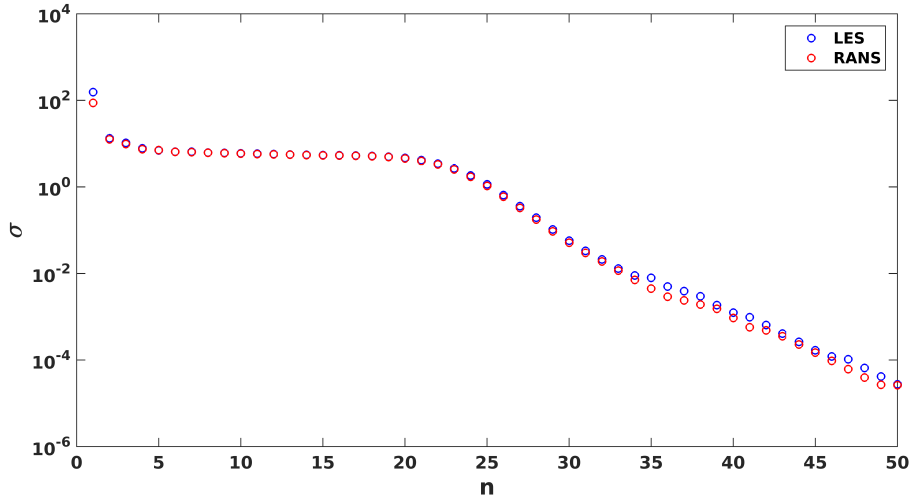

Figure 3.9: Spectra of singular values using the RANS and LES base flows for $M_j = 1.5$ at $St = 0.33$.

analysis does not rely upon an assumption of a smoothly-varying base flow. In other words, a useful feature of input-output analysis is that it can be applied directly to "noisy" base flows and still yield reasonable results—results that become increasingly accurate as the convergence of the base flow improves.

Another source of the discrepancy in optimal gain between RANS and LES may be the fact that the shear layers in the LES emerge from the nozzle in an initially laminar state. As documented by Brès et al. [1], this leads to an overshoot in fluctuation levels close to the nozzle lip compared to experimental measurements. Large gradients associated with thin initial shear layers increase the growth of instability waves, and thus increase the optimal gain in the present analysis. The RANS calculations, on the other hand, use a modified $k-\varepsilon$ model that is known to produce base flows that validate well against experiment. Nevertheless, so as not to overstate our results, we choose to use the LES base flow specifically because it represents the worst case. The difference in gains between optimal and sub-optimal modes is greater for the LES base flow, so

the importance of sub-optimal modes appears diminished. The results obtained below, however, should be seen as lower bounds.

3.3.2 Amplitude of input modes

The input forcing f we consider in this thesis appears as a source term added to the right hand side of the linearized velocity equations (2.31). This source term can also be derived through an exact rearrangement of equation (2.26). Substituting $\boldsymbol{u} = \bar{\boldsymbol{u}} + \boldsymbol{u'}$ and $\rho = \bar{\rho} + \rho'$ into equation (2.26), subtracting out base flow terms, and collecting terms associated with the linearized operator A on the left hand side yields:

$$\frac{\partial \boldsymbol{u'}}{\partial t} + \frac{1}{\bar{\rho}}\nabla p' + \bar{\boldsymbol{u}} \cdot \nabla \boldsymbol{u'} + \boldsymbol{u'} \cdot \nabla \bar{\boldsymbol{u}} = \left[\frac{1}{\bar{\rho}} - \frac{1}{\bar{\rho} + \rho'}\right] \nabla p' - \boldsymbol{u'} \cdot \nabla \boldsymbol{u'}. \tag{3.2}$$

Note that this is exactly the same procedure used to derive an acoustic analogy. After taking Fourier transforms in time and in the azimuthal direction, the nonlinear source term simplifies to:

$$\hat{q}_{LES} = FFT\left(\frac{\rho' \nabla p'}{\bar{\rho}(\bar{\rho} + \rho')} - \boldsymbol{u'} \cdot \nabla \boldsymbol{u'}\right). \tag{3.3}$$

To evaluate the physical relevance of the optimal and sub-optimal input modes resulting from our analysis, we compute this source term directly from high-fidelity LES data. The input modes are physically relevant if they capture at least a portion of the spatio-temporal behavior of the LES forcing. This is quantified by projecting the LES forcing onto the basis of input modes:

$$a_n = \langle \hat{q}_{LES}, q_{in,n} \rangle . \tag{3.4}$$

Here, a_n denotes the amplitude of input mode $q_{in,n}$ in the LES forcing. Figure 3.10 shows amplitudes $|a_n|$ resulting from this process at forcing frequency $St = 0.33$ and

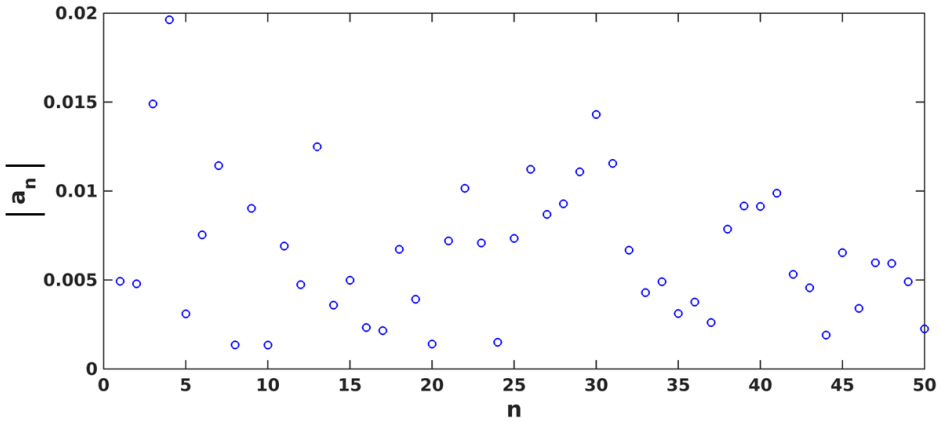

Figure 3.10: Amplitudes $|a_n|$ determined by projecting the LES forcing onto the basis of input modes for $M_j = 1.5$ at $St = 0.33$.

azimuthal wavenumber $m = 0$. Here, the amplitudes are normalized by the average amplitude of the LES source. Overall, less than 0.3% of the energy contained in the LES source is projected onto the input modes. This agrees with the observation that only a small fraction of the overall aerodynamic energy in a turbulent jet is ever radiated as sound [8]. We also note that the amplitudes of many sub-optimal modes are larger than the amplitude of the optimal mode. This indicates that sub-optimal input modes are physically relevant, and should not be neglected.

To quantify the effect of sub-optimal input modes, we use effective gains by modulating the white-noise gains by the amplitudes resulting from the LES projection:

$$\sigma_{eff,n} = \sigma_n a_n. \tag{3.5}$$

The total energy in the output is computed as the sum of squares of the effective gains, resulting in a total increase in the output SPL of $0.53dB$ by including the sub-optimal modes. Because the decibel scale is logarithmic, this represents a significant increase

compared to $\Delta SPL = 0.16dB$, obtained with white noise forcing. In summary, we find sub-optimal modes to be even more relevant in the presence of realistic forcing than they are in the case of white noise forcing.

3.3.3 Reconstruction of an acoustic field by output modes

To assess the physical relevance of output modes, we compare them to the acoustic far-field predicted by the LES [92]. For this purpose, we employ the Kirchhoff method to project near-field pressure fluctuations from the LES outwards, away from the jet [18]. This is necessary because the LES domain is smaller than the domain considered for the output modes. After computing the acoustic field associated with the LES over the entire output domain, this field is then projected onto the orthogonal set of output modes. Similar to equation (3.4), amplitudes associated with output modes are determined by:

$$b_n = \langle p_{LES}, p_{out,n} \rangle \,. \tag{3.6}$$

Figure 3.11 shows the amplitudes $|b_n|$ vs. output mode number. For this supersonic jet, we find that optimal output mode is most prevalent in the LES acoustic data. As shown in figure 3.4, the optimal mode consists of a single acoustic beam at the Mach wave angle. From equation (3.6), we find that this mode accounts for 57% of the acoustic energy in the output domain.

By including more output modes, we recover even more of the acoustic output energy. Figure 3.12 shows the dependence of the recovered acoustic energy on the number of retained output modes. A superposition of 24 output modes recovers almost 70% of the acoustic energy of the LES. Therefore, even though the input modes capture only a small portion of the nonlinear source term, the acoustic field of the corresponding output modes reliably captures the results of a nonlinear simulation. This implies that

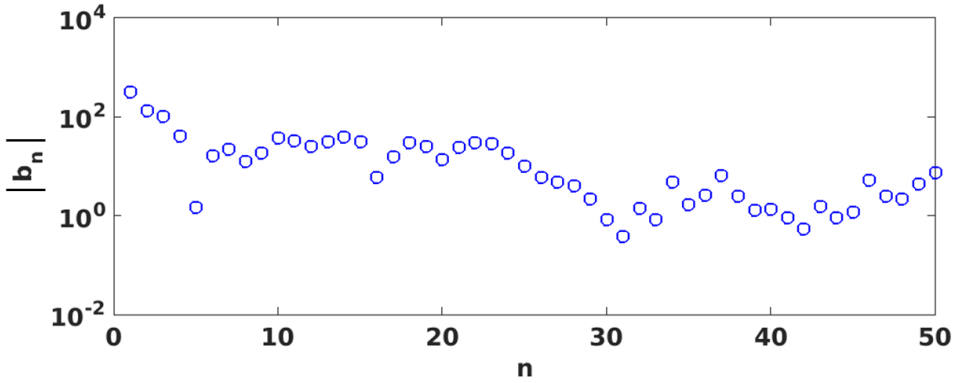

Figure 3.11: Amplitudes $|b_n|$ determined by projecting LES acoustic field onto the orthonormal basis of output modes.

the input modes must indeed capture the small, but radiating portion of the nonlinear source term.

While the output modes successfully recover a large portion of the acoustic energy, the agreement is not perfect. Because input-output analysis is linear, possible nonlinear interactions between input modes leading to far-field sound are neglected. Also, by restricting the input forcing to the velocity equations (2.31), we neglect forcing applied to the pressure equation (2.30) which also may lead to far-field sound. In other words, a part of the LES acoustic field may arise from sources that are not present in our current formulation. Nevertheless, it is striking that 70% of the acoustic energy can be recovered by introducing forcing only to the linearized velocity equations.

Figure 3.12 shows that including more than 24 output modes in the superposition has little effect on how well the LES acoustic field is approximated. Mode number 24 also coincides with the drop off in gains shown in figure 3.9. This implies that an input-output system comprised of just 24 modes is sufficient to represent the noise generation mechanisms in an $M_j = 1.5$ jet at frequency $St = 0.33$ and azimuthal wave number $m = 0$. This offers a substantial reduction compared to the spatial discretization of

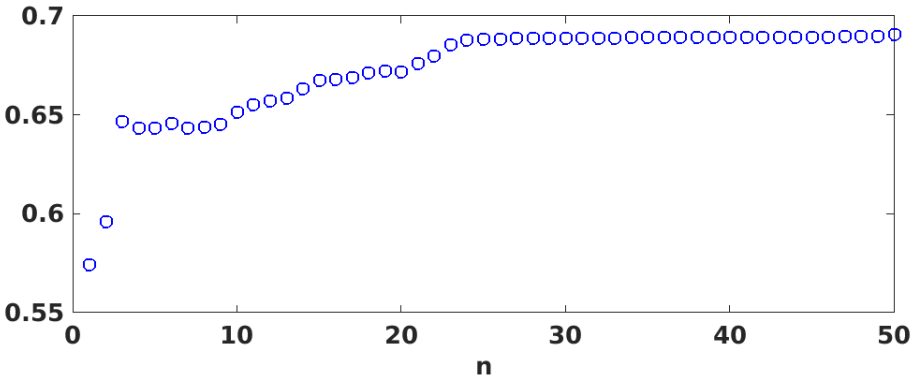

Figure 3.12: Recovered acoustic energy as a function of number of retained output modes.

the original system of equations having almost a half million degrees of freedom. This information can be used to obtain reduced-order models of noise generation.

To further understand the effect of including sub-optimal modes on the acoustic far-field, we use the Kirchhoff method to project both the LES data and the superposition of 24 output modes yet further into the far-field. Figures 3.13(a) and 3.13(c) show the decibel levels as a function of axial and radial position for the LES and output-mode-reconstructed acoustic field, respectively. The black circular arc indicates a distance of 100 jet radii away from the nozzle exit. Figure 3.13(b) shows an acoustic field reconstructed from only the first output mode. An acoustic beam at the Mach wave angle is visible in all three figures. Sideline and upstream acoustic radiation are markedly absent, however, from figure 3.13(b). Clearly, inclusion of the sub-optimal modes recovers this missing sideline and upstream sound, in good agreement with the LES acoustic field.

We quantify this contribution of the sub-optimal modes in figure 3.14 by plotting the SPL difference between the fields shown in figures 3.13(b) and 3.13(c) as a function of polar angle ϕ from the downstream jet axis along the black circular arc. We find

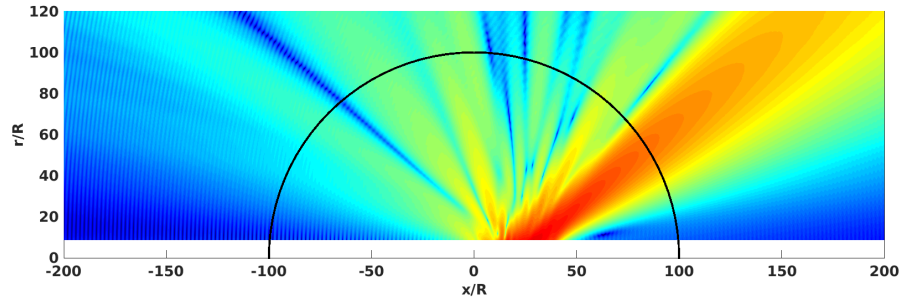

(a)

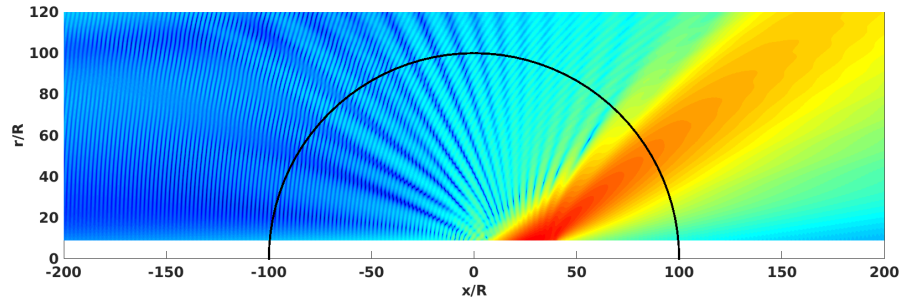

(b)

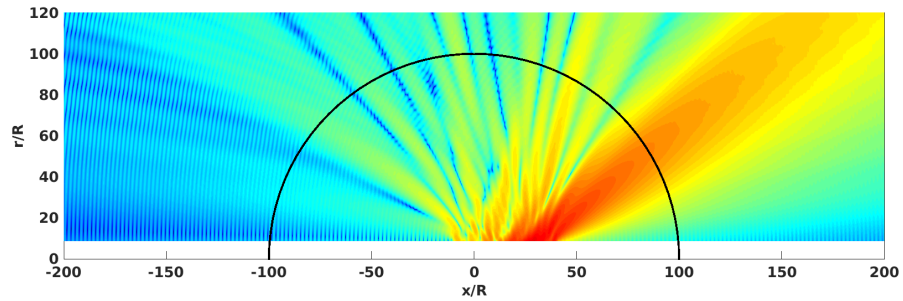

(c)

Figure 3.13: Contours of decibel levels of (a) the LES acoustic field, (b) the acoustic field of the first output mode alone, and (c) an acoustic field reconstructed from a superposition of 24 output modes. The black arc indicates a distance of 100 jet radii away from the center of the jet nozzle.

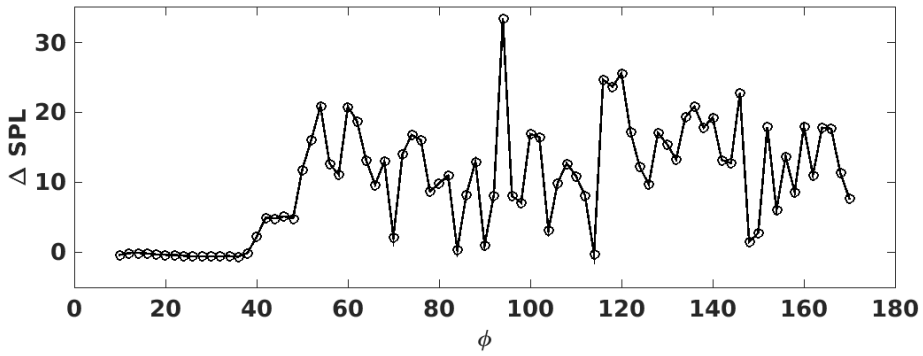

Figure 3.14: Increase in far-field sound pressure levels owing to sub-optimal modes as a function of polar angle ϕ from the downstream jet axis.

that for $\phi > 40°$, sub-optimal modes account for a 10 to $20dB$ increase over levels of the optimal mode alone. We therefore conclude that sub-optimal modes are associated with sideline noise. Unlike stochastic models [93], however, the sideline noise created by sub-optimal modes arises from coherent motions. Furthermore, owing to the similarities between figure 3.13(a) and figure 3.13(c) we suggest that a large part of sideline noise can be explained by such coherent motions embedded in the jet.

3.3.4 Summary

In summary, by projecting the LES source term data onto input modes (in section 3.3.2) and the LES acoustic far-field onto output modes (in section 3.3.3), we demonstrated that both types of modes are physically relevant. We also found that input-output analysis reveals the minimum dimensionality required of reduced-order models to accurately represent the mechanisms of acoustic generation. Finally, in comparison to the optimal output mode we have found that sound recovered by sub-optimal modes is directed mostly in the sideline and upstream directions. As such, sub-optimal modes provide a new interpretation of sideline noise in terms of coherent motions.

Chapter 4

Wavepacket modeling of far-field acoustics

4.1 Introduction

In the previous chapter we projected the high-fidelity LES data onto the orthonormal set of output modes to investigate the physical relevance of them under realistic forcings. We showed that only few coherent output modes recovered almost 70% of the LES acoustic energy, which was very striking. While the results in the previous chapter are insightful, in this chapter we further develop our method to directly handle the far-field observers within input-output analysis framework.

We therefore specify the matrix C to directly sample far-field pressure by incorporating a projection method within itself. In the previous chapter we employed the Kirchhoff method, which is equivalent to the wave equation. It was thus unable to locate a projection surface in the region close enough to the near-field; with combining stretched meshes in the radial direction, this might cause difficulties in fully capturing high frequency waves. Alternatively, in this chapter we use the FW-H method to

manage a projection surface close to the acoustic source region.

The rest of this chapter is organized as follows. A new hybrid input-output/FW-H method is introduced in section 4.2.1. The resulting singular values and corresponding input and unrestricted output modes are shown subsequently in section 4.2.2 for supersonic isothermal and heated jets. Next, we reconstruct the far-field acoustics by retaining few output modes and compare them to those predicted by the LES in section 4.2.3. Finally, in section 4.2.4 we obtain acoustic spectra by repeating input-output analysis over a wide range of frequencies to examine whether our analysis recovers the traditional similarity spectra of turbulent jets. The results presented in this chapter has been published in [94] and reproduced by permission of the American Institute of Aeronautics and Astronautics, Inc.

4.2 Far-field pressure projection

4.2.1 Hybrid input-output/FW-H method

For a stationary source in a medium at rest, the permeable surface FW-H equation [1, 33, 95] is given by:

$$\left(\frac{\partial^2}{\partial t^2} - c_\infty^2 \frac{\partial^2}{\partial x_i \partial x_j}\right)\left[\left(\rho - \rho_\infty\right) H\left(S\right)\right] = \frac{\partial}{\partial t}\left[Q_n \delta\left(S\right)\right] - \frac{\partial}{\partial x_i}\left[F_i \delta\left(S\right)\right] - \frac{\partial^2}{\partial x_i \partial x_j}\left[T_{ij} H\left(S\right)\right], \tag{4.1}$$

where Q_n, F_i, and T_{ij} are defined as

$$Q_n = \rho u_i \hat{n}_i, \tag{4.2}$$

$$F_i = \left(P_{ij} + \rho u_i u_j\right) \hat{n}_j, \tag{4.3}$$

$$T_{ij} = \rho u_i u_j + P_{ij} - c_\infty^2 \left(\rho - \rho_\infty\right) \delta_{ij}. \tag{4.4}$$

Here, the function S defines the surface so that a solution to equation (4.1) is sought outside of the surface $S = 0$, and in this regard the Heaviside function becomes unity for $S > 0$ and zero for $S < 0$. Furthermore, $\hat{n}_i$ represents a unit outward normal vector to the surface $S = 0$, and u_i is the local fluid velocities on the surface $S = 0$. The total density is given by ρ while the ambient properties are denoted by the subscript ∞ in the above equations. The perturbation properties may be then represented by the superscript $'$ such that the density perturbation is written as $\rho' = \rho - \rho_\infty$. Equation (4.4) is the Lighthill stress tensor, which was already introduced in chapter 1, but it should be noted that the compressive stress tensor P_{ij} here is defined as $P_{ij} = \left(p - p_\infty\right) \delta_{ij}$ after neglecting the viscous term.

To perform the Fourier analysis, equation (4.1) may be rewritten in a convenient form as:

$$\left(\frac{\partial^2}{\partial x_j \partial x_j} + k^2\right) \left[\left(c_\infty^2 \tilde{\rho'}\right) H\left(S\right)\right] = -\mathrm{i}\omega \tilde{Q}_n \delta\left(S\right) + \frac{\partial}{\partial x_i}\left[\tilde{F}_i \delta\left(S\right)\right] - \frac{\partial^2}{\partial x_i \partial x_j}\left[\tilde{T}_{ij} H\left(S\right)\right], \tag{4.5}$$

where the wavenumber k is given by $k = \omega / c_\infty$ with the ambient speed of sound c_∞. In fact, we may replace the term $c_\infty^2 \tilde{\rho'}$ by the pressure perturbation p' and write equation (4.5) in a pressure-based form since the density perturbations are small outside of the source region [35]. The integral solution is then, given by:

$$\tilde{p'}\left(\boldsymbol{x}, \omega\right) = -\int_S \tilde{F}_i\left(\boldsymbol{y}, \omega\right) \frac{\partial G\left(\boldsymbol{x}, \boldsymbol{y}\right)}{\partial y_i} dS - \int_S \mathrm{i}\omega \tilde{Q}_n\left(\boldsymbol{y}, \omega\right) G\left(\boldsymbol{x}, \boldsymbol{y}\right) dS, \tag{4.6}$$

assuming that the volume-distributed source terms are negligibly small. Here, the three-dimensional free-space Green's function G is given by:

$$G(\boldsymbol{x}, \boldsymbol{y}) = \frac{-e^{-\mathrm{i}kr}}{4\pi r} \tag{4.7}$$

where r represents the distance between the source $\boldsymbol{y}$ and the observer $\boldsymbol{x}$ such that $r = |\boldsymbol{x} - \boldsymbol{y}|$. Using the chain rule, the derivative of the Green's function with respect to the source $\boldsymbol{y}$ may be then evaluated as

$$\frac{\partial G}{\partial y_i} = \frac{\partial G}{\partial r}\frac{\partial r}{\partial y_i}, \tag{4.8}$$

and in cylindrical coordinates we use here, $\frac{\partial r}{\partial y_i}$ is simply:

$$\frac{\partial r}{\partial y_i} = -\hat{r}_i = \frac{x_i - y_i}{|x_i - y_i|}. \tag{4.9}$$

Now we linearize the integral solution in equation (4.6) to implement an FW-H solver within input-output analysis framework. Since outside of the hydrodynamic region, local properties are mostly perturbation properties, we may neglect the second-order terms in the dipole source term F_i and rewrite it as:

$$F_i = P_{ij}\hat{n}_j. \tag{4.10}$$

The linear monopole source term Q_n remains unchanged.

Since we consider a linearized system, the source terms to the FW-H equations are also linear. We therefore treat them explicitly so that we can write the FW-H formulation as a linear operator inside the matrix C. In this way the adjoint of the matrix C takes far-field pressure fluctuations and maps these back onto state vectors

on the FW-H surface.

Since the FW-H solver is linearized, a projection surface should be placed in purely acoustic region that is sufficiently far from the jet turbulence. In this sense, while linear input-output analysis may place it closely to the source region, the location of a projection surface needs to be carefully determined when we project near-field LES data to the far-field. To ensure that we are in the linear regime in LES, we choose a straight cylindrical FW-H surface at 6 jet radii away from the jet exit whose axis lies along the jet centerline. The projection surface is thus located much closer to the jet than the Kirchhoff surface in section 3.3.1 was and yet it is far enough to enclose all noise sources. The FW-H surface extends from $x/R = -10$ to $x/R = 60$ and has an open outflow disk. We assume that the projection surface is sufficiently long and lean that spurious modes will not contaminate the acoustic response even without closing a disk.

We examine the far-field pressure along an arc positioned at a distance of 200 jet radii from the nozzle exit. The observers are distributed with uniform spacing along an arc, ranging from $\phi = 10^\circ$ to $\phi = 150^\circ$ where the polar angle ϕ is measured from the downstream jet axis. These angles are determined by the extent of the FW-H surface with respect to the center of the nozzle exit. It should be noted that upstream and downstream sponge layers are employed at $x/R = -10$ and $x/R = 60$, respectively, to prevent outgoing waves from reflecting back. For this reason, the choice of arc is also made to exclude regions outside of the sponge layers to avoid spurious modes. Figure 4.1 shows a schematic representation of this hybrid input-output/FW-H method.

4.2.2 Input and unrestricted output modes

In this chapter, the dynamics of small perturbations around RANS base flows are governed by the LNS equations. To account for the effects of eddy viscosity, we consider

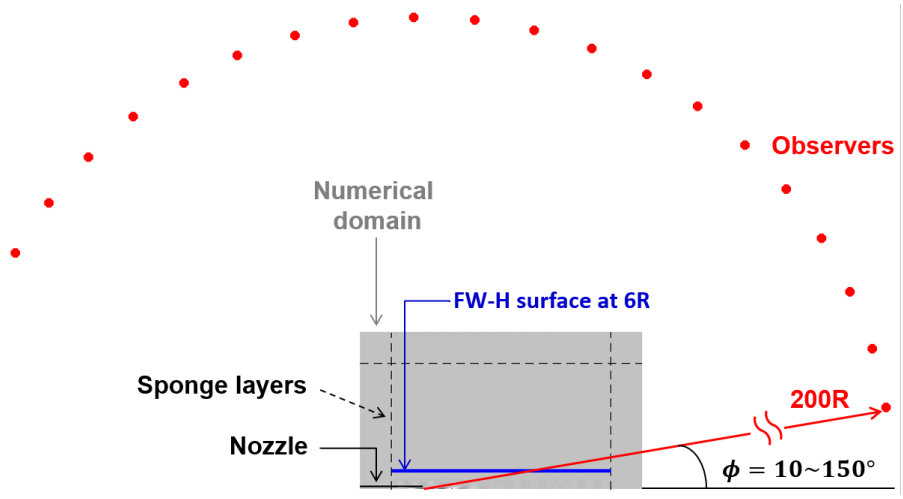

Figure 4.1: A schematic representation of the hybrid FW-H/input-output analysis method. A straight cylindrical FW-H projection surface is located at $x/R = 6$, denoted by a blue straight line. Red dots indicate observers distributed uniformly along an arc in far-field from $\phi = 10°$ to $\phi = 150°$.

the effective viscosity solutions of RANS base flow, which are incorporated within the LNS equations. We therefore recover tilted vortex structures near the nozzle walls in input modes. Further details about the effects of eddy viscosity are provided later in section 6.3. While the output domains are now restricted to an arc at a distance of 200 jet radii from the nozzle exit, the input domains still remain unchanged such that $-10 < x/R < 60$ and $r/R < 2.90$.

Figure 4.2 shows the first four input modes for the $M_j = 1.5$ isothermal jet. In the figure the gray rectangle represents the finite nozzle and the black lines indicate the extent of the input domain. Singular values and few unrestricted output modes are also shown in figure 4.3 and figure 4.4, respectively. While the output domains are now restricted to an arc at a distance of 200 jet radii away from the nozzle exit, we still obtain unrestricted output modes, i.e., the entire system state before the output matrix C is applied. These modes extend to the entire numerical domain, and are later projected to

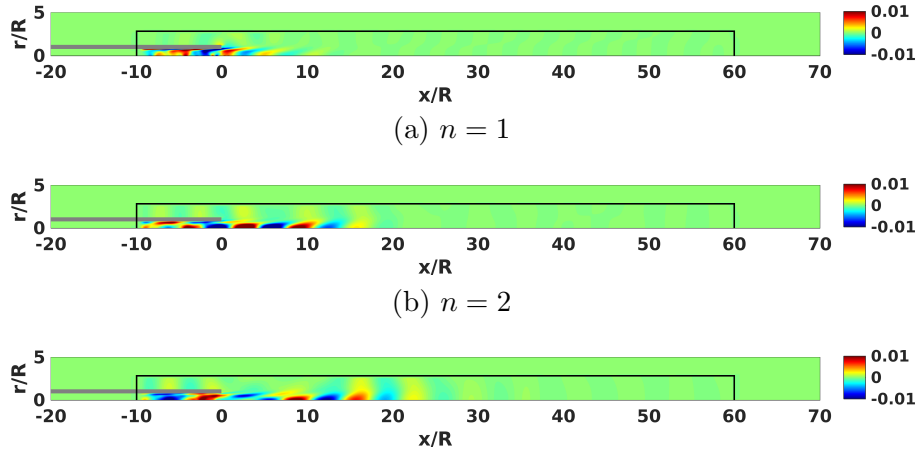

(a) $n = 1$

(b) $n = 2$

(c) $n = 3$

Figure 4.2: The first three input modes of the $M_j = 1.5$ isothermal jet for forcing frequency $St = 0.33$. Contours of the real part of the normalized axial velocity forcing are shown.

an arc in the far-field. As shown in these figures, input-output modes and gains follow similar patterns observed in analysis of the LEE in the previous section. In figure 4.2 input modes extend farther downstream as the mode number increases. Figure 4.3 shows the optimal mode still dominates the acoustic response, and a plateau over several mode numbers is reported before a sudden drop in singular values. In figure 4.4, as the mode number increases we find an increasing number of acoustic beams, which rotate towards the sideline direction and the jet centerline. New beams form between such diverging beams. Here, black dotted lines in figures represent the location of sponge layers.

We repeat input-output analysis for the $M_j = 1.5$ supersonic heated jet with the jet-to-ambient temperature ratio $T_j/T_\infty = 1.74$. Figures 4.5 and 4.6 visualizes the first three input and output modes, respectively, which correspond to three largest singular values in figure 4.7. Overall, they follow the same pattern observed in the case of isothermal jet. Note that at the same forcing frequency examined for the isothermal

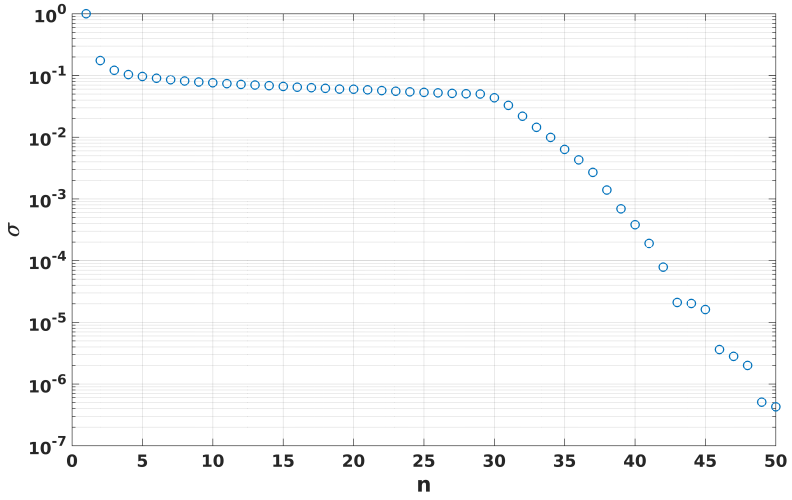

Figure 4.3: Singular values vs. mode number n for the $M_j = 1.5$ supersonic isothermal jet at forcing frequency $St = 0.33$ with the azimuthal mode number $m = 0$.

jet, the relative gain of optimal mode increases for the heated jet since the Mach wave radiation becomes more active with jet heating. Moreover, the dropoff location of the singular values for the heated jet is delayed to $n = 38$ compared to $n = 30$ for the isothermal jet. The shift is expected from the fact that the acoustic Mach number increases with applied heating so the wavelength of waves which may reside in the input domain decreases. This may allow a greater number of modes with significant gains within the domain of the same size.

4.2.3 Reconstructed far-field acoustics

To assess how well output-modes-reconstructed far-field acoustics captures acoustic energy of an LES, a high-fidelity LES database is projected onto the orthonormal set of output modes. The LES database is processed in the same way as described in section 3.3.1. Since the original LES was performed for a smaller computational domain,

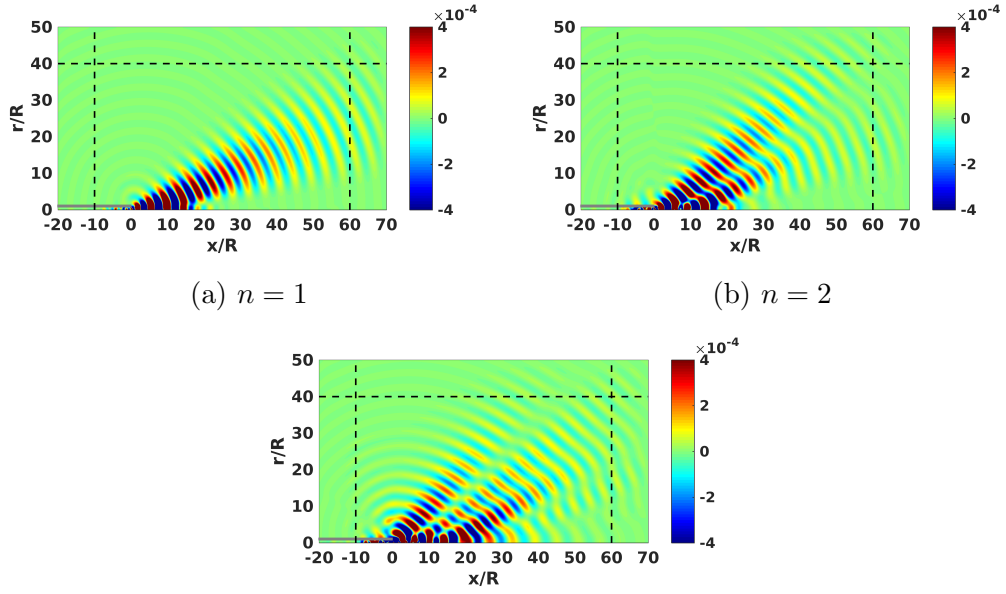

(a) $n = 1$

(b) $n = 2$

(c) $n = 3$

Figure 4.4: Output modes corresponding to the first three largest singular values for the $M_j = 1.5$ supersonic isothermal jet at forcing frequency $St = 0.33$ with the azimuthal mode number $m = 0$. Contours visualize the real part of normalized output pressure fluctuations. Black lines indicate the extent of sponge layers.

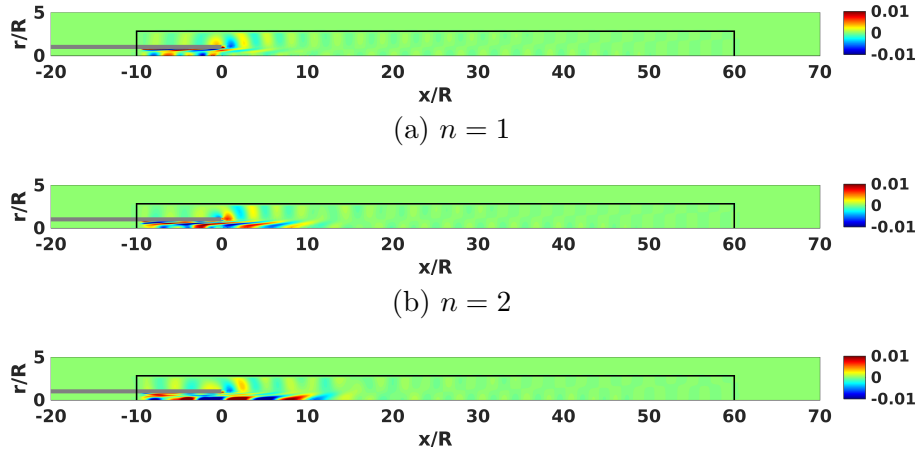

(a) $n = 1$

(b) $n = 2$

(c) $n = 3$

Figure 4.5: The first three input modes of the $M_j = 1.5$ supersonic heated jet with $T_j/T_\infty = 1.74$ for forcing frequency $St = 0.33$. Contours of the real part of the normalized axial velocity forcing are shown.

the LES database is also projected to an arc at 200 radii from the jet exit. In this chapter we do this using the FW-H method instead of the Kirchhoff method. We examine the acoustic response at forcing frequency $St = 0.33$ or equivalently, $St_a = 0.5$.

Figure 4.8 shows the recovered acoustic energy as a function of the number of retained output modes. Strikingly, a superposition of only 30 output modes captures more than 90% of the LES acoustic energy. Compared to the results obtained using the rectangular output domain, this is a significant improvement. One may also notice that we include sub-optimal modes up to $n = 30$ where the singular values fall off after a long plateau as shown in figure 4.3.

The new hybrid input-output/FW-H method successfully captures almost all LES acoustic energy and we now reconstruct the far-field acoustics as described in figure 4.9. In this figure the acoustic fields reconstructed by the LES (black line with squares), by the optimal mode alone (blue line with circles), and by retaining the first 30 modes (red

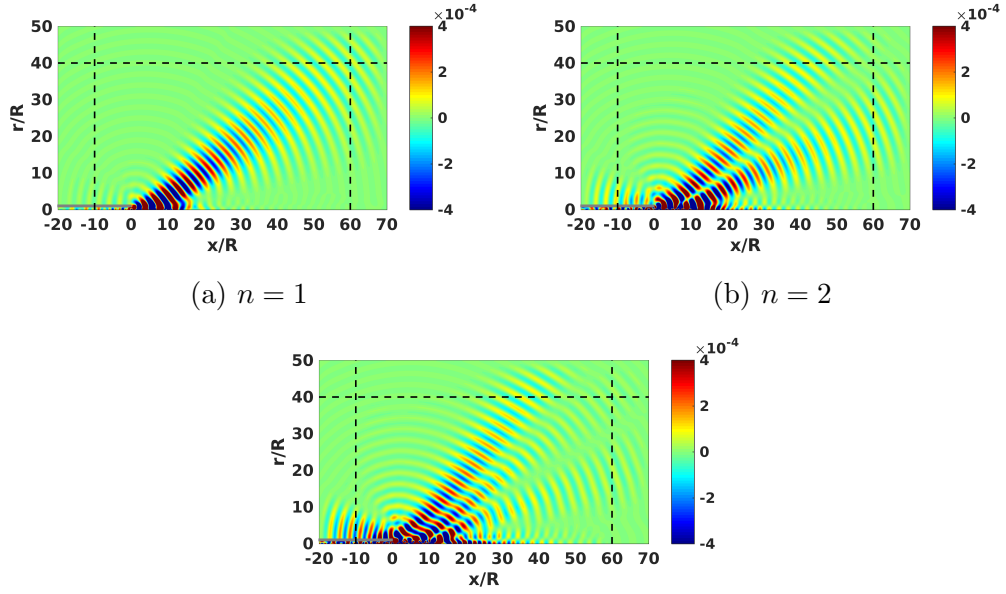

(a) $n = 1$

(b) $n = 2$

(c) $n = 3$

Figure 4.6: Output modes corresponding to the first three largest singular values for the $M_j = 1.5$ supersonic heated jet with $T_j/T_\infty = 1.74$ at forcing frequency $St = 0.33$ with the azimuthal mode number $m = 0$. Contours visualize the real part of normalized output pressure fluctuations. Black lines indicate the extent of sponge layers.

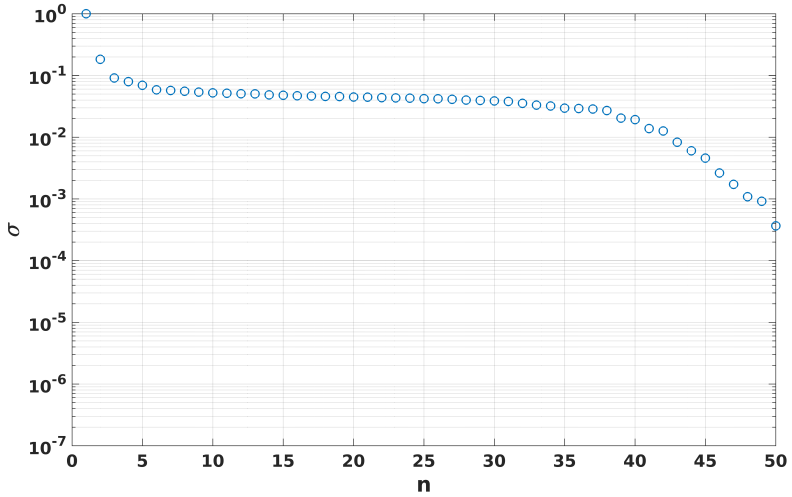

Figure 4.7: Singular values vs. mode number n for the $M_j = 1.5$ supersonic heated jet with $T_j/T_\infty = 1.74$ at forcing frequency $St = 0.33$ with the azimuthal mode number $m = 0$.

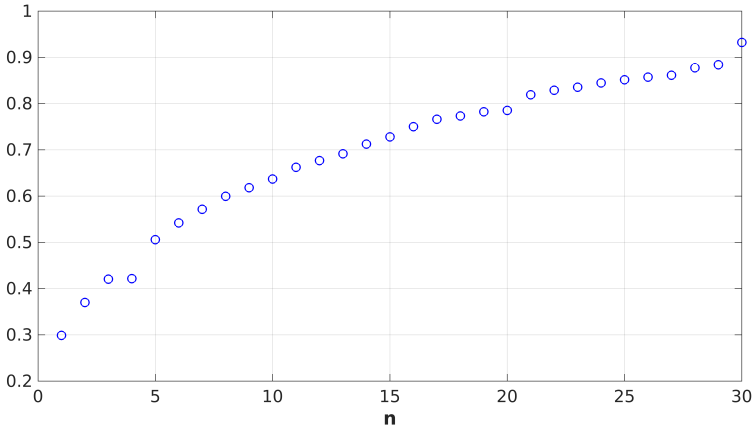

Figure 4.8: Recovered acoustic energy as a function of the number of retained output modes for the $M_j = 1.5$ isothermal jet at forcing frequency $St = 0.33$.

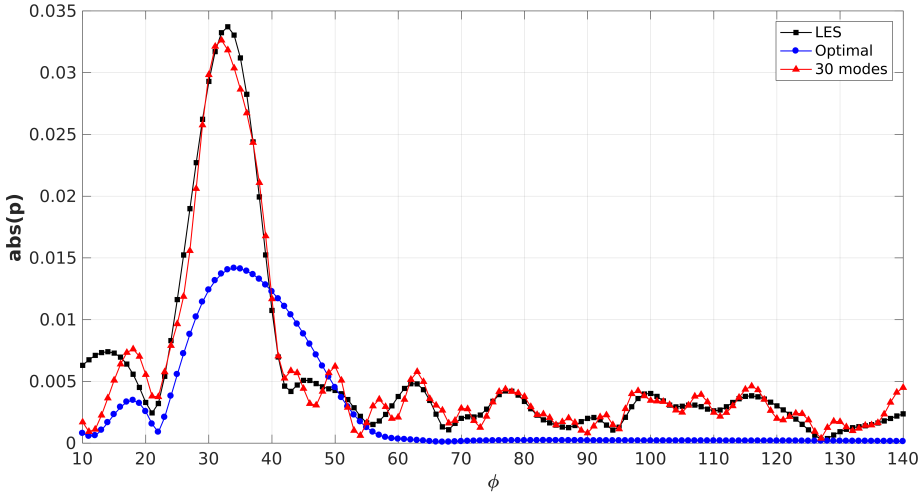

Figure 4.9: Directivity pattern of the LES acoustic field (black), reconstructed acoustic field by the optimal output mode alone (blue), and acoustic field reconstructed from a superposition of 30 output modes (red) measured at a distance of 200 jet radii away from the jet exit for the $M_j = 1.5$ isothermal jet.

line with triangles) are placed in one plane. With the optimal mode alone, only about 30% of the LES acoustic energy can be recovered. Also, the optimal mode entirely misses sideline and upstream propagating noise. Inclusion of 30 sub-optimal modes, however, correctly captures the directivity of the LES acoustic energy. In other words, input-output analysis may model the turbulent jet noise, and this supports one coherent source mechanism for turbulent jets. Sideline noise may also be explained in terms of non-compact but coherent sources, which is given by input modes as shown in figure 4.2.

In addition to isothermal jets, we also test effects of heating on input-output analysis of turbulent jets later in section 6.2. As will be discussed in detail in that section, we find that input modes are indeed active in the presence of realistic forcing. We observe that, even though applied heating seems to magnify the significance of the optimal mode under the assumption of uniform forcing such as white noise, sub-optimal modes

become even more relevant in the presence of realistic forcing extracted from a high-fidelity LES database. In this sense, we investigate whether output modes recover a significant portion of an actual LES acoustic field even for heated jets.

We examine small perturbations about the base flow for heated jet at forcing frequency $St = 0.33$, i.e., $St_a = 0.66$. By projecting an LES database for the $M_j = 1.5$ supersonic heated jet with $T_j/T_\infty = 1.74$ onto a set of ooutput modes, we obtain the recovered acoustic energy as a function of the number of retained output modes in figure 4.10. Also, the directivity pattern is presented in figure 4.11. In this case we need more output modes (38 modes) than in the case of isothermal jet since the dropoff in gains is delayed as a result of applied heating. Compared to the isothermal case, the optimal mode alone recovers less than 10% of the LES acoustic energy. By including 38 modes, however, almost 95% of the LES acoustic energy is captured. Furthermore, as shown in figure 4.11 the directivity is predicted more accurately for the heated jet than for the isothermal jet above. This confirms again that sub-optimal modes are physically relevant under the realistic forcing and therefore, input-output analysis can be used to model heated turbulent jets.

4.2.4 Modeling similarity spectra

In this section we repeat input-output analysis over a range of frequencies to investigate the resulting acoustic spectra for the $M_j = 1.5$ isothermal jet. We consider axisymmetric and higher azimuthal wavenumber modes (up to m = 2) at each frequency. For low frequencies $St < 1$ and at low polar angles, it is known that sound generated from turbulent jets are successfully captured by the first three azimuthal components only [51, 52, 63, 96]. At larger polar angles, however, higher azimuthal modes become more important. The effects of higher azimuthal wavenumber modes are discussed more thoroughly later in section 6.4.

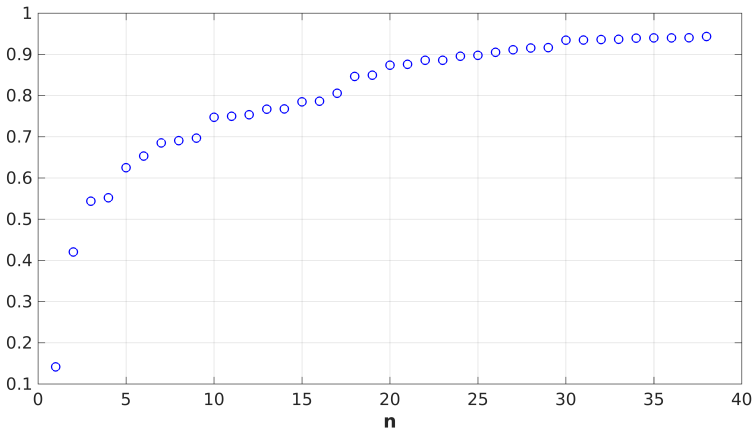

Figure 4.10: Recovered acoustic energy as a function of the number of retained output modes for the $M_j = 1.5$ heated jet with the jet-to-ambient temperature ratio $T_j/T_\infty = 1.74$ at forcing frequency $St = 0.33$.

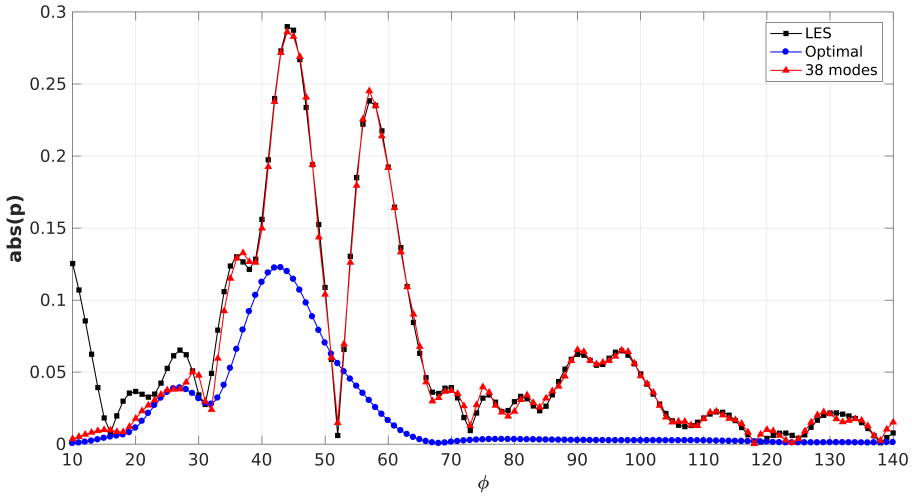

Figure 4.11: Directivity pattern of the LES acoustic field (black), reconstructed acoustic field by the optimal output mode alone (blue), and acoustic field reconstructed from a superposition of 30 output modes (red) measured at a distance of 200 jet radii away from the jet exit for the $M_j = 1.5$ heated jet with the jet-to-ambient temperature ratio $T_j/T_\infty = 1.74$.

For each azimuthal wavenumber and at each frequency, the acoustic field at a distance of 200 jet radii away from the nozzle exit is obtained using the FW-H solver implemented within the input-output analysis framework. Assuming all input modes are uniformly forced (white noise forcing), we superpose the most significant output modes, starting with the optimal mode and continuing to the dropoff of the singular values. Since azimuthal wavenumber modes are orthogonal, the resulting acoustic fields are easily superposed to complete the total spectra. We repeat this process for two different radiation angles of $\phi = 30^\circ$ and $\phi = 90^\circ$. Although we include only the first three azimuthal modes, our analysis recovers a broadening of the far-field acoustic spectra as the radiation angle increases as shown in figure 4.12. The downstream spectrum is peaky, reminiscent of the large-scale similarity spectrum (F) that fits a range of experimental measurements [93]. At high frequencies, the spectrum at $\phi = 90^\circ$ drops off less quickly, similar to the behavior of the fine-scale similarity spectrum (G). For low frequencies, however, acoustic spectrum at $\phi = 90^\circ$ differs from the G spectrum and, in fact, drops off almost as sharply as the F spectrum. Similar results have also been reported in other wavepacket modeling approaches [97]. These results suggest that sideline also may be explained in terms of large-scale noise using relatively few coherent modes [52, 97]. Moreover, our model provides a first principles-based approach to construct far-field acoustic spectra over a broad range of directivity angles and to understand them in terms of non-compact sources resembling wavepackets.

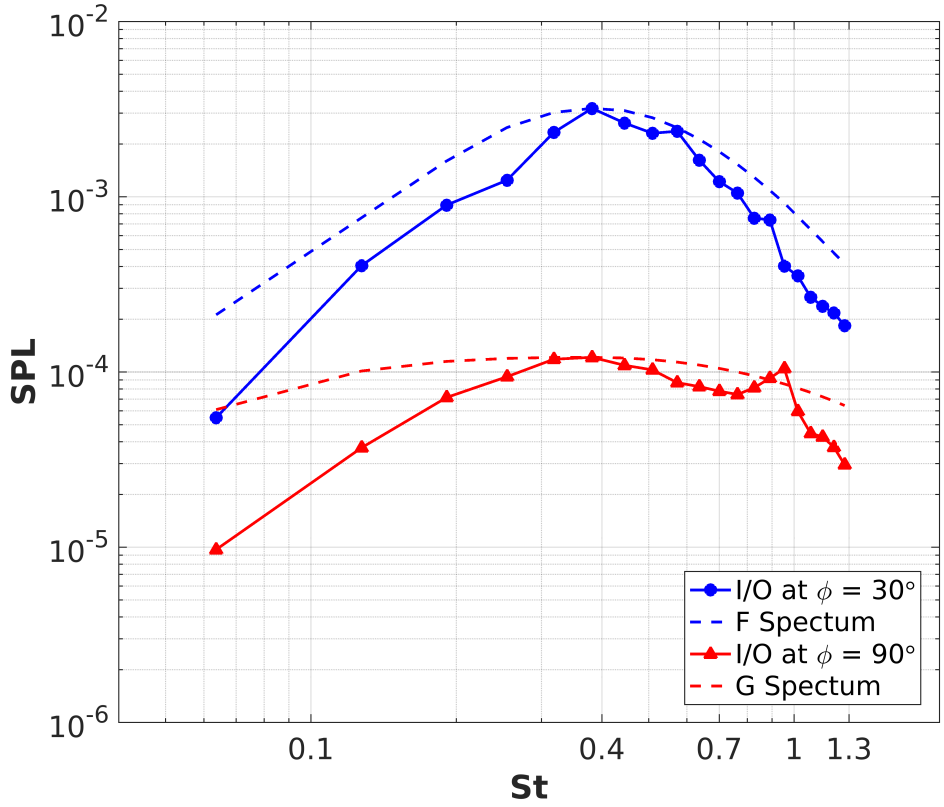

Figure 4.12: Far-field acoustic spectra measured at a distance of 200 jet radii away from the nozzle exit obtained for $m = 0$, 1, and 2 for the $M_j = 1.5$ isothermal jet. As the radiation angle ϕ increases, input-output analysis recovers a broadening of the acoustic spectra.

Chapter 5

Modeling near-field wavepackets as acoustic sources

5.1 Introduction

In this chapter we focus on an ideally expanded, isothermal, axisymmetric $M_j = 0.9$ subsonic turbulent jet, matching the conditions of the experiment used as a basis for the stochatic similarity wavepacket model [97, 98] and those of the high-fidelity LES performed by Brès et al. [21]. Like supersonic jets, $M_j = 0.9$ subsonic jets support instability waves and wavepackets can be predicted by stability analysis based on either the PSE or the LEE [4]. Wavepackets, however, seem to underpredict the sound generated by subsonic jets, particularly in the sideline direction [4, 61]. This underprediction is partially rectified by introducing either jitter or a decoherence scale into the model [4, 51, 56, 99]. The stochastic similarity wavepacket model incorporates these effects through a randomized superposition of coherent wavepackets, which, by fitting, can closely reproduce experimentally measured far-field acoustic spectra [97]. Applying

input-output analysis, we found acoustic source terms may be linked to several sub-optimal modes in addition to the wavepacket in chapters 3 and 4. The sub-optimal modes were especially important for subsonic jets. For this reason, we focus upon $M_j = 0.9$ jet in this chapter. We will provide an interpretation of the physics behind optimal and sub-optimal acoustic sources predicted by input-output analysis and use this to explain the sound generation mechanisms of subsonic jets. Part of the results presented in this chapter is to appear in [100] and is also in preparation for future publication [101].

5.2 Base flow

Figure 5.1 shows contours of axial velocity from a RANS solution of the jet, computed using a modified $k-\varepsilon$ turbulence model with coefficients suggested by Thies and Tam [90]. Flow configurations follow those described in chapter 2, but the geometry is now normalized by the jet diameter $D = 1$, instead of the radius R. In this figure, the flow exhausts from a straight cylindrical nozzle with inner diameter D and finite thickness $t = 0.1D$, which is denoted by a white line. Along the wall, no-slip boundary conditions are employed, allowing boundary layers to grow as the flow travels downstream. The upstream boundary conditions are chosen to produce the desired jet exit velocity, pressure, and temperature at $x/D = 0$. In terms of the jet diameter D, the jet Reynolds number is given by $Re = \rho_j u_j D/\mu = 2 \times 10^5$, where μ is the constant dynamic viscosity across the full numerical domain. Here, ρ_j and u_j are respectively the density and the velocity at the nozzle exit as in the previous chapters. While figure 5.1 visualizes only part of it, the actual computational domain spans from $x/D = -10$ to $x/D = 40$ in the axial direction and from $r/D = 0$ to $r/D = 25$ in the radial direction. Sponge layers are employed at $x/D = -5$, $x/D = 35$, and $r/D = 20$.

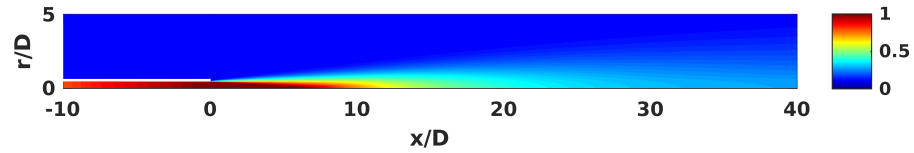

Figure 5.1: Contours of axial velocity from a RANS solution of a round $M_j = 0.9$ subsonic jet. The velocity contours are normalized by the velocity at the nozzle exit at $x/D = 0$.

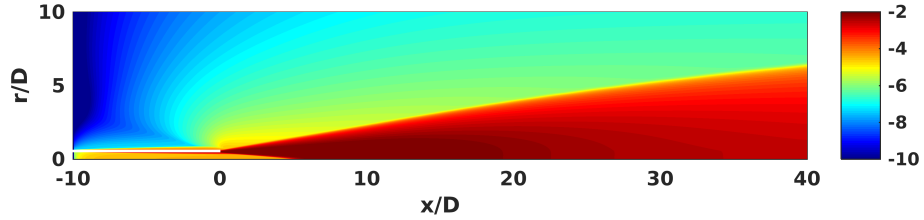

Figure 5.2: Contours of the TKE for the $M_j = 0.9$ subsonic jet in logarithmic scale normalized by the square of the jet exit velocity.

5.3 Turbulent kinetic energy (TKE)-weighted input modes

Physically, in high-speed jets forcings radiating far-field sound come from turbulent motion in jet flows. To ensure this is the case, we weight input forcings by the TKE as shown in figure 5.2, which is evaluated by the same RANS model as used in computing the base flow. In this way only acoustically relevant aerodynamic sources are distilled to investigate input forcings and acoustic response produced by them.

A schematic description of the modified system with TKE-weighted input forcings is given in figure 5.3. By applying the TKE weighting matrix denoted by W_{TKE}, the modified input forcings $\tilde{f}$ are written as:

$$\tilde{f} = W_{TKE} f. \tag{5.1}$$

Here, the matrix A is associated with the LNS equations. The resolvent R remains unchanged since it uniquely depends on the base flow. The matrix C also remains the same as in the previous chapter. In this way the original unweighted system in equations (2.38) and (2.39) becomes:

$$\dot{\boldsymbol{q}} = A\boldsymbol{q} + B\boldsymbol{f} = A\boldsymbol{q} + \tilde{B}\tilde{\boldsymbol{f}}, \tag{5.2}$$

$$\boldsymbol{y} = C\boldsymbol{q}, \tag{5.3}$$

where

$$\tilde{B} = BW_{TKE}^{-1}. \tag{5.4}$$

Because we are interested in output produced by the weighted inputs $\tilde{\boldsymbol{f}}$, we consider a new transfer function $\tilde{H}$ corresponding to the red box in figure 5.3. This new transfer function $\tilde{H}$ is related to the transfer function H in the original, unweighted system such that:

$$\tilde{H} = C(zI - A)^{-1}\tilde{B} = HW_{TKE}^{-1}. \tag{5.5}$$

Consequently, by substituting equations (5.1) and (5.5) into the Arnoldi iteration of $H^{\dagger}H$:

$$\boldsymbol{f}_{new} = H^{\dagger}H\boldsymbol{f} = W_{TKE}\tilde{H}^{\dagger}\tilde{H}W_{tke}\boldsymbol{f} = W_{TKE}\tilde{H}^{\dagger}\tilde{H}\tilde{\boldsymbol{f}}, \tag{5.6}$$

we obtain that:

$$\tilde{\boldsymbol{f}}_{new} = W_{TKE}^{2}\tilde{H}^{\dagger}\tilde{H}\tilde{\boldsymbol{f}}. \tag{5.7}$$

Note that without weighting by the TKE, i.e., when $W_{TKE} = I$, the system returns to the original, unweighted system described in section 2.3.

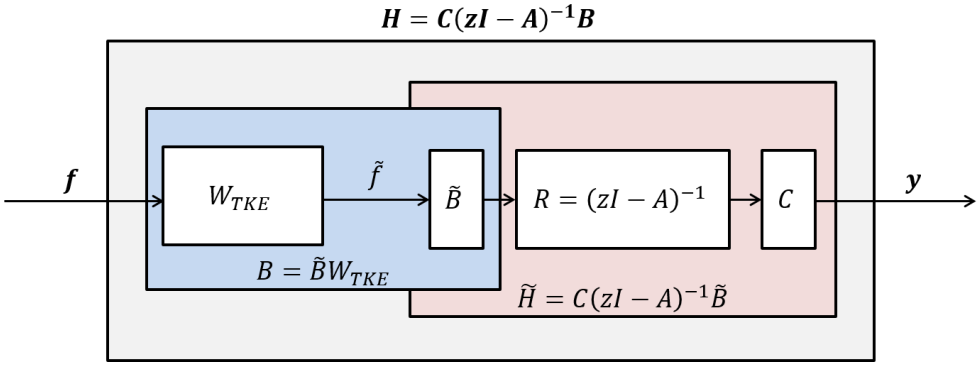

Figure 5.3: A schematic representation of the modified system with the TKE weighting matrix indicated by W_{TKE}.

5.4 Modeling similarity wavepackets

5.4.1 Input and unrestricted output modes

Applying the hybrid input-output/FW-H method, we obtain a spectrum of singular values that represent gains between inputs and outputs. In figure 5.4 we show the first 50 singular values, ordered by amplification factor, for the $M_j = 0.9$ jet at a forcing frequency of $St = 0.59$. For the purposes of this section, which focuses upon the physical meaning of the results of input-output analysis, it is sufficient to consider axisymmetric disturbances ($m = 0$) only. Our input-output formulation can handle higher azimuthal wavenumbers, however, which become important especially to describe noise radiation in the sideline direction. The first 29 singular values show a relatively slow decrease in amplification factor, which means that the first 29 input-output modes produce approximately the same amount of far-field noise per unit energy of forcing. This is consistent with previous results for subsonic jets, where sub-optimal modes were found to produce nearly the same amplification as the optimal mode. This is in contrast, however, to supersonic jets where the optimal mode becomes dominant as shown in section 3.2.

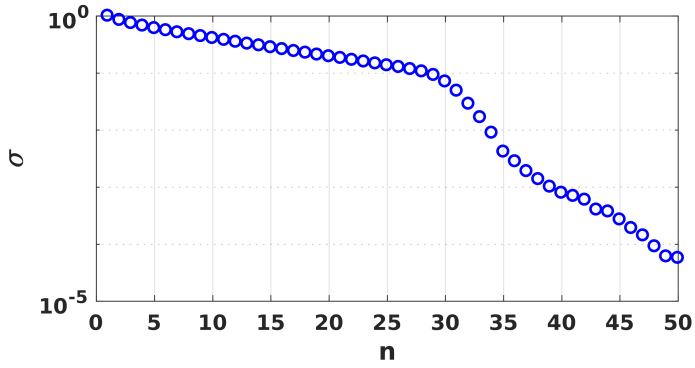

Figure 5.4: Singular values as a function of the mode number for the Mach 0.9 subsonic jet at forcing frequency $St = 0.59$.

Along with the gains, the singular value decomposition also produces orthogonal sets of corresponding input and output modes. Figure 5.5 shows the first four input modes corresponding to the four largest singular values shown in figure 5.4. In figure 5.5, the gray rectangle represents the finite nozzle, which ends at $x/D = 0$. Contours showing the real part of the axial velocity forcing reveal that the input modes to have significant structure. The optimal input mode ($n = 1$), in particular, is clearly a wavepacket. At this frequency, the wavepacket is centered close to the end of the potential core of the jet, and extends several diameters upstream along the jet shear layers as well as downstream along the jet centerline.

While the leading input mode represents the optimal way to force a jet to make noise, figures 5.5(b)-(d) show sub-optimal input modes ($n = 2, 3, 4$), which produce nearly the same amount noise as the optimal mode. They are active along upstream and downstream edges of the wavepacket associated with the optimal mode. As the mode number increases, the sub-optimal input modes progressively reach further upstream and downstream, as observed in previous chapters. To understand the pattern that they follow, it is helpful to to examine the sound fields they produce.

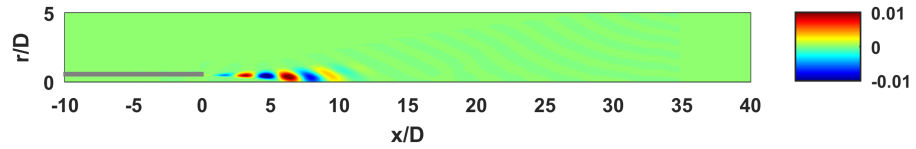

(a) $n = 1$

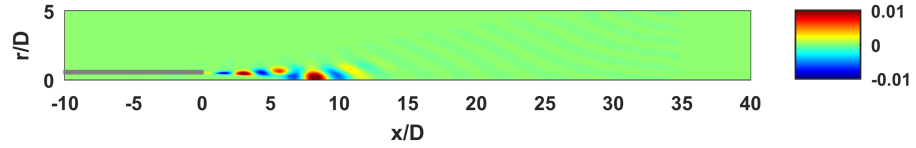

(b) $n = 2$

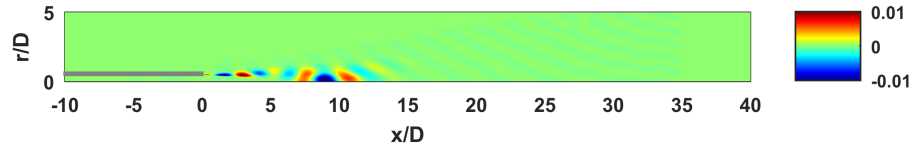

(c) $n = 3$

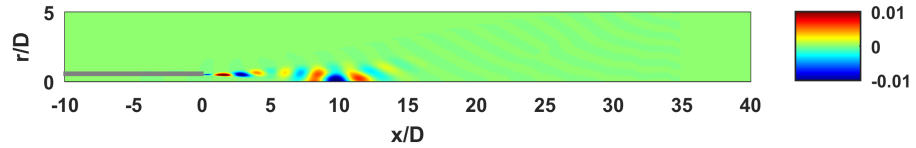

(d) $n = 4$

Figure 5.5: The first four input modes of the $M_j = 0.9$ isothermal jet for forcing frequency $St = 0.59$. Contours visualizes the real part of the normalized axial velocity forcing.

While the output domain is restricted to an arc at a distance of 100 jet diameters away from the nozzle exit, we can still obtain near-field sound associated with input modes by examining the system state after application of the resolvent operator, but before application of the output matrix C. We call these states "unrestricted" output modes. These modes extend over $-5 < x/D < 35$ in the axial direction and over $0 < r/D < 20$ in the radial direction, respectively. The output matrix C later projects them to an arc in the far-field. As shown in figure 5.6, unrestricted outputs resulting from these inputs follows a similar pattern. Black dashed lines in this figure represent the upstream, downstream, and lateral sponge layers. The pattern is now clear: the optimal mode radiates a beam of acoustic radiation directed toward the peak jet noise angle for this frequency. Each sub-optimal output mode is active along the edges of the preceding mode. This creates two beams of acoustic radiation in the first sub-optimal mode, three in the second, and so on.

5.4.2 Asymmetric pseudo-Gaussian envelope functions

Input modes correspond precisely to a decomposition of the acoustic source terms in an acoustic analogy. Our results indicate that these source terms can be understood in terms of wavepackets, which maintain correlation over significant distances. To characterize the physics of this wavepacket source, we consider the (complex) amplitude of the optimal input mode (as shown in figure 5.5(a)) along the nozzle lipline ($r/D = 0.5$). The blue solid line in figure 5.7 represents the absolute magnitude of the x-component of the input forcing for the optimal mode. Along this slice, we find a wavepacket that peaks around the end of the potential core (at $x/D = 6$). Although the effect is subtle, this wavepacket grows slightly faster along its upstream edge than it decays downstream. Such asymmetric wavepackets have been observed in experiments

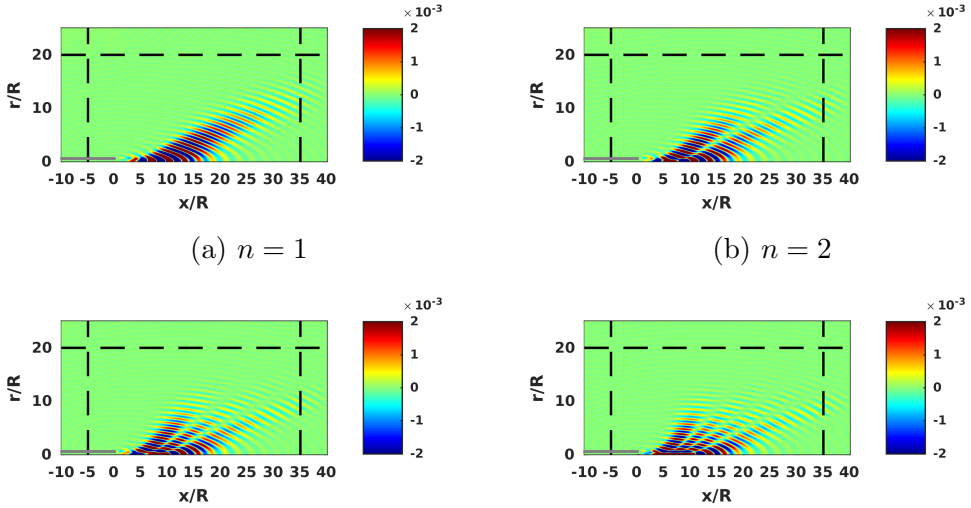

(a) $n = 1$ (b) $n = 2$

(c) $n = 3$ (d) $n = 4$

Figure 5.6: The first four unrestricted output modes of the Mach 0.9 subsonic jet at forcing frequency $St = 0.59$. Contours of the real part of normalized output pressure fluctuations are shown.

and simulations and have been modeled theoretically by a variety of different functions [56, 62, 63, 102, 103, 104]. One of the most popular functional forms is the following asymmetric pseudo-Gaussian:

$$u_x(x) = \begin{cases} exp\left[-\left(\frac{x-b_1}{c_1}\right)^{p_1}\right], & \text{if x} \leq b_1, \\ exp\left[-\left(\frac{x-b_1}{c_2}\right)^{p_2}\right], & \text{if x} \geq b_1, \end{cases} \tag{5.8}$$

where b_1 locates the peak of the wavepacket envelop, c_1 and c_2 respectively determine widths of the amplifying and decaying parts, and p_1 and p_2 represent the exponents, respectively. Applying a nonlinear least squares fitting algorithm, we find that $b_1 = 5.9375D, c_1 = 4.0599D, p_1 = 2.2545, c_2 = 4.5584D$, and $p_2 = 2.2517$ produce a pseudo-Gaussian curve that almost exactly matches our wavepacket. The fact that $p_1 > p_2$

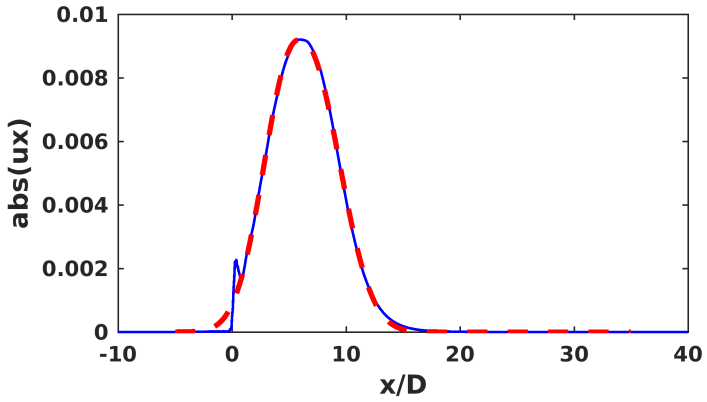

Figure 5.7: The lipline wavepacket measured at $r/D = 0.5$ (blue solid line) modeled by an asymmetric pseudo Gaussian wavepacket (red dashed line) for the optimal mode of the $M_j = 0.9$ subsonic jet at forcing frequency $St = 0.59$.

means that the wavepacket amplifies along its upstream edge slightly faster than it decays. This asymmetry is also indicated by $c_1 < c_2$. Also, because both p_1 and p_2 are approximately equal to two, the shape of our wavepacket is nearly (but not quite) Gaussian. The shape of the wavepacket, and in particular its asymmetry, are important factors determining its efficiency at generating acoustic radiation [104].

5.4.3 Similarity wavepackets

Optimal Mode

Although the lipline wavepacket associated with optimal input mode is well-described by a simple asymmetric function at one frequency, we repeat the modeling procedure over a range of frequencies. Motivated by the self-similarity of turbulent jets, we investigate whether similar asymmetric pseudo-Gaussian wavepacket functions can describe our input modes over different frequencies. Other wavepacket modeling approaches also have yielded self-similar asymmetric bell-shaped wavepackets over a range of frequencies [97, 105]. Naturally, the next task would be to construct a universal wavepacket

model, which can be widely used for a range of frequencies, using minimum degrees of parameters; such as the first moment (mean or centroid of a wavepacket in the axial direction) μ_1 and the standard deviation SD, which are respectively defined as:

$$\mu_1 = \frac{\int x u_x(x) dx}{\int u_x(x) dx} \tag{5.9}$$

and

$$SD = \sqrt{\frac{\int (x - \mu_1)^2 u_x(x) dx}{\int u_x(x) dx}}, \tag{5.10}$$

where E represents the expected value.

Figure 5.8 shows these quantities as a function of frequency. For sufficiently high frequencies, both the mean and standard deviation show a power-law dependence. As presented in figure 5.8(a) the mean location of the lipline wavepacket μ_1 shifts upstream as forcing frequency increases. Excluding few low frequency cases, μ_1 varies as $St^{-0.4858}$. Similarly, the standard deviation given in figure 5.8(b) follows the power-law form, though it decays slightly less rapidly than the mean as $St^{-0.4094}$. We observe such similarities for cases over $St > 0.5$, and this agrees the result of theoretical approach by Papamoschou [97] who reported the similarity wavepackets for turbulent jets for $St > 0.55$.

If we further take into account the virtual origin of a jet based on the momentum thickness, the decay of the mean and standard deviation becomes slightly more rapid. By considering an axial co-flow, the momentum thickness of a jet [58] is defined as:

$$\delta_\theta(x) = \int_0^\infty \bar{\rho}(x,r) \frac{\bar{u}(x,r) - u_{co}}{\bar{u}(x,0) - u_{co}} \left(1 - \frac{\bar{u}(x,r) - u_{co}}{\bar{u}(x,0) - u_{co}}\right) r dr, \tag{5.11}$$

and it is valid until the end of the potential core (x/D $\approx$ 5). Here, $\bar{\rho}$ and $\bar{u}$ represent

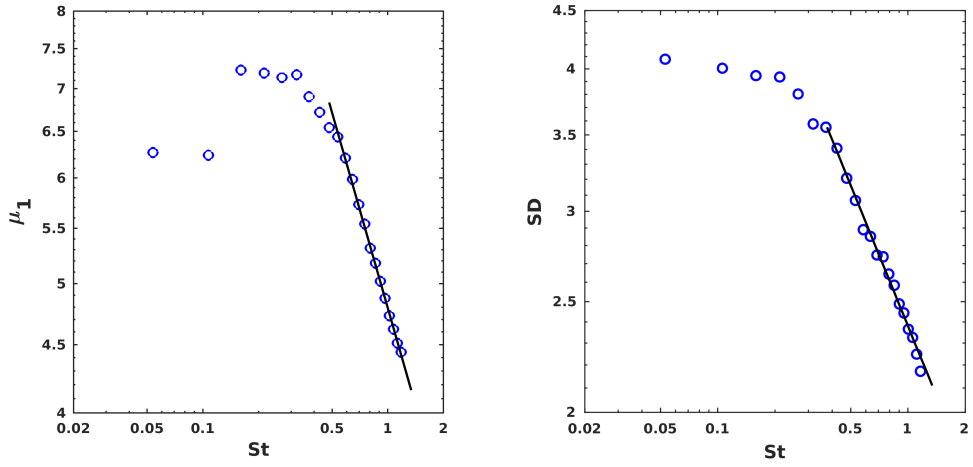

(a) (b)

Figure 5.8: Model parameters as a function of frequencies for the lipline wavepacket: (a) the mean decays and (b) the standard deviation.

the density and the axial velocity of a base flow, and u_{co} means a uniform axial co-flow. Using this definition, the momentum thickness of the subsonic jet is shown in figure 5.9 for $0 \leq x/D \leq 5$, yielding a positive virtual origin $x_0 = 0.5213D$. The mean of the lipline wavepacket with respect to the virtual origin is then measured as shown in figure 5.10, decaying as $St^{-0.5380}$. Even after considering the virtual origin, the variation of the standard deviation in frequency remain almost the same as before.

Furthermore, we compute the skewness of wavepackets for each frequency defined by:

$$SK = E\left[\frac{(x-\mu_1)^3}{SD^3}\right] \tag{5.12}$$

where E means the expected value, SD denotes the standard deviation, and μ_1 represents the centroid of a wavepacket in the axial direction, respectively. Using this, figure 5.11 indicates positively skewed wavepackets for almost all frequencies as expected from long decaying tails. For frequencies $St > 0.5$ wavepackets becomes more skewed

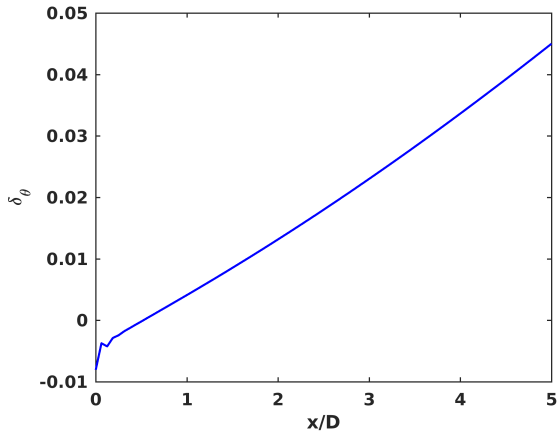

Figure 5.9: Momentum thickness of the $M_j = 0.9$ subsonic jet. Intercept of the momentum thickness profile with the abscissa computes the virtual origin $x_0 = 0.5213D$.

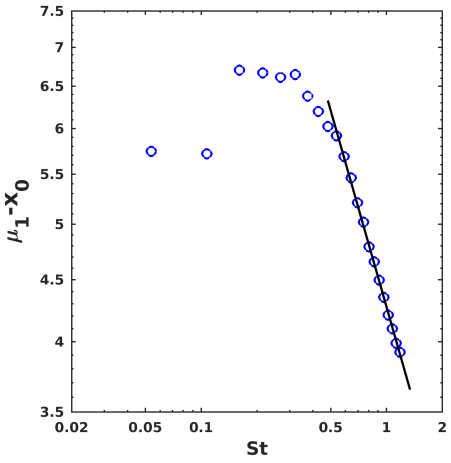

Figure 5.10: The mean of the lipline wavepacket as a function of frequency, measured from the virtual origin based on the momentum thickness.

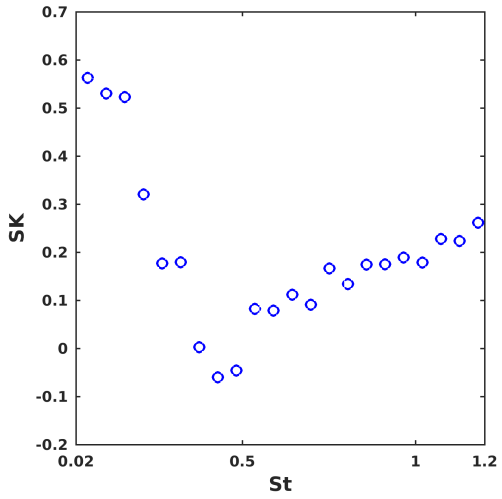

Figure 5.11: Skewness of the lipline wavepacket as a function of forcing frequency.

as frequency increases, but overall, the variations of skewness remain small, suggesting similarity wavepackets in frequency.

Finally, we construct wavepacket models, which are functions of a new variable η transformed by the mean source location μ_1 and scaled by the standard deviation SD such as:

$$\eta = \frac{x - \mu_1}{SD}. \tag{5.13}$$

Here, instead of using two parameters c_1 and c_2 that control the widths of two parts of wavepackets separately, the standard deviation is chosen as a single unified parameter to describe the shape of wavepacket envelopes. Figure 5.12 shows the overall collapse of wavepacket envelopes taken over a range of frequencies between $St = 0.5$ and $St = 1.2$.

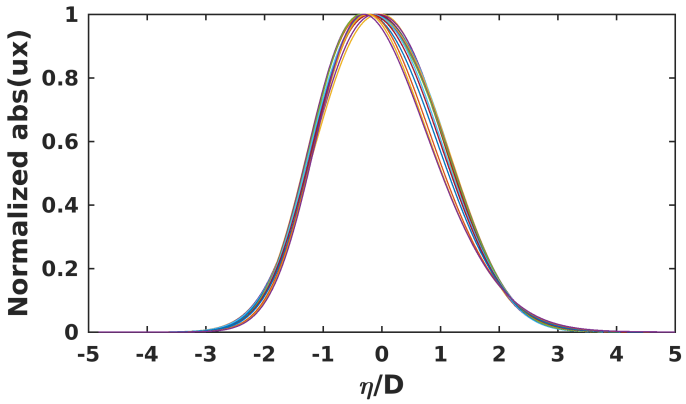

Figure 5.12: Collapse of scaled lipline wavepackets obtained for frequencies $0.5 < St < 1.2$, suggesting simple similarity wavepacket models based on the similarity variable η.

Sub-optimal modes

Sub-optimal modes appear to be composed of multiple wavepackets (see figure 5.5). The envelopes of these component wavepackets are similar in shape to that associated with the optimal mode. Because each sub-optimal mode contains multiple wavepackets, modeling them is more complicated. Moreover, as the frequency changes, a group of wavepackets moves upstream and sometimes merges into the wavepacket in a boundary layer developed along the nozzle wall. It thus requires a great care to track the same type of wavepackets and model them as similarity wavepackets in frequency.

In figure 5.13 we model wavepackets taken along the jet lipline ($r/D = 0.5$) for the first sub-optimal mode ($n = 2$) by asymmetric pseudo-Gaussian functions. In contrast to the optimal mode, the first sub-optimal mode captures two wavepackets downstream of the nozzle exit ($x/D = 0$). They, however, bear a similar shape to that captured by the optimal mode, and are approximated using the same type of asymmetric pseudo-Gaussian function given in equation (5.8). Here, the blue solid line represents the input-mode-captured wavepacket, while the red dashed line and the green dashed line

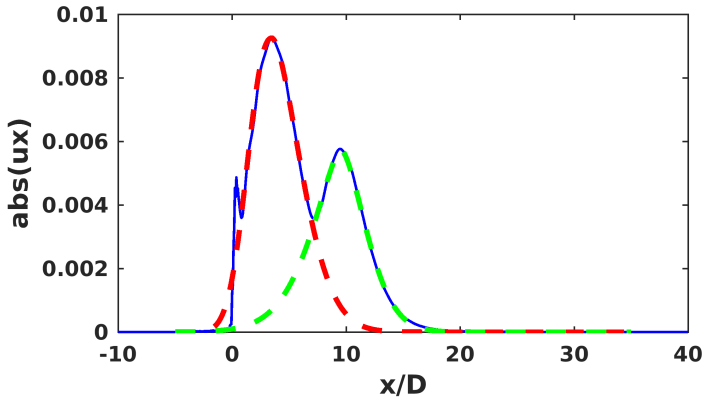

Figure 5.13: Wavepackets taken along the lipline for the first sub-optimal mode ($n = 2$) at $St = 0.59$ modeled using asymmetric pseudo-Gaussian functions.

denote modeled wavepackets.

Figure 5.14 shows wavepackets taken along the inner lipline for mode number $n = 3$ (the next sub-optimal mode). We observe three wavepackets, denoted by $W1$, $W2$, and $W3$, measured from the upstream. Each wavepacket is positively skewed and bell-shaped as in other cases. We therefore expect that a similarity wavepacket model could be constructed, even for this case.

The pattern shown in figures 5.12 through 5.14 is approximately the same that obtained by taking a sequence (of magnitudes) of axial derivatives of the optimal wavepacket envelope. Of course, the input modes are two-dimensional, so their inter-relationship may be more complicated than this. Still, the sub-optimal modes appear to be associated with dynamics in the regions where the amplitude of the preceding mode in the sequence is undergoing the most change (i.e., where its gradient is greatest). In the next section, we discuss physical mechanisms that could lead to sources that can align with such a pattern, thereby creating noise.

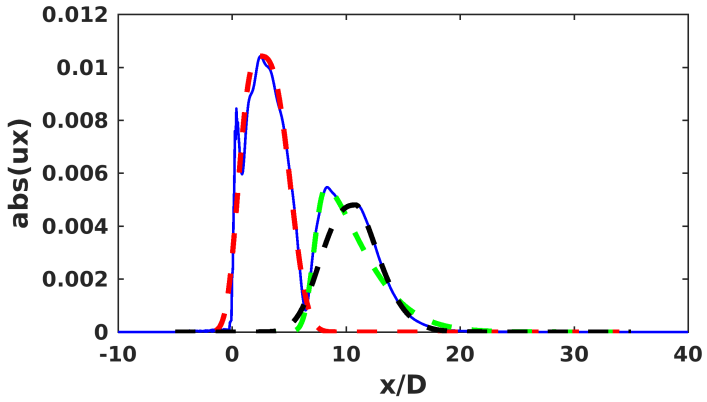

Figure 5.14: Wavepackets taken along the lipline for the second sub-optimal mode (blue solid line) at $St = 0.59$ modeled using asymmetric pseudo-Gaussian functions. W1: red dashed line, W2: green dashed line, and W3: black dashed line, counted from the upstream.

5.4.4 Physical origin of sub-optimal input modes

In previous sections, we found that the optimal input mode clearly reveals a wavepacket whose envelope corresponds to an asymmetric pseudo-Gaussian function. Moreover, we observed that the sub-optimal input mode captures structures that follow upstream and downstream edges of the optimal wavepacket. As shown in figures 5.13 and 5.14, the sub-optimal mode shows increasingly many humps as the mode number increases. The humps in each sub-optimal mode appear at locations where the largest differences would occur, if the wavepackets in the preceding mode were perturbed slightly in their axial position. This type of uncertainty in a wavepacket's axial position is known as "jitter" [4, 51, 52]. Jitter arises from the fact that high-speed jets are susceptible to variations at very low frequency, much lower than the frequencies associated with wavepackets. On the timescales of the wavepacket, this very low frequency variation appears to correspond to changes in the base flow. The wavepacket responds to slow variations in the base flow by changing its position (and perhaps, shape). While axial

jitter of the optimal wavepacket leads to a double-humped shape corresponding to the first sub-optimal mode, axial jitter of the first sub-optimal mode produces a shape with four humps. As shown in figure 5.14, the second sub-optimal mode has three humps.

Alternatively, we consider axial decoherence [56, 106] as another possible mechanism by which acoustic sources embedded in the jet turbulence may align with the pattern of sub-optimal modes that we find. Entire wavepackets are almost never visible in instantaneous snapshots of the near-field turbulent jets. Instead, one observes "pieces" of wavepackets that persist over a maybe only a few diameters before losing coherence. Inside these windows of coherence, fluctuations grow or decay in accordance to the overall wavepacket envelope. While the growth and decay of disturbances are governed by dynamics, wavepackets have a statistical nature as turbulence drives instability waves into and out of coherence. An entire wavepacket, therefore, should be thought of as the tendency of the base flow to make disturbances grow or decay in accordance with instability physics. Because these physics do not change in time for a given base flow, a wavepacket is also constant and is determined by dynamics.

To model decoherence, we perturb the optimal wavepacket by small random forcing, and extract short, stochastic windows of it, positioned between $-5 \leq x/D \leq 15$. The constant window width w is chosen to be as large as the coherence length-scales of the axial velocities such that $w = 2D$. Outside of a given window, we zero all other fluctuations. We repeat this process to build a stack of different realizations, visiting a different part of the wavepacket each time and reproducing the effect of its axial decoherence. Singular value decomposition applied to this collection yields its dominant dynamical features. As expected, the first singular vector recovers the original wavepacket (not shown). The right-hand column of figure 5.15 shows the second and third singular vectors obtained from the decomposition. While there are differences, they reproduce the corresponding sub-optimal modes fairly well. In particular, the third singular vector

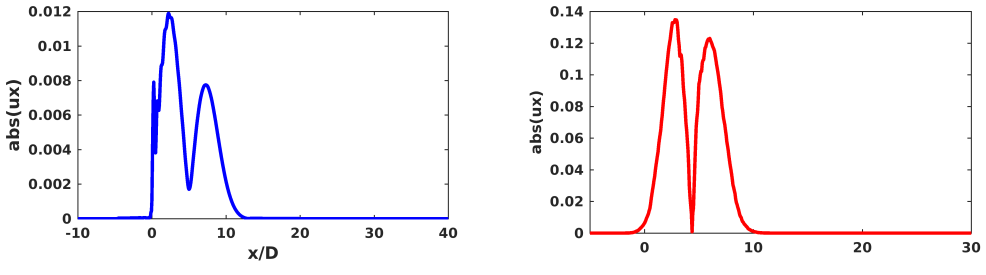

(a) $n = 2$ (b) $n = 2$

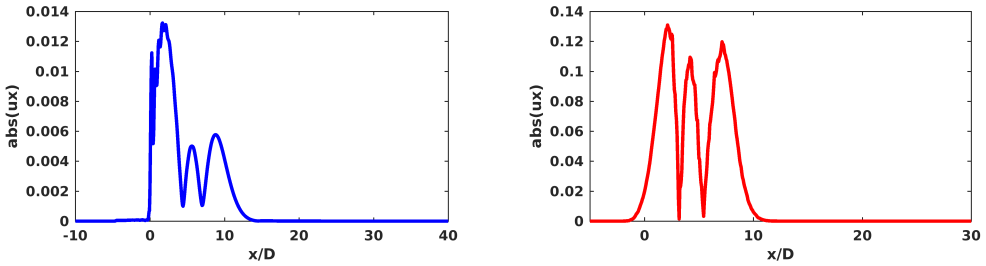

(c) $n = 3$ (d) $n = 3$

Figure 5.15: By taking singular value decomposition of the matrix whose columns consists of a series of axial snapshots of the optimal wavepacket, the left singular vectors (b,d) qualitatively reproduce the actual input modes (a,c) for $St = 1.18$.

contains three humps just like the second sub-optimal mode. This therefore conclude that axial decoherence is a physical mechanism by which acoustic sources in the jet align well with input modes predicted by input-output analysis.

We should note that unlike the connection between input and output modes, there is not necessarily a causal relationship between axial decoherence modes and input modes. If it occurs, jitter may also project a significant portion of the sources onto the input modes. From our analysis, it seems that axial decoherence aligns even better with the input modes, and thus is an efficient mechanism of noise production.

5.5 Input-output analysis of jet noise radiating to specific angles

Previously, we have described how the optimal and sub-optimal modes cooperate to complete the overall acoustic field spanning a wide range of polar angles. Strong directional radiation at relatively low angles is mostly formed by the optimal mode. Sideline noise, on the other hand, is associated with sub-optimal modes, which form a sequence where each mode follows the edges of its predecessor. Physically, sub-optimal modes can be interpreted as the results of jitter and/or decoherence of the optimal wavepacket as discussed in the previous section. Therefore, sub-optimal modes, and by extension sideline noise, may be seen as consequences of large-scale acoustic sources. This provides an alternative view to the two-source theory of jet noise [91, 93, 107], although it agrees well with stochastic similarity wavepacket models of jet noise [97, 105].

To further test the hypothesis that sideline noise is connected to large-scale flow features, we consider input modes that radiate optimally to a single angle. An advantage of our analysis is that the operators B and C can be adjusted to investigate different physical questions. In this section we modify the output operator C to measure far-field sound at only a single observer angle. At the peak jet noise direction for a specific frequency, we expect to recover (and do recover) the same optimal input mode as in the previous sections, where noise radiation to all angles was considered. At the same frequency, however, we investigate whether the sub-optimal modes remain the optimal way to produce sound at angles not corresponding to the peak.

If the operator C is restricted to a single observer angle, then the operator $\tilde{H}^{\dagger}\tilde{H}$ is of rank 1 so that only one singular value of $\tilde{H}$ may be computed. To obtain additional information, instead of an observer located at a single point, we consider acoustic radiation to a small arc spanning 1°, centered around the angle of interest. We have found

that resolving this small arc with five observer locations is sufficient (finer resolution does not change the following results significantly).

In figure 5.16(a) and (b), we consider axisymmetric disturbances only since they alone recover nearly all of the total sound for small radiation angles. Figure 5.16(a) shows the optimal input mode for $\phi = 40°$, which corresponds to the peak noise direction at this frequency, and this mode resembles the optimal input mode for radiation to the full arc, which is given in figure 5.5(a). Additionally, the input mode for observer angle $\phi = 20°$ as shown in figure 5.16(b) recovers the first sub-optimal input modes given in figure 5.5(b). Furthermore, by following a theoretical directivity obtained by Papamoschou [97], which predicts that noise emission at 60° and 90° for $St \approx 0.5$ strongly depends on higher azimuthal modes—for example, $m = 4$ and higher—, we decide to consider small disturbances with $m = 4$ for observers at these two angles in Figure 5.16(c) and (d). In each sub-figure visualizes the real part of the normalized axial velocity forcing.

In this figure, while input mode for higher angles do not correspond to sub-optimal modes, they still are wavepackets. A rank-1 approximation does not necessarily have to form wavepackets; incoherent fine-scale structures may optimally produce noise at a single location close to the sideline, although a superposition of large-scale coherent structures obtained in a set of input modes generate sound in far more extended region. Nevertheless, this figure confirms the existence of well-organized structures that create far-field sound in the sideline direction, underpinning a unified noise generation mechanism in a form of wavepackets regardless of radiation angles. While each optimal input mode obtained from a rank-1 approximation radiate sound, exclusively at a specified angle, we may apply the FW-H projection method to unrestricted output modes. Using a cylindrical projection surface at $r/D = 6$, figure 5.17 shows that the optimal input wavepackets resulted from a rank-1 approximation propagate sound wave

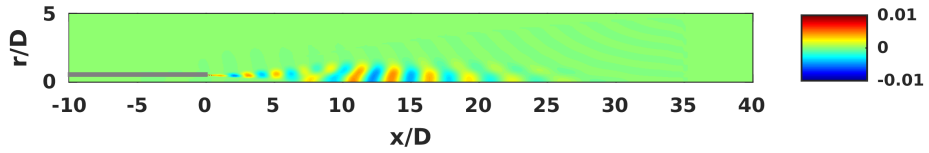

(a) $\phi = 20°$ and $m = 0$

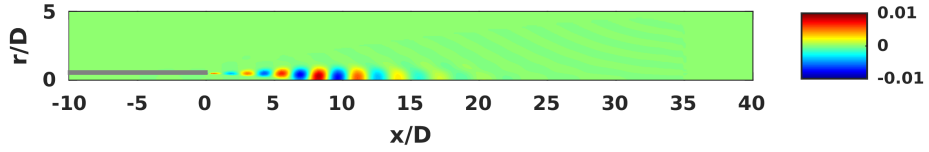

(b) $\phi = 40°$ and $m = 0$

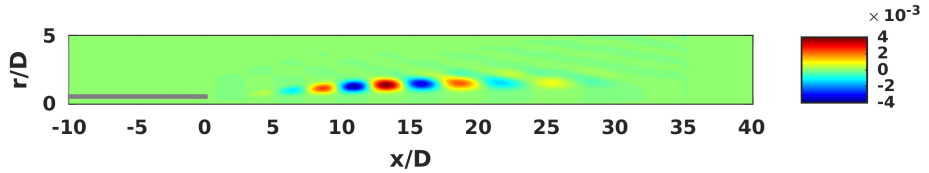

(c) $\phi = 60°$ and $m = 4$

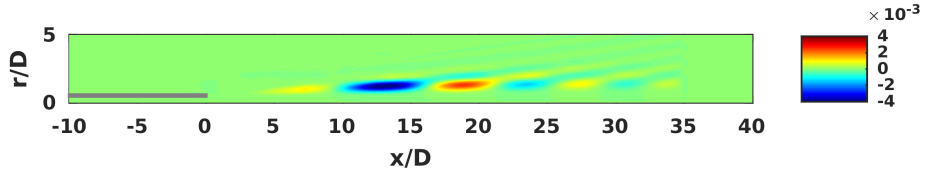

(d) $\phi = 90°$ and $m = 4$

Figure 5.16: Rank-1 approximations of input modes for single observers at various angles at forcing frequency $St = 0.59$.

in the designated direction. Accordingly, we view these input wavepackets as a sort of generalization or union of the optimal and sub-optimal input wavepackets, educed to radiate sound in a desired angle.

Another way to validate forcings captured by rank-1 approximations and associated acoustic response may be modeling a directivity pattern using 141 single probes and testing whether the resulting directivity recovers that predicted by a full arc spanning $\phi = 10^\circ$ to 150° as an output domain. Here, sound radiated to the full arc from axisymmetric disturbances at forcing frequency $St = 0.59$ is obtained by superposing 29 output modes under the assumption of white noise forcing, which means that each mode is excited equally with unit energy. As shown in figure 5.18 we find that the acoustic field predicted by rank-1 approximations (red dotted line) agrees well with the field obtained for the full-arc output domain (blue solid line) at low polar angles. The two curves, however, deviate from each other at angles larger than $\phi = 70^\circ$. Nevertheless, it should be noted that the directivity for the full-arc is yielded by assuming uniform forcings. Figure 5.16 shows that the wavenumber of input wavepackets decreases while the radiation angle increases so that a given wavepacket envelope appears more compact at a given forcing frequency. This enhances radiative efficiency of wavepackets and also the rotates radiation angle into the sideline direction [104, 108]. In sum, rank-1 approximation of input wavepackets for a single observer may be educed from the optimal and sub-optimal wavepackets captured by a full-arc output domain, having physical meanings. Based on the fact that it recovers large-scale coherent structures for a observer in any direction, one coherent source mechanism may be justified for turbulent jet noise again.

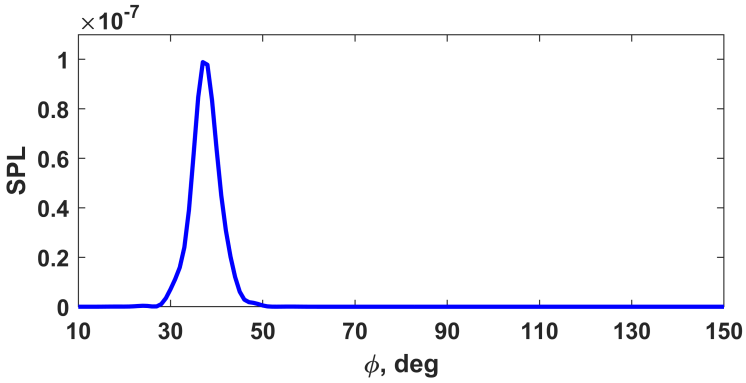

(a) $\phi = 40°$ and $m = 0$

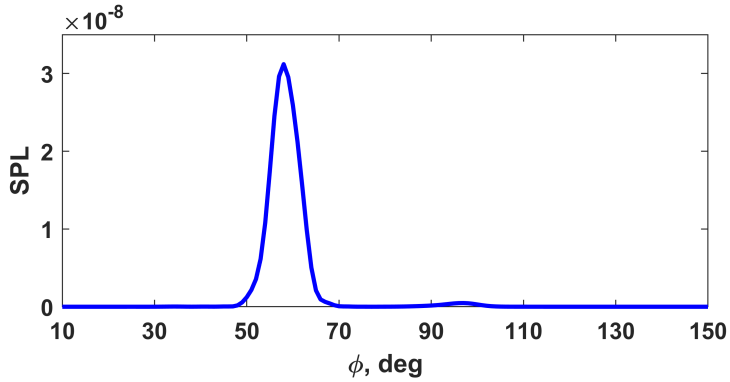

(b) $\phi = 60°$ and $m = 4$

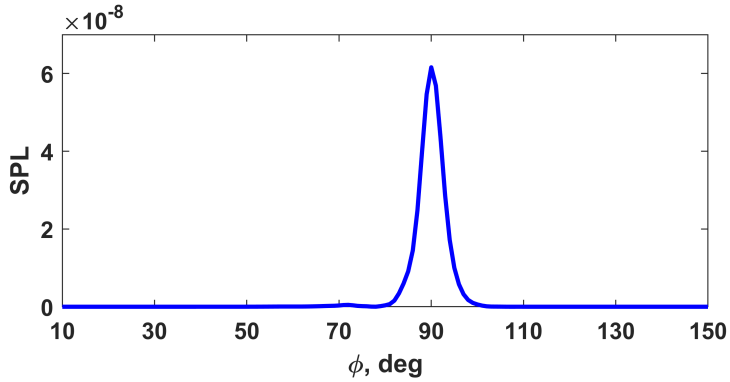

(c) $\phi = 90°$ and $m = 4$

Figure 5.17: Acoustic far-field at 100 diameters away from the nozzle exit for forcing frequency $St = 0.59$, predicted by applying the FW-H projection method to acoustic response obtained from a rank-1 approximation.

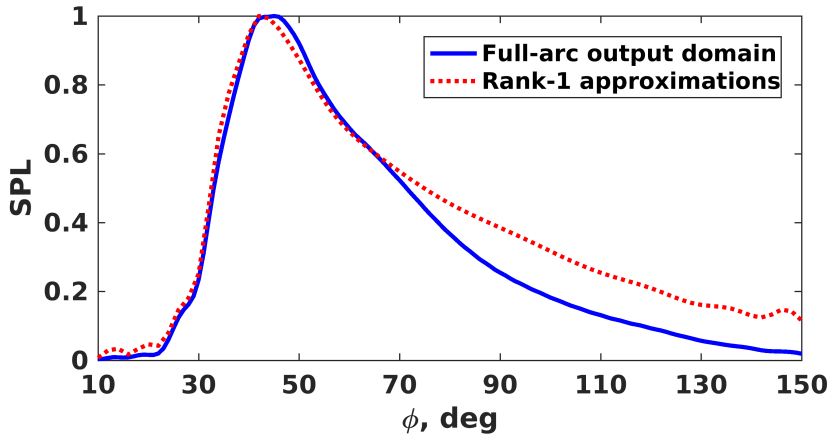

Figure 5.18: Comparison of the directivity patterns for axisymmetric disturbances at $St = 0.59$.

Far-field spectra

Figure 5.19 shows contours of far-field SPL over radiation angles from $\phi = 20°$ to $120°$ and frequencies for $0.05 < St < 1$. At each frequency we superpose the optimal and several sub-optimal acoustic responses until we meet the dropoff of the corresponding singular values. In this way figure 5.19 visualize contour maps of far-field spectra on the Strouhal number-radiation angle plane. We consider axisymmetric ($m = 0$), helical ($m = 1$), and double-helical ($m = 2$) azimuthal modes in figures 5.19(a), (b), and (c), respectively, to reconstruct the SPL level at a given frequency and a radiation angle. For $m = 0$, the far-field spectrum has a peak at $\phi = 40°$ and $St = 0.32$. At higher angle the spectrum does not broaden with respect to frequency. As the azimuthal wavenumber modes increases, however, the spectrum shifts to higher frequencies as shown in figures 5.19(b) and (c). Adding the spectra from $m = 0$, 1, and 2 results in figure 5.19(d). The spectra are significantly broader than figure 5.19(a). In other words, at high frequencies and radiation angles where higher azimuthal modes required to capture full far-field acoustics, our analysis would recover broadened spectra, compared

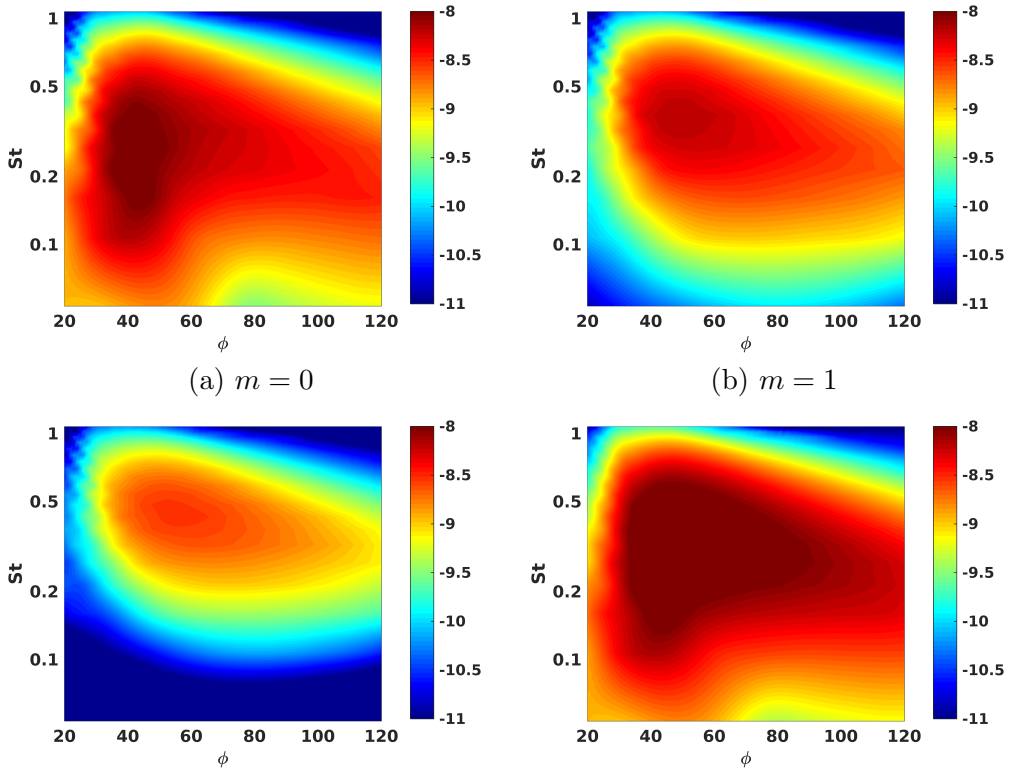

(a) $m = 0$ (b) $m = 1$

(c) $m = 2$ (d) $m = 0$, 1, and 2

Figure 5.19: Far-field acoustic spectra for the $M_j = 0.9$ subsonic jet on the Strouhal number-radiation angle plane.

to the spectra at low radiation angles where the axisymmetric mode is significant.

This may be viewed more clearly by examining far-field pressure of a single observer at $\phi = 90°$, which represents the sideline noise direction, over a range of frequencies. As shown in figure 5.20 the axisymmetric mode generates the loudest sound for low frequencies $St < 0.4$. Higher azimuthal modes predict much weaker sound at these frequencies. As we further increase forcing frequencies, however, these modes dominate the acoustic response over the axisymmetric mode, yielding more flattened spectra. Finally, figure 5.21 compares spectra at $\phi = 40°$ to those at 90° by considering the first 5 azimuthal modes at high radiation angle. For low frequencies, we predict acoustic

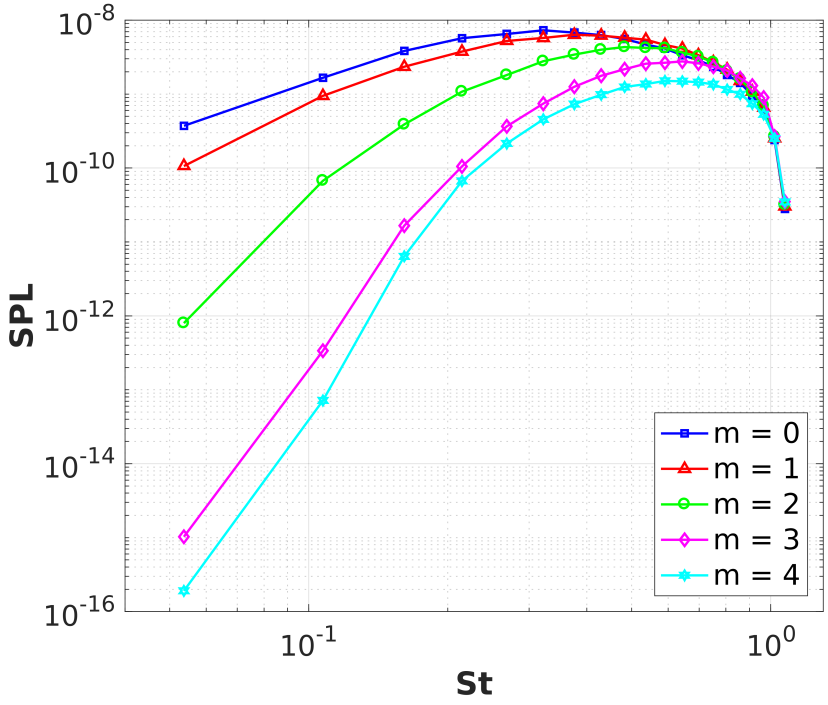

Figure 5.20: Far-field acoustic spectra of the Mach 0.9 subsonic jet for a single observer at $\phi = 90°$. We examine acoustic responses of various azimuthal modes from $m = 0$ to 4.

spectra as steep as large-scale similarity spectrum (denoted by F spectrum) even at the high radiation angle; nevertheless, as frequency increases, they become broaden as the radiation angle increases.

To further understand the wavepackets producing sound at high angles, we consider sub-optimal forcings from the small arc calculation. We distribute five observers along a small arc whose extent is given by 1°, centered at either 40° or 90° to represent the low and high radiation angles. In other words, we take rank-5 approximations of acoustic response of the Mach 0.9 subsonic jet. While we consider axisymmetric disturbances for the low angle, higher azimuthal mode ($m = 4$) is examined for the high

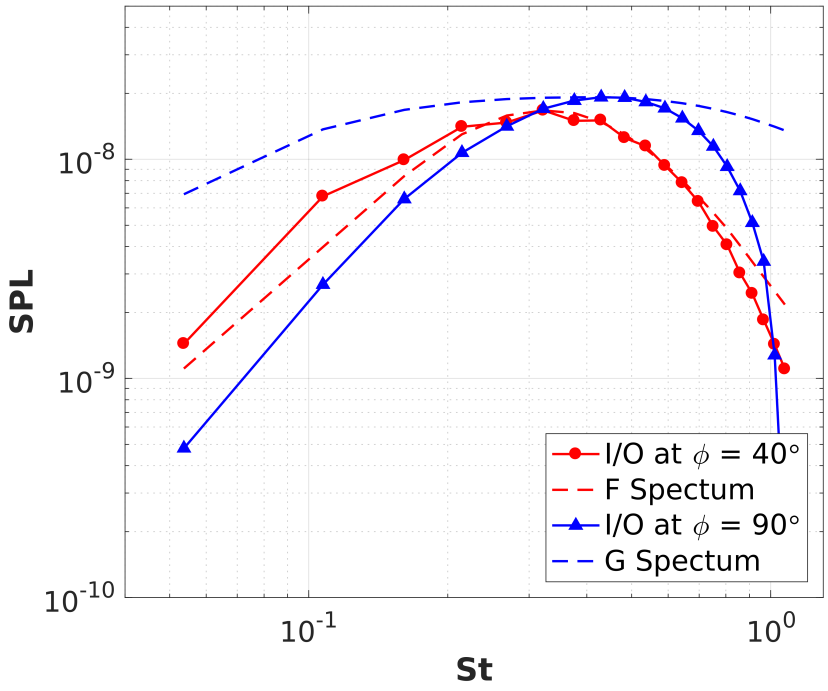

Figure 5.21: Far-field acoustic spectra of the Mach 0.9 subsonic jet for single observers at $\phi = 40°$ and $90°$, indicating broadening as the radiation angle increases for high frequencies.

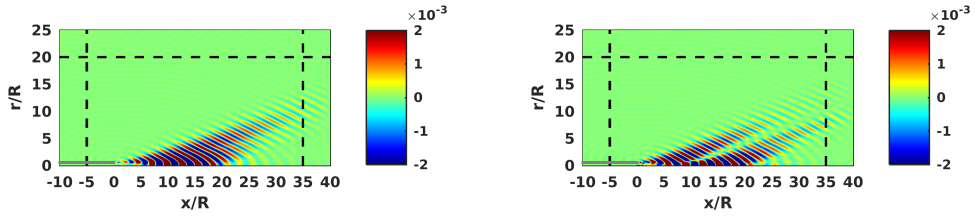

(a) $n = 1$ (b) $n = 2$

Figure 5.22: The first two unrestricted output modes of the Mach 0.9 subsonic jet at forcing frequency $St = 0.59$ for a small arc centered at $\phi = 40°$. Contours of the real part of normalized output pressure fluctuations for $m = 0$ are shown.

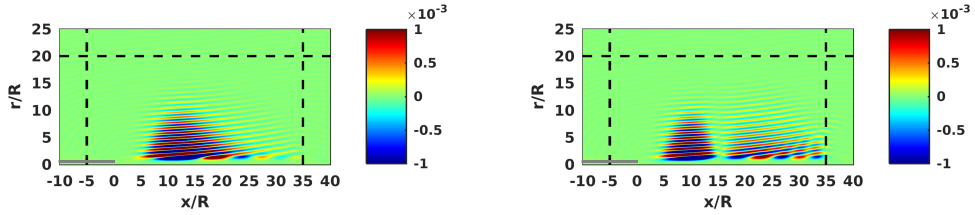

(a) $n = 1$ (b) $n = 2$

Figure 5.23: The first two unrestricted output modes of the Mach 0.9 subsonic jet at forcing frequency $St = 0.59$ for a small arc centered at $\phi = 90°$. Contours of the real part of normalized output pressure fluctuations $m = 4$ are shown.

angle. At $\phi = 90°$ the ratio of the optimal to sub-optimal gains σ_1/σ_2 is computed as 8.366, while it is 13.67 in the low radiation angle case. The ratios of the optimal to higher-rank sub-optimal gains also follow this trend. Moreover, figures 5.22 and 5.23 are unrestricted output modes for respectively $\phi = 40°$ and $90°$, showing that sub-optimal output modes follow the edges of acoustic beams obtained in the optimal mode. In the sideline direction, more degrees of freedom are needed as azimuthal mode number and frequency increases, leading to broadening of acoustic spectra [109].

Chapter 6

Parametric studies

In this chapter we discuss dependence of input-output analysis on parameters such as the Mach number, applied heating, eddy viscosity, and azimuthal wavenumbers. Part of the materials presented in this chapter is based on the publications [68, 110].

6.1 Effects of Mach numbers

In addition to the $M_j = 0.9$ and $M_j = 1.5$ jets discussed so far, we computed 11 other RANS base flows corresponding to high-speed isothermal jets. The entire database covers jet Mach numbers ranging from $M_j = 0.6$ to 1.8 in increments of 0.1. Figure 6.1 compares centerline axial velocity for these base flows. Note that the potential core length increases slightly with increasing jet Mach number.

In this section the dynamics of small perturbations are governed by the LEE. Figure 6.2 shows resulting singular values for several subsonic and supersonic jets at the same jet Strouhal number $St = 0.33$. The singular values suddenly drop after a certain mode number, and this sudden decrease is delayed with increasing jet Mach number. For example, the singular values drop after $n \approx 15$ for the $M_j = 0.9$ subsonic jet and

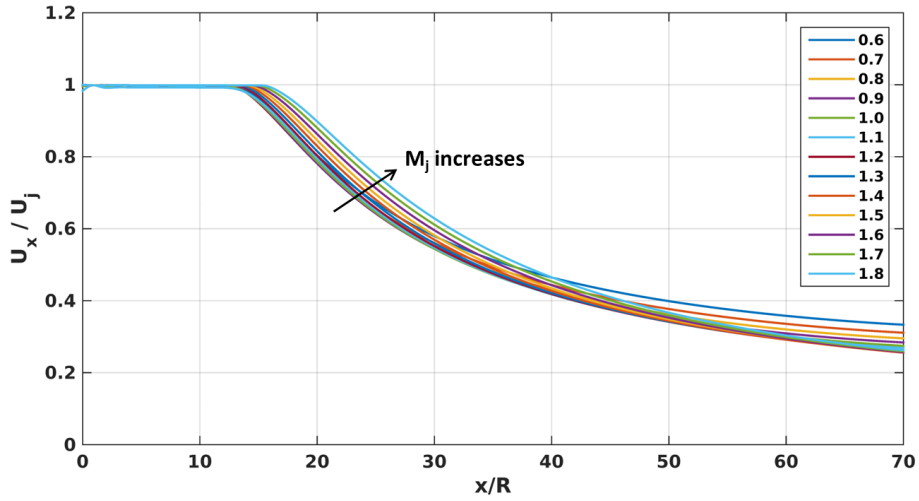

Figure 6.1: Streamwise distribution of axial velocity on the jet centerline.

$n \approx 30$ for the $M_j = 1.5$ supersonic jet, respectively.

We find, however, that many of the sub-optimal singular values collapse to a single curve if we fix the acoustic Strouhal number St_a instead of the jet Strouhal number St. The acoustic Strouhal number controls the wavelength of acoustic waves outside of the jet. Figure 6.3 shows singular values for a number of different jet Mach numbers for fixed acoustic Strouhal number $St_a = 0.50$. This result implies that the acoustic Strouhal number may be used as a new scale to anticipate the sudden drop of gains in the input-output behavior of jet noise.

While many of the singular values collapse for fixed St_a, the optimal mode and first few sub-optimal modes remain sensitive to jet Mach number. Here, we again observe that the first singular value dominates the response of supersonic jets, whereas sub-optimal modes play a more significant role for subsonic jets. Using equation (3.1), figure 6.4 shows the increase in SPL owing to sub-optimal modes as a function of jet Mach number. We interpret the drop in ΔSPL at $M_j \approx 1.3$ to be a consequence of the onset of Mach wave radiation. Assuming that the optimal mode corresponds to an

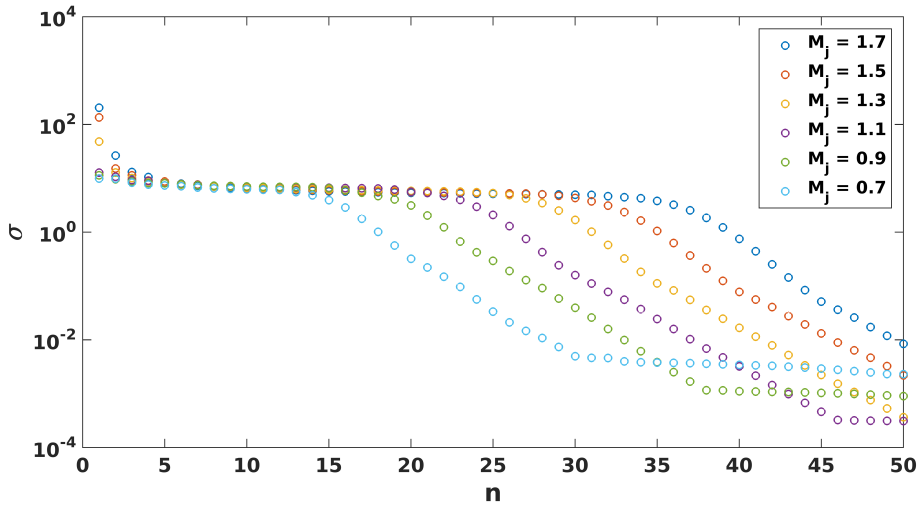

Figure 6.2: Optimal gain vs. mode number for different jet Mach numbers keeping the jet Strouhal number fixed $St = 0.33$.

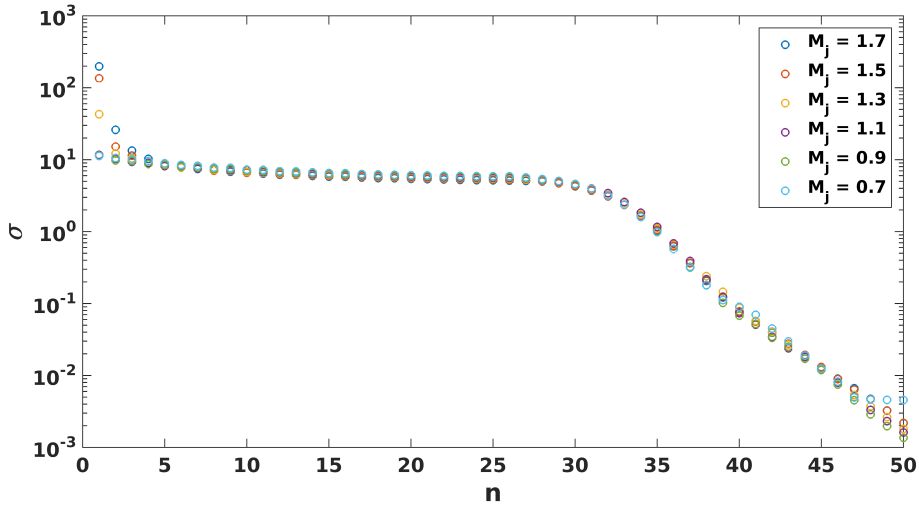

Figure 6.3: Optimal gain vs. mode number for different jet Mach numbers keeping the acoustic Strouhal number fixed $St_a = 0.50$.

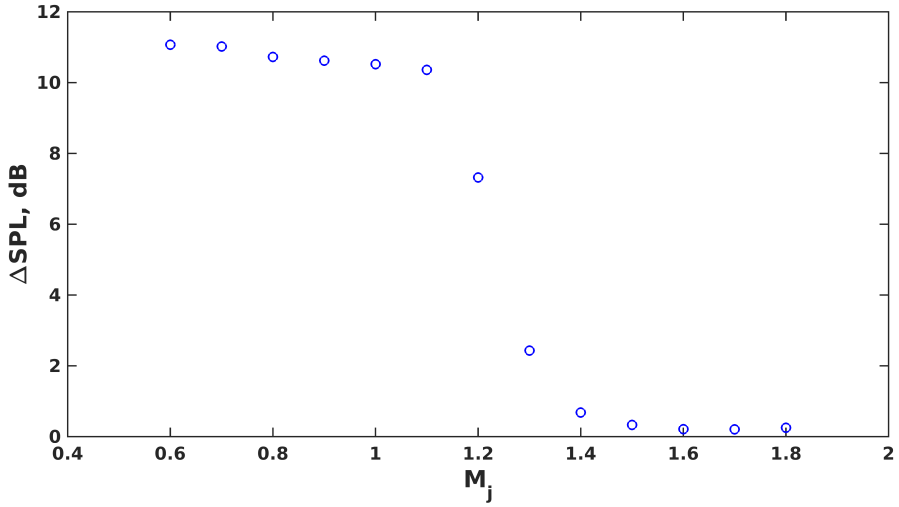

Figure 6.4: Noise increase including sub-optimal modes with respect to the jet Mach number.

instability wavepacket with convection velocity u_c between $0.65u_j < u_c < 0.8u_j$ [91, 107], then we can expect the onset of Mach wave radiation to occur between $1.3 < M_a < 1.6$. Mach wave radiation occurs when disturbances propagate along the jet supersonically with respect to the ambient speed of sound, coupling near-field pressure disturbances to far-field acoustic radiation in a linear fashion [91].

6.2 Effects of heating

6.2.1 Base flows

To study effects of applied heating on small perturbations in high-speed turbulent jets, which are governed by the LEE, we produce RANS solutions over a range of jet Mach numbers with different amounts of applied heating. As the core of the jet heats above ambient, the speed of sound c_j inside the jet increases, which means that the jet Mach number decreases for constant jet velocity u_j. In this case, it is useful to use Mach

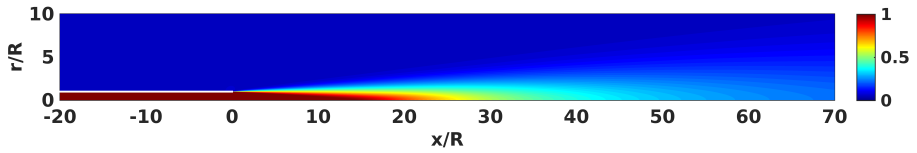

Figure 6.5: Contours of axial velocity from a RANS solution of a round $M_j = 1.5$ supersonic heated jet with $T_j/T_\infty = 1.44$. The velocity contours are normalized by the velocity at the nozzle exit at $x/R = 0$.

number based on the constant speed of sound c_∞ in the ambient fluid, acoustic Mach number St_a. In this section, we vary both the jet and acoustic Mach numbers such that $0.6 < M_j < 1.5$ and $0.6 < M_a < 2.0$. In each case, we consider only heated jets such that $M_j < M_a$, that is, $T_j > T_\infty$. Except for this, other properties and flow configurations are remained the same as described in chapter 3. Figure 6.5 shows contours of axial velocity from a RANS solution of a $M_j = 1.5$ heated jet with the jet-to-ambient temperature ratio $T_j/T_\infty = 1.44$.

6.2.2 Optimal and sub-optiml modes

Figure 6.6 shows the first 50 singular values for the $M_j = 1.5$ jet with $T_j/T_\infty = 1.44$, or equivalently $M_a = 1.8$, for the forcing frequency $St = 0.28$. The optimal gain for this heated jet is found to be $\sigma_1 = 3.26 \times 10^2$, which is larger than that for the isothermal jet with the same jet Mach number.

Figure 6.7 and figure 6.8 respectively visualize the first four output and input modes for the heated jet. The output modes, which are restricted to be pressure perturbations in the region far away from the jet, follow the same pattern as obtained for isothermal jets in section 3.2.1 in terms of the increasing number of beams and progressively rotating radiation angles with respect to the mode number. The optimal mode shows a single strong acoustic beam radiating at an angle of 32° in the direction of peak jet noise

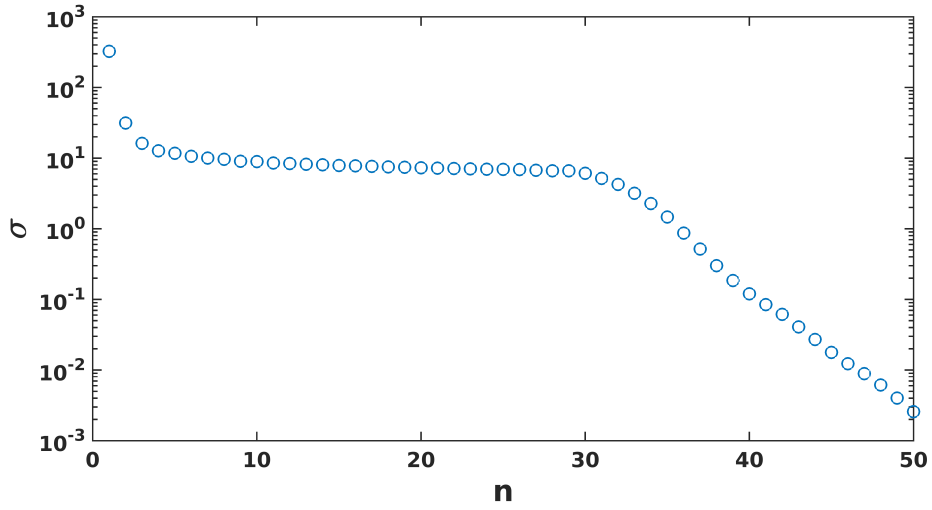

Figure 6.6: Singular values vs. mode number for the $M_j = 1.5$ jet with $T_j/T_\infty = 1.44$ at forcing frequency $St = 0.28$.

measured from the downstream jet axis, which is slightly larger than the isothermal case. As the mode number increases, additional beams appear at both larger and smaller radiation angles.

The input modes are restricted to the region near to the jet turbulence, as represented by the rectangle in figure 6.8. The choice of the input domain is also consistent with the study of input-output analysis for isothermal jets in chapter 3. Compared to that obtained for the isothermal jet, the optimal input mode in this case is more highly concentrated upstream of the nozzle exit. Similar to the isothermal sub-optimal input modes, sub-optimal inputs for this heated jet extend downstream farther than the optimal mode. It is found that the sub-optimal inputs for the heated jet, however, align better with the shear layer in comparison with those obtained for the isothermal case.

We repeat input-output analysis for a $M_j = 0.9$ subsonic heated jet with $T_j/T_\infty = 1.78$, or equivalently $M_a = 1.2$, for the forcing frequency $St = 0.42$. This jet Strouhal number yields the same acoustic Strouhal number $St_a = StM_a = 0.50$ as in the case

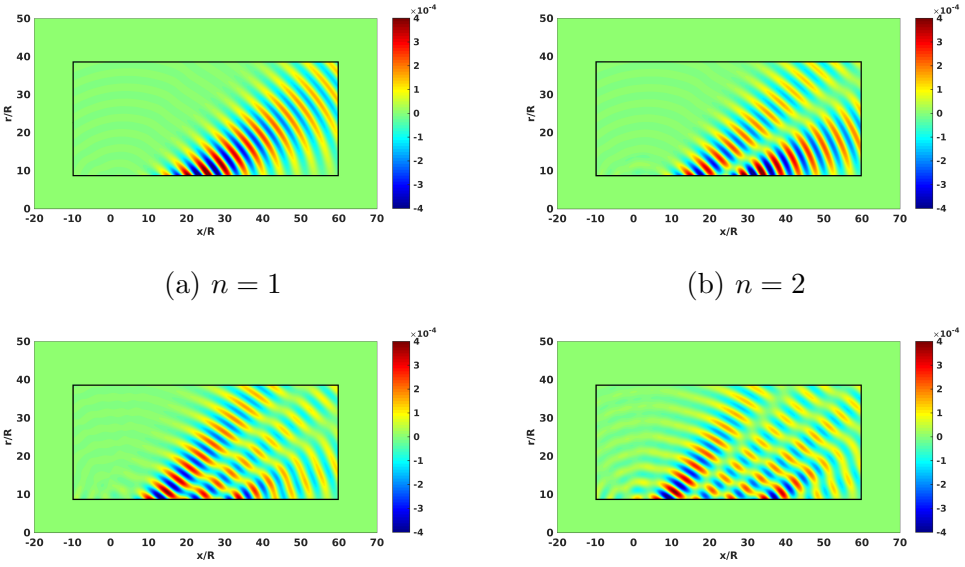

(a) $n = 1$ (b) $n = 2$

(c) $n = 3$ (d) $n = 4$

Figure 6.7: The first four input modes of the $M_j = 1.5$ supersonic heated jet with $T_j/T_\infty = 1.44$. Contours visualize the real part of the normalized output pressure perturbations for forcing frequency $St = 0.28$.

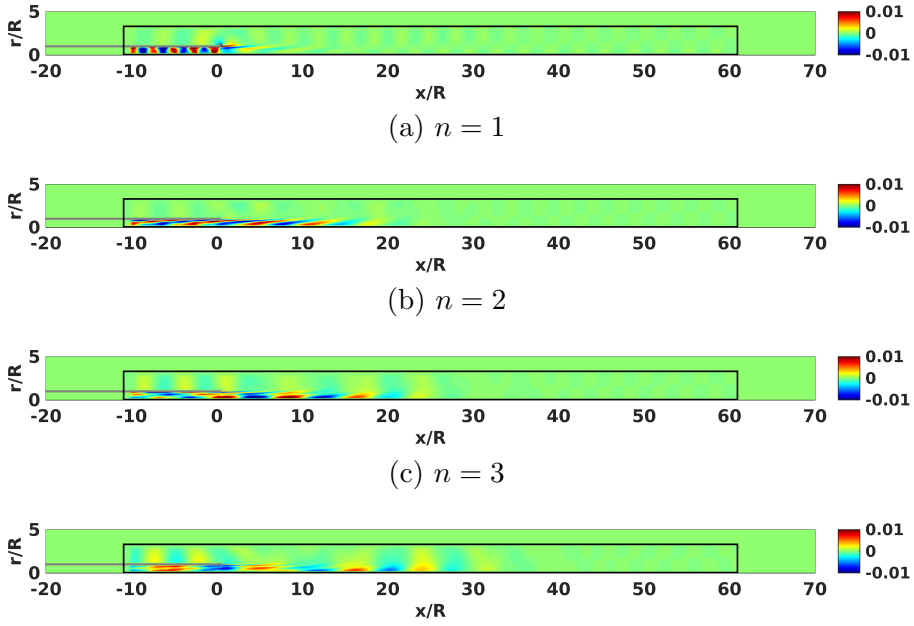

(a) $n = 1$

(b) $n = 2$

(c) $n = 3$

(d) $n = 4$

Figure 6.8: The first four input modes of the $M_j = 1.5$ supersonic heated jet with $T_j/T_\infty = 1.44$. Contours visualize the real part of the normalized axial velocity forcings for forcing frequency $St = 0.28$.

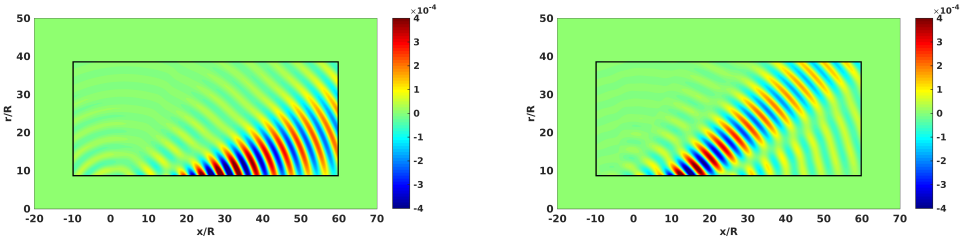

(a) $n = 1$ (b) $n = 2$

Figure 6.9: The first two input modes of the $M_j = 0.9$ subsonic heated jet with $T_j/T_\infty = 1.78$. Contours visualize the real part of the normalized output pressure perturbations for forcing frequency $St = 0.42$.

of the heated supersonic jet examined earlier. This is important because the acoustic Strouhal number was found to be a new dimensionless variable to predict the input-output behavior of jet noise in the previous section.

Figure 6.9 visualizes the first two output modes for the subsonic heated jets. While output modes show the same pattern as obtained for the supersonic heated jet, the direction of peak jet noise in this case is aligned at smaller angle of 20° as shown in figure 6.9(a).

In the study of input-output analysis for isothermal jets we showed that the optimal and the first sub-optimal ($n = 2$) input modes extended farther downstream of the nozzle exit. Unlike the subsonic isothermal jet case in section 3.3.2, figure 6.10(a) shows that the optimal inputs of this heated jet are extremely confined to the vicinity of the nozzle exit. While the first sub-optimal mode shown in figure 6.10(b) extends farther downstream, it is still shifted upstream, compared to the isothermal subsonic jet with the same jet Mach number. This indicates that applied heating makes a subsonic jet behave more like a supersonic jet; in other words, in the heated subsonic jet the largest singular value may be much greater than the second singular value. Figure 6.11 shows

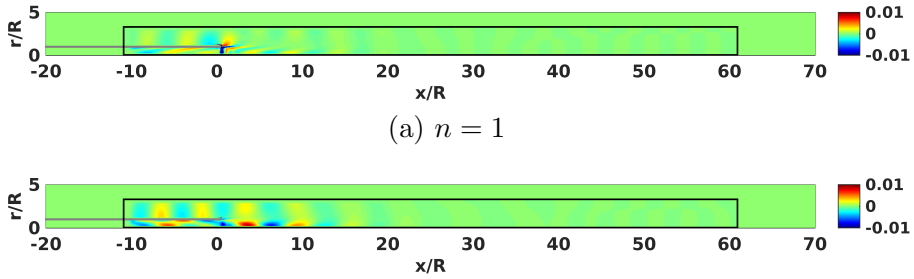

(a) $n = 1$

(b) $n = 2$

Figure 6.10: The first four input modes of the $M_j = 0.9$ supersonic heated jet with $T_j/T_\infty = 1.78$. Contours visualize the real part of the normalized axial velocity forcings for forcing frequency $St = 0.42$.

singular values vs. mode number for this subsonic heated jet and confirms that optimal gain increases with applied heating. Note that the first few sub-optimal gains were comparable to the optimal gain in isothermal subsonic jets.

6.2.3 Sound pressure level increase with applied heating

In section 3.3, it was shown that including sub-optimal modes recovers a fraction of the missing sound. To investigate the effect of heating on the sound recovery by sub-optimal modes, we consider 28 RANS base flows whose jet Mach number and acoustic Mach number vary such that $0.6 < M_j < 1.5$ and $0.6 < M_a < 1.8$. Similarly to this, we compute the amount of recovery in SPL by including sub-optimal modes using equation (3.1). Figure 6.12 shows SPL increase with respect to different acoustic Mach number for a fixed jet Mach number. Heated jets represented by open markers follow remarkably well the SPL increase fashion of the isothermal case (black closed squares), and this thus implies that applied heating triggers the onset of Mach wave radiation. This result also agrees with the change of patterns of input and output modes we observed for the subsonic heated jet with $M_j = 0.9$ and $T_j/T_\infty = 1.78$.

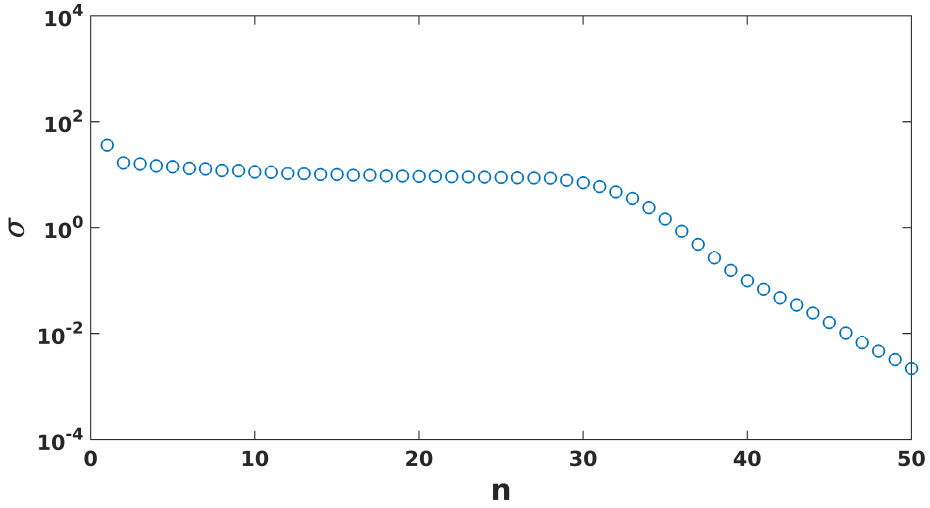

Figure 6.11: Singular values vs. mode number for the $M_j = 0.9$ jet with $T_j/T_\infty = 1.78$ at forcing frequency $St = 0.42$.

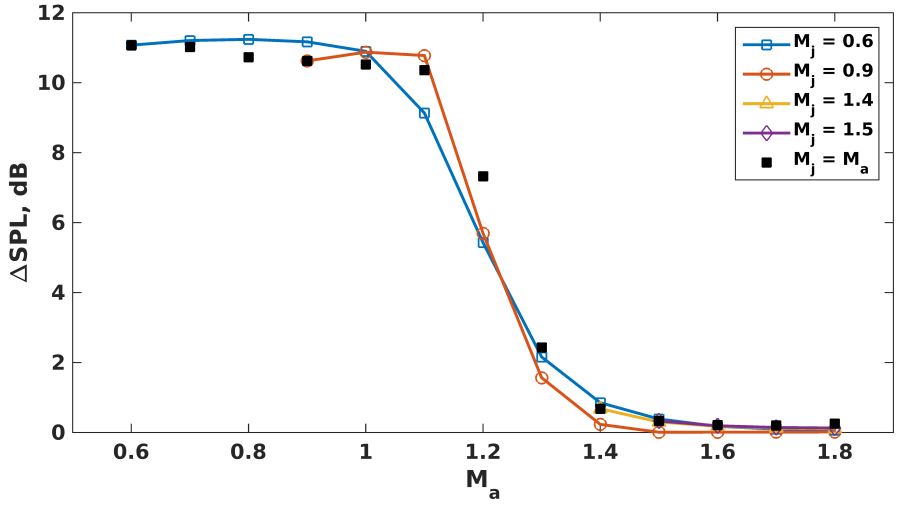

Figure 6.12: SPL increase vs. acoustic Mach number for a fixed acoustic Strouhal number $St_a = 0.50$. Black closed squares represent the result of isothermal jets and open markers show results corresponding to each jet Mach number.

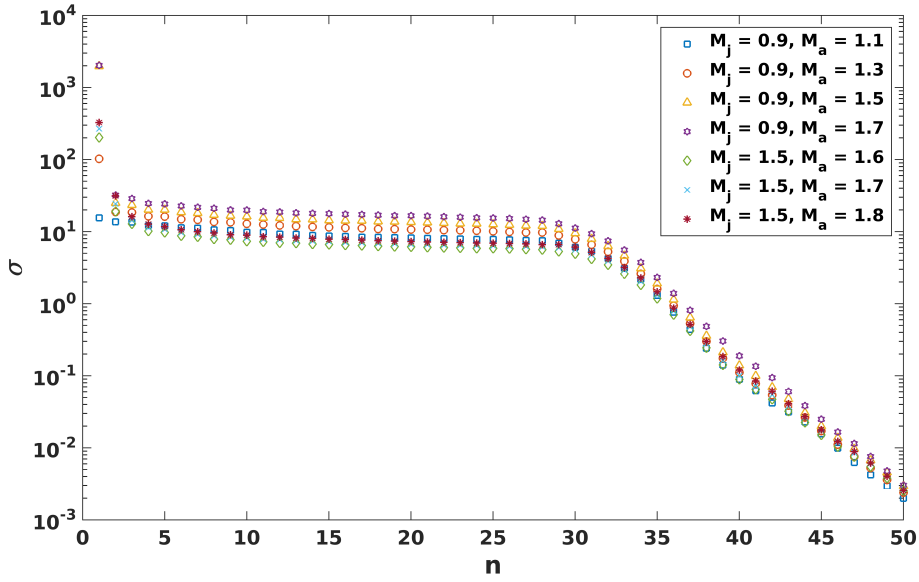

Figure 6.13: Singular values vs. mode number for heated jets with different jet-to-ambient temperature ratios keeping the acoustic Strouhal number fixed $St_a = 0.50$. Among 28 different heated jets tested, results of few selected base flows are shown.

6.2.4 Role of the acoustic Strouhal number

As introduced in section 3.2, the singular values computed using input-output analysis follow a particular pattern; after the first few modes sub-optimal gains reach a plateau that is maintained across many mode numbers. Gains then suddenly start decreasing again. Moreover, in section 6.1 it was found that the acoustic Strouhal number St_a controls the number of sub-optimal modes with significant gains. By examining heated jets with various jet Mach numbers and jet-to-ambient temperature ratios, we see that the acoustic Strouhal number can predict the sudden drop of gains, regardless of the amount of applied heating as shown in Figure 6.13.

While the acoustic Strouhal number retain the ability to predict the sudden drop of gains for heated jets as in the case of isothermal jets, in figure 6.13 sub-optimal

singular values for different base flows do not collapse to a single curve. As the amount of applied heating increases, the optimal and sub-optimal singular values shift upward. In contrast to sub-optimal singular values which strictly increase with more heating, the corresponding optimal gains start to converge as the jet-to-ambient ratio goes beyond a certain value. For some cases, this may result in the rise in ΔSPL including sub-optimal modes over some jet-to-ambient ratio (ΔSPL increases again after $M_a > 1.6$ for the $M_j = 0.9$ jet).

6.2.5 Effects of heating on sub-optimal modes

One motivation for this section was the fact that PSE analysis underpredicts the far-field acoustics, especially in the sideline direction [61]. We considered many RANS solutions of turbulent jets with different jet Mach numbers and amounts of applied heating as base flows to examine whether input-output analysis is able to recover the missing sound in such cases. The results shown in previous sections, however, seem to support that applied heating is in fact beneficial to PSE analysis. This contradiction may result from the assumption that the jet turbulence excites all modes with equal amounts of forcing. To quantify the relevance of sub-optimal modes of heated jets in the presence of realistic forcing, we therefore project high-fidelity LES data onto input modes.

We obtain an LES database for $M_j = 1.5$ supersonic jet heated with $T_j/T_\infty = 1.74$ and 5.1% axial co-flow using an unstructured finite-volume compressible flow solver. The similar procedure described in section 3.3.3 is then carried out; we take the time average of $5,000$ snapshots taken from the LES with time intervals of $0.02D/c_\infty$. We also take an average of the database in the azimuthal direction. The numerical domain of the LES extends from $x/R = 0$ to 40 and $r/R = 0$ to 10, in the axial and radial directions, respectively. As explained earlier, the RANS solutions was obtained for a larger numerical domain than the LES domain. To account for the difference in

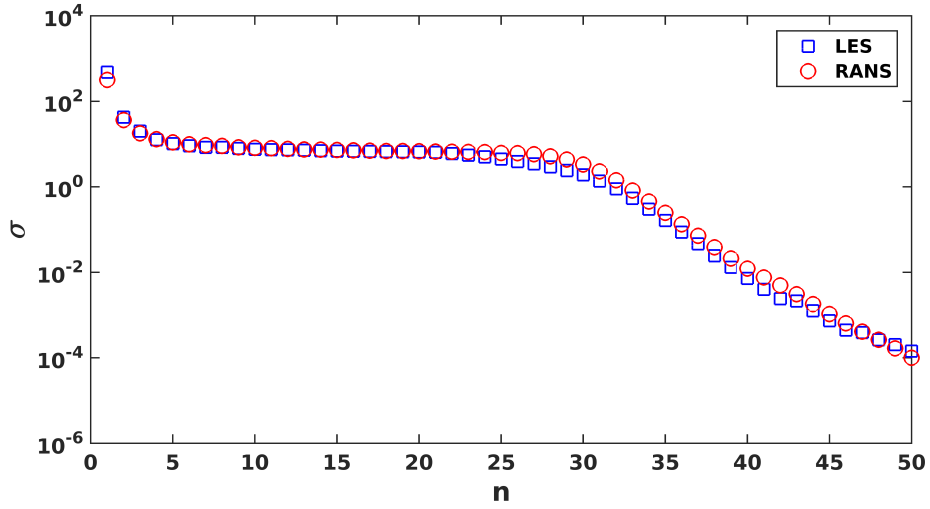

Figure 6.14: Singular values vs. mode number for the $M_j = 1.5$ jet with $T_j/T_\infty = 1.74$ for forcing frequency $St = 0.33$.

numerical domains between two base flows, the LES base flow was extrapolated to the RANS domain, and the input and output domains were restricted to $x/R = 40$ in the axial direction.

Despite differences between the two base flows, Figure 6.14 shows that the resulting singular values of two base flows agree very well. The largest differences occur for the optimal gain as well as for the sub-optimal gains near the dropoff location. Whereas the optimal singular value of the LES base flow is observed to be 1.51 times greater than that of the RANS base flow, sub-optimal singular values of the LES base flow after $n \approx 20$ are slightly smaller than those obtained from the RANS base flow. Considering the definition of SPL increase by including sub-optimal modes given by equation (3.1), this implies that the contribution of sub-optimal modes in this case becomes less significant. Again, we therefore think of the results of the LES base flow as lower bounds for this jet.

By projecting the LES forcing as derived in equation (3.3) onto the orthonormal

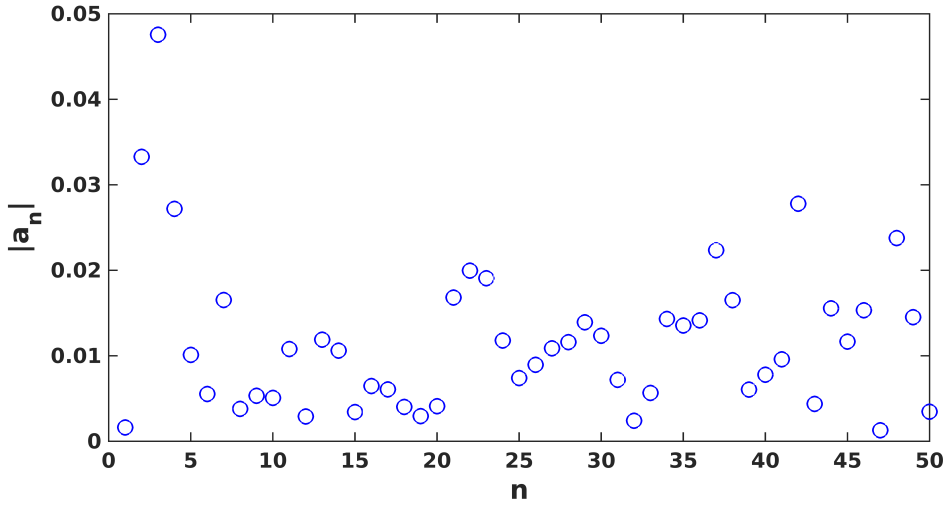

Figure 6.15: Amplitudes $|a_n|$ are determined by projecting the LES forcing onto the orthonormal set of input modes for the $M_j = 1.5$ jet with $T_j/T_\infty = 1.74$ and the azimuthal wavenumber $m = 0$ for forcing frequency $St = 0.33$.

set of input modes, the relevance of input modes in the presence of realistic forcing is quantified in the form of amplitude using equation (3.4). The amplitudes normalized by the average amplitude of the LES source are shown in figure 6.15 for the $M_j = 1.5$ jet with $T_j/T_\infty = 1.74$ for forcing frequency $St = 0.33$. Note that the amplitudes of sub-optimal modes are much larger than the amplitude of the optimal mode, and thus sub-optimal input modes are physically relevant to the realistic forcing.

Finally, we modulate the singular values obtained with the assumption of white noise forcing σ_n by the input amplitudes a_n computed from the LES projection. From equation (3.5), the contribution of sub-optimal modes with realistic forcing are measured in terms of the effective gain as shown in Figure 6.16. Without the LES forcing, SPL increase by including sub-optimal modes was computed as $0.14dB$. In the presence of realistic forcing, however, ΔSPL jumps to $7.92dB$ which represents a remarkable increase when considering the logarithmic decibel scale.

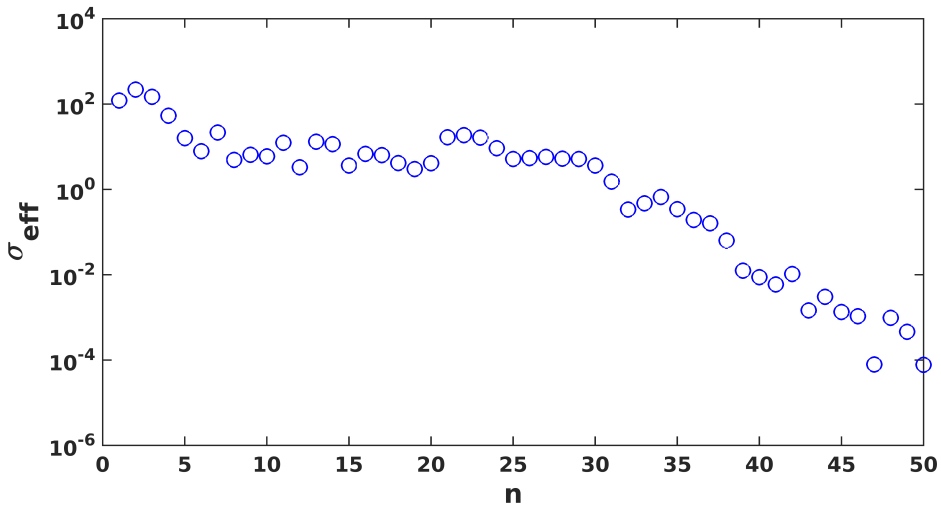

Figure 6.16: Effective gains determined by projecting the LES forcing onto the orthonormal set of input modes for the $M_j = 1.5$ jet with $T_j/T_\infty = 1.74$ and the azimuthal wavenumber $m = 0$ for forcing frequency $St = 0.33$. Singular values obtained with the white noise forcing are modulated by the input amplitudes a_n computed from the LES projection.

At the beginning of this section, we pointed out that the results obtained from the white noise forcing may imply that applied heating is advantageous to PSE analysis; this contradicts the underprediction of PSE analysis for supersonic heated jets. Using the LES projection, we demonstrate that sub-optimal modes are very significant with realistic forcing for the $M_j = 1.5$ jet with applied heating, and this may explain why PSE analysis cannot successfully capture the far-field sound of supersonic heated jets.

6.2.6 Summary

In this section, by examining various RANS solutions with jet and acoustic Mach numbers in a range of $0.6 < M_j < 1.8$ and $0.6 < M_a < 2.0$, we find that applied heating triggers disturbances to propagate through Mach wave radiation because the convection velocity of instability waves with respect to the ambient speed of sound lies in the supersonic regime in such cases. As the amount of applied heating increases, the optimal gain becomes much larger than sub-optimal gains. In this sense, one may think that applied heating in fact benefits PSE analysis. It should be noted that, however, this argument results from the assumption of white noise forcing. By projecting the LES database onto a basis of input modes, we observe that sub-optimal modes are even more relevant in the presence of realistic forcing. For the $M_j = 1.5$ heated jet with $T_j/T_\infty = 1.74$ for forcing frequency $St = 0.33$, ΔSPL owing to sub-optimal modes is found to be $7.92dB$. This is indeed a huge increase, compared to $0.14dB$ that is obtained assuming all singular directions being forced equally. We also find that acoustic Strouhal number still controls the dropoff location of sub-optimal singular values after the plateau as in the case of isothermal jets.

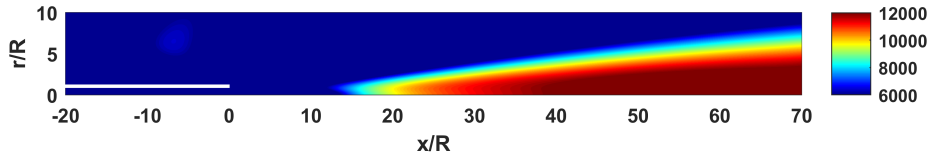

Figure 6.17: Contours of the effective viscosity for the $M_j = 1.5$ isothermal jet normalized by the constant dynamic viscosity.

6.3 Effects of eddy viscosity

Owing to the high Reynolds number of the flow, we have so far neglected the direct effect of turbulent viscosity on the perturbations. Instead, the turbulent viscosity affected the perturbations only indirectly through the base flow. To prove the validity of this assumption, the eddy viscosity solutions of base flows as obtained in figure 6.17 are incorporated in the LNS equations. The dynamics of small perturbations are now governed by the LNS equations as derived in section 2.2.

In figures 6.18 and 6.19, we present the first few pairs of output and input modes for the $M_j = 1.5$ supersonic jet. Similarly, figures 6.20 and 6.21 visualize the first two input-output modes for the $M_j = 0.9$ subsonic jet. Overall, we find that the qualitative features of input and output modes obtained using the LEE in chapter 3 are still remained unchanged. The optimal input forcing, however, now reveals the Orr-type tilted structure against the shear near the nozzle boundary and also shows some centerline mode, which develops into the jet column mode as it proceeds downstream. Figure 6.22 zooms in the optimal input mode around the nozzle for the $M_j = 0.9$ jet and more clearly shows active Orr-like mechanism. These are not obtained from input-output analysis of the LEE, but they agree well with the Orr mechanism observed from resolvent analysis of boundary layers [111].

The curves of singular values and input-output modes obtained in the present section

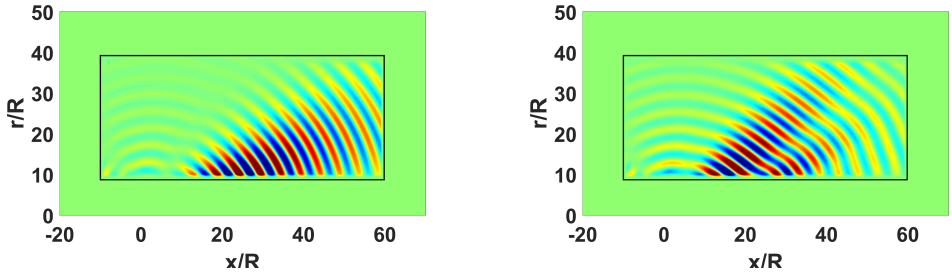

(a) $n = 1$ (b) $n = 2$

Figure 6.18: The first two output modes of the $M_j = 1.5$ supersonic jet for forcing frequency $St = 0.32$. Contours visualize the real part of normalized output pressure fluctuations governed by the LNS equations.

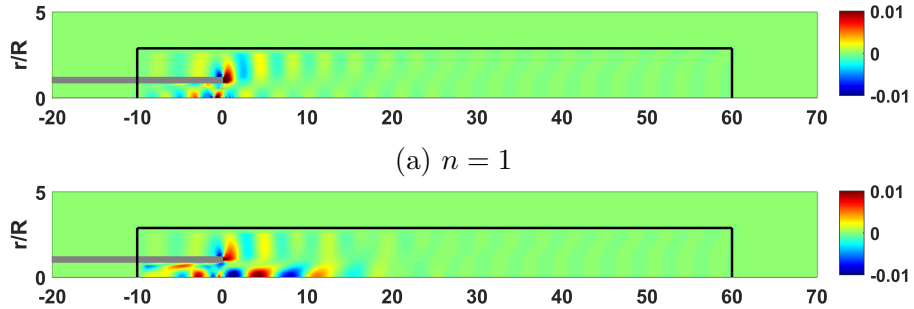

(a) $n = 1$

(b) $n = 2$

Figure 6.19: The first two input modes of the $M_j = 1.5$ supersonic jet for forcing frequency $St = 0.32$. Contours of the real part of the normalized axial velocity forcing governed by the LNS equations are shown.

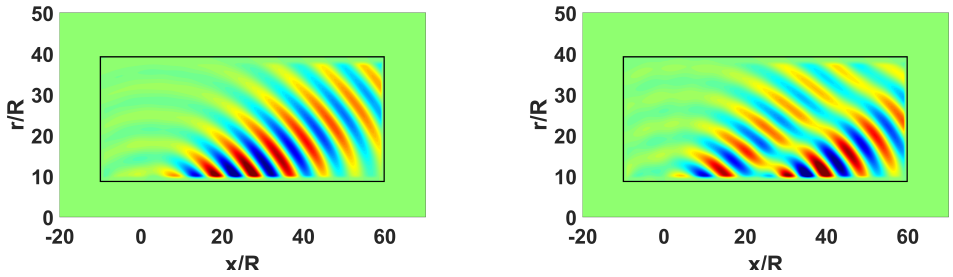

(a) $n = 1$ (b) $n = 2$

Figure 6.20: The first two output modes of the $M_j = 0.9$ subsonic jet for forcing frequency $St = 0.32$. Contours visualize the real part of normalized output pressure fluctuations governed by the LNS equations.

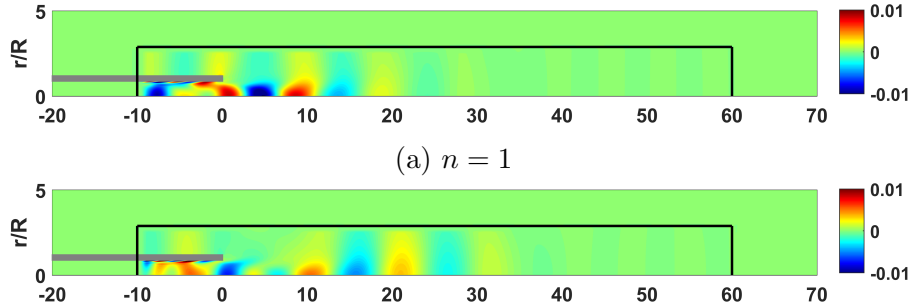

(a) $n = 1$

(b) $n = 2$

Figure 6.21: The first two input modes of the $M_j = 0.9$ subsonic jet for forcing frequency $St = 0.32$. Contours of the real part of the normalized axial velocity forcing governed by the LNS equations are shown.

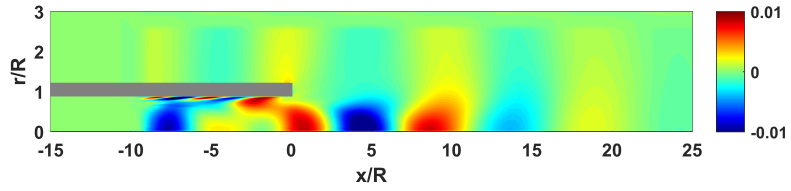

Figure 6.22: The optimal input mode of the $M_j = 0.9$ isothermal jet for forcing frequency $St = 0.32$ zoomed in near the nozzle wall. Contours visualizes the real part of the normalized axial velocity forcing.

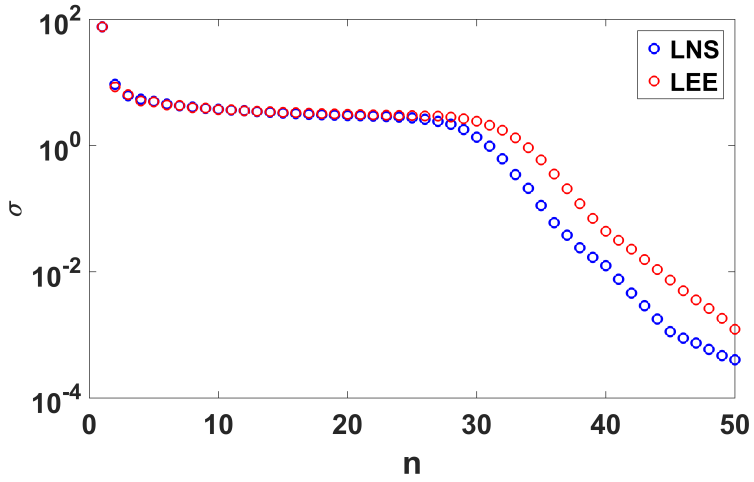

Figure 6.23: Singular values vs. mode number for the $M_j = 1.5$ supersonic jet with forcing frequency $St = 0.32$. The viscous (marked by LNS) and inviscid (marked by LEE) results are shown together for comparison.

using the LNS equations preserve the same qualitative behavior of small perturbations governed by the LEE. Moreover, the first 50 singular values in both cases are plotted together in one plane and matches very well before a dropoff location as shown in figure 6.23. This implies that the eddy viscosity has little effects to the relative importance of the sub-optimal modes at this high Reynolds numbers ($Re = 10^6$). After that point, singular values computed from the perturbations governed by the LNS equations damps much quickly, and this may well be probably due to the eddy viscosity added in this case.

6.4 Higher azimuthal wavenumber modes

So far, we have studied axisymmetric disturbances $m = 0$ about RANS base flows. While axisymmetric disturbances dominate the acoustic response of turbulent jets, first

few higher azimuthal wavenumber modes are, in fact, also known to be important particularly in the sideline direction [51, 52, 63, 96]. In this sense, in addition to an axisymmetric disturbances, we consider helical ($m = 1$) and double helical ($m = 2$) disturbances. Furthermore, to account for the effects of eddy viscosity, we consider the dynamics of small perturbations, which are governed by the LNS equations incorporated with the effective viscosity. The resulting optimal output modes for the helical and double helical perturbations for the $M_j = 1.5$ supersonic jet are respectively presented in figures 6.24(a) and (b).

Figure 6.25 compares the first 50 singular values of all three azimuthal wavenumber modes for the $M_j = 1.5$ supersonic jet. As expected, the optimal gain for the axisymmetric mode ($m = 0$) dominates the response. One may find that sub-optimal modes, however, become increasingly important as the azimuthal wavenumber increases.

Figure 6.26 represents the directivity of pressure perturbations at $r/R = 10$ for each azimuthal wavenumber mode as a function of polar angle ϕ, which is measured from the downstream jet axis. The axisymmetric mode dominates acoustic radiations in the direction of peak jet noise. On the contrary, sideline noise is better explained by higher azimuthal wavenumber modes.

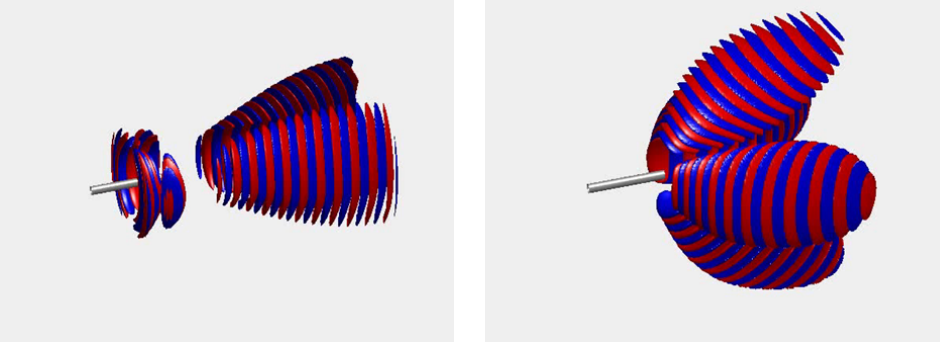

(a) $m = \pm 1$ (b) $m = \pm 2$

Figure 6.24: The optimal output modes for the (a) helical and (b) double helical modes for the $M_j = 1.5$ supersonic jet with forcing frequency $St = 0.32$.

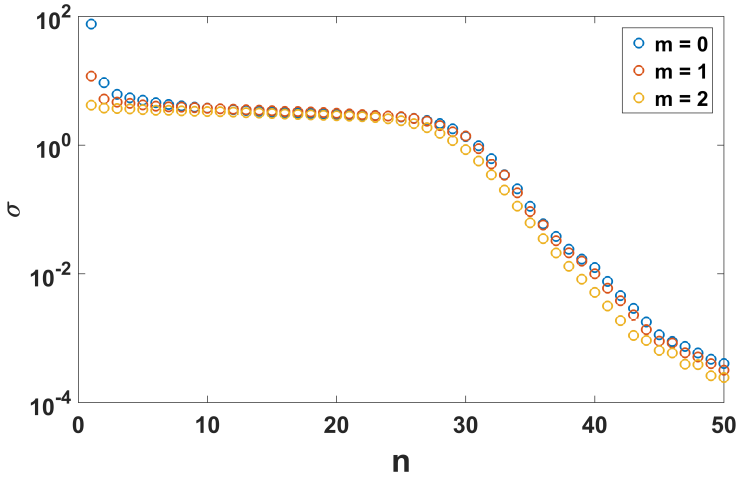

Figure 6.25: The first 50 singular values for the axisymmetric ($m = 0$), helical ($m = 1$), and double helical ($m = 2$) disturbances for the $M_j = 1.5$ supersonic jet with forcing frequency $St = 0.32$.

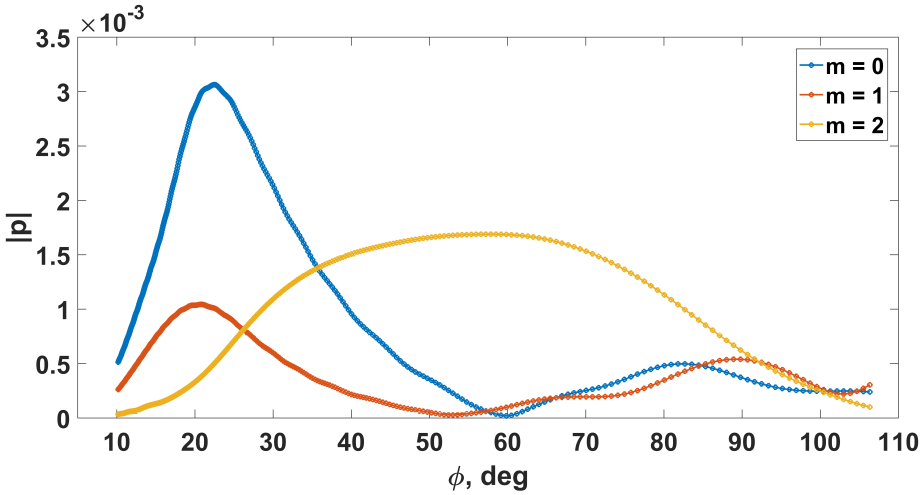

(a) $M_j = 1.5$

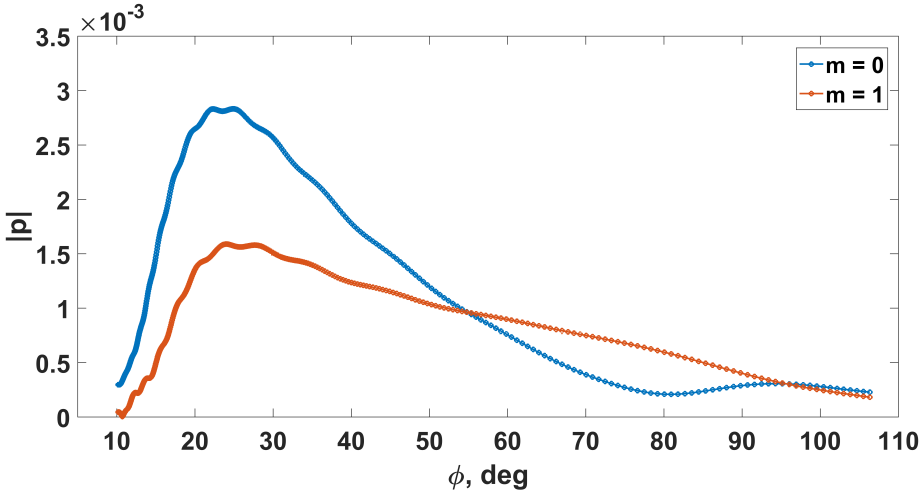

(b) $M_j = 0.9$

Figure 6.26: Far-field pressure perturbations as a function of polar angle ϕ measured from the downstream jet axis. Axisymmetric ($m = 0$), helical ($m = 1$), and double helical disturbances ($m = 2$) are shown together for the (a) $M_j = 1.5$ supersonic jet and (b) $M_j = 0.9$ subsonic jet with forcing frequency $St = 0.32$.

Chapter 7

Concluding remarks

7.1 Summary and conclusions

The present study considers input-output analysis of small perturbations about RANS and LES base flows for subsonic and supersonic jets. By specifying an input domain to be forcings to velocity equations in the vicinity of jet turbulence and an output domain to be pressure perturbations in the region far away from jets, our analysis studies how input forcings map onto output quantities of interests. The dynamics of small perturbations about the base flows are governed either by the LEE or by the LNS equations to account for the effects of eddy viscosity. Compared to the analysis of LEE, input-output analysis of small perturbations governed by the LNS equations preserves the same qualitative behavior except for that in this case the input modes incorporate the Orr mechanism (vortex tilting).

Input-output analysis yields orthonormal sets of input and output modes by taking the singular value decomposition of the resolvent operator, corresponding to the linearized governing equations. We first focus on the axisymmetric disturbances only. For a given frequency, the leading output mode, concerned with the largest singular value,

recovers a convectively unstable wavepacket similar to that obtained by the PSE. While the leading output mode represents the optimal linear response to forcing, input-output analysis also predicts a range of sub-optimal modes, associated with lesser singular values. These sub-optimal modes correspond to additional coherent forcings and responses. Moreover, the sub-optimal output modes follow a regular pattern, where acoustic radiation is organized into an increasing number of acoustic beams leaving the jet at different angles. As the mode number increases, output modes tend to include additional acoustic beams oriented both towards the sideline direction and low angles with respect to the jet axis.

We further assess the relevance of sub-optimal modes by projecting data obtained from the LES of $M_j = 1.5$ supersonic jet onto the orthonormal sets of singular directions resulting from input-output analysis. Projection onto input modes determines the relative amplitude of each mode, as forced by the jet turbulence. We find that sub-optimal modes are indeed active, even in this case which is otherwise dominated by the optimal mode. In fact, taking into account sub-optimal modes with projected amplitudes increases the output sound pressure level by 0.37 dB in this case. The LES data projection onto the output modes confirms their physical relevance and further demonstrates the potential of input-output analysis as reduced-order modeling of jet noise. With only 24 modes, input-output analysis recovers a substantial amount of the acoustic energy predicted by the LES.

To handle the far-field sound projection directly within input-output analysis framework, an FW-H formulation is implemented as a linear operator inside the matrix C. Using the hybrid input-output/FW-H method, a significant portion of the LES acoustic energy of both the isothermal and the heated supersonic jets is recovered for observers along a full-arc at a distance of 200 jet radii away from the nozzle exit. Output-mode-reconstructed acoustic fields predict the correct directivity of the LES database, using

30 and 38 modes, respectively for the isothermal and heated jets. Furthermore, we perform input-output analysis over a range of frequencies at two different polar angles. Here, we consider small disturbances with first few dominant azimuthal wavenumber modes (up to $m = 2$). As the polar angle increases, our method predicts that the far-field spectra broaden. Similar effects are observed in experiments [93, 112] and are predicted by LES. Our spectra also closely resemble theoretical predictions, which are based on models constructed entirely from similarity wavepackets [105].

In the literature, it has been suggested that turbulent mixing noise is best represented by a two source model [93, 112]. In particular, experimental measurements seem to fit two independent mechanisms of jet noise generation. In this view, one mechanism is associated with large-scale coherent structures and is responsible for downstream acoustic radiation known as the large-scale spectrum (LSS). The other mechanism is thought to be more incoherent and omnidirectional in nature and creates the fine-scale spectrum (FSS). As recently argued, however, it may be possible to model jet noise with a single source model which does not separate between LSS and FSS [52, 105]. Our results further suggest that sideline radiation can be explained by coherent mechanisms associated with sub-optimal modes, in addition to the downstream radiation associated with the optimal mode. Based on the LES data projection onto the set of output modes, we find that including sub-optimal modes results in a 10-20 dB increase in far-field SPL for polar angles $\phi > 40^\circ$ for the $M_j = 1.5$ supersonic jet.

The physics of coherent structures captured by input modes are investigated thoroughly for the $M_j = 0.9$ subsonic jet. The $M_j = 0.9$ subsonic jets have been the subject of several other experimental and numerical investigations. They support wavepackets as acoustic sources, but noise radiation is severely underpredicted in many wavepacket modeling approaches in this case. To consider acoustically relevant sources only, input forcings are weighted by the TKE. Input-output analysis indicates that the optimal

input mode resemble wavepackets, which are spatially and temporally modulated while traveling downstream. More specifically, they are found to be positively skewed bell-shaped structures as observed in other wavepacket modeling approaches [56, 62, 63, 103, 104, 105]. After examining several wavepacket models, we find that optimal input modes correspond to wavepackets represented by asymmetric pseudo-Gaussian envelope functions at a given forcing frequency. These wavepackets remain similar in shape over a range of frequencies for $St > 0.5$, and scale as $St^{-0.5}$. While the optimal mode is a wavepacket, sub-optimal modes represent decoherence of the optimal input mode.

By investigating input wavepackets and associated acoustic radiation to specific angles, we find that input modes do indeed serve as realistic, non-compact coherent sources relevant to far-field sound generated by turbulent jets at any angles. These wavepackets are those who cooperate to complete the overall acoustic field spanning a wide range of polar angles. More specifically, at lower radiation angle than the peak noise angle, the input mode represents jitter or decoherence of the optimal input forcing for full-arc outputs. Wavepackets radiating sound at large angles, on the other hand, become more compact as radiation angle increases and thus more efficient. Furthermore, by repeating our analysis over a range of frequencies, we show that more degrees of freedom are needed in terms of the azimuthal wavenumber as radiation angle rotates towards the sideline direction, revealing broadening of spectra as radiation angle increases at high frequencies.

Lastly, we construct parametric studies; we investigate the effect of jet Mach number on the importance of sub-optimal modes in the prediction of jet noise. To do this, we generate 13 different base flows with various jet Mach numbers, spanning $M_j = 0.6$ to 1.8. For supersonic jets, the largest singular value is much greater in magnitude than any of the others, and thus, the acoustic response is dominated by the leading output mode. Additionally, the leading input mode in this case is confined inside the nozzle

and in the immediate vicinity of its exit. Physically, this agrees with an instability wave mechanism triggered by a small upstream disturbance, and analysis of the PSE successfully predicts the acoustic response in this case. For subsonic jets, however, the gains corresponding to sub-optimal modes are comparable to the amplification of the leading mode and therefore cannot be neglected. This study also suggests the importance of a new dimensionless parameter, the acoustic Strouhal number St_a defined in terms of the free-stream speed of sound. We show that the acoustic Strouhal number determines the number of significant sub-optimal modes regardless of the jet Mach number. By retaining only the optimal mode and the significant sub-optimal modes, we may construct an accurate but minimal reduced-order model of noise generation at a given frequency.

In addition, we examine small disturbances about RANS and LES base flows for heated jets. For various RANS solutions with jet and acoustic Mach numbers ranging $0.6 < M_j < 1.8$ and $0.6 < M_a < 2.0$, we find that applied heating triggers disturbances to propagate through Mach wave radiation because the convection velocity of instability waves with respect to the ambient speed of sound lies in the supersonic regime in such cases. As the amount of applied heating increases, the optimal gain becomes much larger than sub-optimal gains. Based on this, one may think that applied heating in fact benefits PSE analysis, which contradicts the previous observation that PSE analysis breakdowns for supersonic heated jets. It should be noted that, however, this argument results from the assumption of white noise forcing. By projecting the LES database onto a basis of input modes, we observe that sub-optimal modes are even more relevant in the presence of realistic forcing.

The effects of eddy viscosity are also investigated. To do so, they are incorporated in the LNS equations. In this way, input forcings reveal tilted structures along the nozzle wall; at this high Reynolds number, however, the eddy viscosity has little effects to

the relative importance of the sub-optimal modes. The higher azimuthal wavenumber modes, on the other hand, increase the significance of sub-optimal modes. In particular, sideline noise is better explained by them than by the axisymmetric mode alone.

7.2 Future work

We have analyzed small perturbations about RANS and LES base flows to predict and understand the aeroacoustics of high-speed turbulent jets. We utilize the LES database for both supersonic and subsonic jets to assess the physical relevance of input-output modes under the realistic volumetric forcing. In order for our method itself to be a more predictive model for turbulent jet noise, without the use of high-fidelity simulations, we may want a low-rank modeling of realistic forcings from known properties as suggested in [113, 114, 115, 116].

The sensitivity analysis of turbulent jet noise can also be used as an industrial design tool for a quieter jet engine. High-fidelity simulations such as DNS or LES require a number of iterations to find optimal design parameters by examining various possible scenarios, but even a single iteration costs a lot. Our analysis, on the other hand, may be utilized to provide a noise control strategy in less computationally expensive way through a base flow modification, in conjunction with modeling techniques to reproduce flow statistics that are mentioned above.

Finally, though we limit our interest to turbulent jets exhausted from a straight cylindrical nozzle, our approach is universal and may be applied to nozzles with more complex geometries such as the chevroned [24, 25] or faceted [26] engines. Particularly, it is known that chevrons can reduce the overall noise substantially. Input-output analysis may be extended to study the sensitivity of small perturbations for such geometries and to understand their noise reduction mechanisms.

References

[1] G. A. Brès, J. W. Nichols, S. K. Lele, and F. E. Ham. Towards best practices for jet noise predictions with unstructured large eddy simulations. *AIAA Paper 2012-2965*, 2012.

[2] C. J. Moore. The role of shear-layer instability waves in jet exhaust noise. *Journal of Fluid Mechanics*, 80(2):321–367, 1977.

[3] S. C. Crow and F. H. Champagne. Orderly structure in jet turbulence. *Journal of Fluid Mechanics*, 48(03):547–591, 1971.

[4] P. Jordan, T. Colonius, G. A. Bres, M. Zhang, A. Towne, and S. K. Lele. Modeling intermittent wavepackets and their radiated sound in a turbulent jet. In *Proceedings of the Summer Program*, page 241. Center for Turbulence Research, Stanford University, 2014.

[5] FAA aerospace forecast: Fiscal years 2018-2038. Technical report, Federal Aviation Administration, 2018.

[6] Report on jet engine noise reduction. Technical report, Naval Research Advisory Committee, 2009.

[7] D. L. Huff. NASA Glenn's contributions to aircraft engine noise research. *Journal of Aerospace Engineering*, 26(2), 2013.

[8] A. P. Dowling and J. E. Ffowcs Williams. *Sound and sources of sound*. Horwood, 1983.

[9] M. J. Lighthill. On sound generated aerodynamically. I. general theory. *Proceedings of the Royal Society of London. Series A, Mathematical and Physical Sciences*, pages 564–587, 1952.

[10] M. E. Goldstein and S. J. Leib. The aeroacoustics of slowly diverging supersonic jets. *Journal of Fluid Mechanics*, 600:291–337, 2008.

[11] S. A. Karabasov, M. Z. Afsar, T. P. Hynes, A. P. Dowling, W. A. McMullan, C. D. Pokora, G. J. Page, and J. J. McGuirk. Jet noise: acoustic analogy informed by large eddy simulation. *AIAA journal*, 48(7):1312–1325, 2010.

[12] O. M. Phillips. On the generation of sound by supersonic turbulent shear layers. *Journal of Fluid Mechanics*, 9(1):1–28, 1960.

[13] N. Curle. The influence of solid boundaries upon aerodynamic sound. *Proceedings of the Royal Society of London A: Mathematical, Physical and Engineering Sciences*, 231(1187):505–514, 1955.

[14] J. E. Ffowcs Williams. The noise from turbulence convected at high speed. *Philosophical Transactions of the Royal Society of London A: Mathematical, Physical and Engineering Sciences*, 255(1061):469–503, 1963.

[15] G. M. Lilley. On the noise from jets. Agard-cp-131, Advisory Group for Aeronautical Research and Development, 1974.

[16] M. E. Goldstein. A generalized acoustic analogy. *Journal of Fluid Mechanics*, 488:315–333, 2003.

[17] J. B. Freund, S. K. Lele, and P. Moin. Numerical simulation of a Mach 1.92 turbulent jet and its sound field. *AIAA journal*, 38(11):2023–2031, 2000.

[18] J. B. Freund. Noise sources in a low-Reynolds-number turbulent jet at Mach 0.9. *Journal of Fluid Mechanics*, 438:277–305, 2001.

[19] C. Bogey, C. Bailly, and D. Juvé. Noise investigation of a high subsonic, moderate Reynolds number jet using a compressible large eddy simulation. *Theoretical and Computational Fluid Dynamics*, 16(4):273–297, 2003.

[20] D. J. Bodony and S. K. Lele. On using large-eddy simulation for the prediction of noise from cold and heated turbulent jets. *Physics of Fluids*, 17(8):085103, 2005.

[21] G. A. Brès, V. Jaunet, M. Le Rallic, P. Jordan, T. Colonius, and S. K. Lele. Large eddy simulation for jet noise: the importance of getting the boundary layer right. *AIAA Paper 2015-2535*, 2015.

[22] S. Mendez, M. Shoeybi, S. K. Lele, and P. Moin. On the use of the Ffowcs Williams-Hawkings equation to predict far-field jet noise from large-eddy simulations. *International Journal of Aeroacoustics*, 12(1-2):1–20, 2013.

[23] D. Dahl, J. Jeun, and J. W. Nichols. Large eddy simulation of a tactical aircraft exhaust nozzle with free-stream and wall turbulence. *AIAA Paper 2015-2373*, 2015.

[24] H. Xia, P. G. Tucker, and S. Eastwood. Large-eddy simulations of chevron jet flows with noise predictions. *International Journal of Heat and Fluid Flow*, 30(6):1067–1079, 2009.

[25] J. W. Nichols, S. K. Lele, P. Moin, F. E. Ham, G. A. Brès, and J. Bridges. Large-eddy simulation for supersonic rectangular jet noise prediction: effects of chevrons. *AIAA Paper 2012-2212*, 2012.

[26] R. Powers and D. McLaughlin. Acoustics measurements of scale models of military style supersonic beveled nozzle jets with interior corrugations. *AIAA Paper 2012-2116*, 2012.

[27] D. J. Bodony and S. K. Lele. Current status of jet noise predictions using large-eddy simulation. *AIAA journal*, 46(2):364–380, 2008.

[28] F. Farassat and M. K. Myers. Extension of Kirchhoff′s formula to radiation from moving surfaces. *Journal of Sound and Vibration*, 123(3):451–460, 1988.

[29] A. D. Pierce. *Acoustics: an introduction to its physical principles and applications*. Acoustical Society of America, 1989.

[30] K. S. Brentner and F. Farassat. Analytical comparison of the acoustic analogy and Kirchhoff formulation for moving surfaces. *AIAA journal*, 36(8):1379–1386, 1998.

[31] J. E. Ffowcs Williams and D. L. Hawkings. Sound generation by turbulence and surfaces in arbitrary motion. *Phil. Trans. R. Soc. Lond. A*, 264(1151):321–342, 1969.

[32] P. Di Francescantonio. A new boundary integral formulation for the prediction of sound radiation. *Journal of Sound and Vibration*, 202(4):491–509, 1997.

[33] D. P. Lockard. An efficient, two-dimensional implementation of the Ffowcs Williams and Hawkings equation. *Journal of Sound and Vibration*, 229(4):897–911, 2000.

[34] M. L. Shur, P. R. Spalart, and M. Kh. Strelets. Noise prediction for increasingly complex jets. part II: Applications. *International Journal of Aeroacoustics*, 4(3):247–266, 2005.

[35] P. R. Spalart and M. L. Shur. Variants of the Ffowcs Williams-Hawkings equation and their coupling with simulations of hot jets. *International journal of aeroacoustics*, 8(5):477–491, 2009.

[36] E. Mollo-Christensen. Measurements of near field pressure of subsonic jets. Technical report, Advisory Group for Aeronautical Research and Development, 1963.

[37] E. Mollo-Christensen. Jet noise and shear flow instability seen from an experimenter′s viewpoint. *Journal of Applied Mechanics*, 34(1):1–7, 1967.

[38] H. V. Fuchs. Measurement of pressure fluctuations within subsonic turbulent jets. *Journal of Sound and Vibration*, 22(3):361–378, 1972.

[39] H. V. Fuchs. Space correlations of the fluctuating pressure in subsonic turbulent jets. *Journal of sound and vibration*, 23(1):77–99, 1972.

[40] J. Seiner and G. Reethof. On the distribution of source coherency in subsonic jets. *AIAA Paper 74-4*, 1974.

[41] R. R. Armstrong, A. Michalke, and H. V. Fuchs. Coherent structures in jet turbulence and noise. *AIAA Journal*, 15(7):1011–1017, 1977.

[42] A. Michalke. A wave model for sound generation in circular jets. Technical report, Deutsche Luft- und Raumfahrt, 1970.

[43] A. Michalke. An expansion scheme for the noise from circular jets. *Z. Flugwiss.*, 1972.

[44] G. E. Mattingly and C. C. Chang. Unstable waves on an axisymmetric jet column. *Journal of Fluid Mechanics*, 65(3):541–560, 1974.

[45] D. G. Crighton and M. Gaster. Stability of slowly diverging jet flow. *Journal of Fluid Mechanics*, 77(2):397–413, 1976.

[46] A. Michalke. Survey on jet instability theory. *Progress in Aerospace Sciences*, 21:159–199, 1984.

[47] C. K. W. Tam and D. E. Burton. Sound generated by instability waves of supersonic flows. Part 2. Axisymmetric jets. *Journal of Fluid Mechanics*, 138:273–295, 1984.

[48] T. Suzuki and T. Colonius. Instability waves in a subsonic round jet detected using a near-field phased microphone array. *Journal of Fluid Mechanics*, 565:197–226, 2006.

[49] A. Michalke. Instability of a compressible circular free jet with consideration of the influence of the jet boundary layer thickness. *Z. Flugwiss.*, 1971.

[50] J. E. Ffowcs Williams and A. J. Kempton. The noise from the large-scale structure of a jet. *Journal of Fluid Mechanics*, 84(4):673–694, 1978.

[51] A. V. G. Cavalieri, P. Jordan, A. Agarwal, and Y. Gervais. Jittering wave-packet models for subsonic jet noise. *Journal of Sound and Vibration*, 330(18):4474–4492, 2011.

[52] P. Jordan and T. Colonius. Wave packets and turbulent jet noise. *Annual Review of Fluid Mechanics*, 45:173–195, 2013.

[53] A. Michalke and H. V. Fuchs. On turbulence and noise of an axisymmetric shear flow. *Journal of Fluid Mechanics*, 70(1):179–205, 1975.

[54] C. K. W. Tam. On the noise of a nearly ideally expanded supersonic jet. *Journal of Fluid Mechanics*, 51(1):69–95, 1972.

[55] C. K. W. Tam and P. J. Morris. The radiation of sound by the instability waves of a compressible plane turbulent shear layer. *Journal of Fluid Mechanics*, 98(2):349–381, 1980.

[56] Y. B. Baqui, A. Agarwal, A. V. G. Cavalieri, and S. Sinayoko. A coherence-matched linear source mechanism for subsonic jet noise. *Journal of Fluid Mechanics*, 776:235–267, 2015.

[57] A. V. G. Cavalieri, D. Rodríguez, P. Jordan, T. Colonius, and Y. Gervais. Wavepackets in the velocity field of turbulent jets. *Journal of fluid mechanics*, 730:559–592, 2013.

[58] L. C. Cheung, D. J. Bodony, and S. K. Lele. Noise radiation predictions from jet instability waves using a hybrid nonlinear PSE-acoustic analogy approach. *AIAA Paper 2007-3638*, 2007.

[59] K. Gudmundsson and T. Colonius. Instability wave models for the near-field fluctuations of turbulent jets. *Journal of Fluid Mechanics*, 689:97–128, 2011.

[60] D. Rodríguez, A. Sinha, G. A. Brès, and T. Colonius. Inlet conditions for wave packet models in turbulent jets based on eigenmode decomposition of large eddy simulation data. *Physics of Fluids*, 25(10):105107, 2013.

[61] A. Sinha, D. Rodríguez, G. A. Brès, and T. Colonius. Wavepacket models for supersonic jet noise. *Journal of Fluid Mechanics*, 742:71–95, 2014.

[62] R. Reba, S. Narayanan, and T. Colonius. Wave-packet models for large-scale mixing noise. *International Journal of Aeroacoustics*, 9(4-5):533–557, 2010.

[63] A. V. G. Cavalieri, P. Jordan, T. Colonius, and Y. Gervais. Axisymmetric superdirectivity in subsonic jets. *Journal of fluid Mechanics*, 704:388–420, 2012.

[64] A. Towne and T. Colonius. Improved parabolization of the Euler equations. *AIAA Paper 2013-2171*, 2013.

[65] M. R. Jovanović. *Modeling, analysis, and control of spatially distributed systems*. PhD thesis, University of California, Santa Barbara, 2004.

[66] M. R. Jovanović and B. Bamieh. Componentwise energy amplification in channel flows. *Journal of Fluid Mechanics*, 534:145–183, 2005.

[67] J. W. Nichols and M. R. Jovanović. Input-output analysis of high-speed jet noise. In *Proceedings of the Summer Program*, pages 251–260. Center for Turbulence Research, Stanford University, 2014.

[68] J. Jeun, J. W. Nichols, and M. R. Jovanović. Input-output analysis of high-speed axisymmetric isothermal jet noise. *Physics of Fluids*, 28(4):047101, 2016.

[69] L. N. Trefethen, A. E. Trefethen, S. C. Reddy, and T. A. Driscoll. Hydrodynamic stability without eigenvalues. *Science*, 261(5121):578–584, 1993.

[70] B. F. Farrell and P. J. Ioannou. Stochastic forcing of the linearized navier–stokes equations. *Physics of Fluids A: Fluid Dynamics*, 5(11):2600–2609, 1993.

[71] P. J. Schmid and D. S. Henningson. *Stability and transition in shear flows*, volume 142 of *Applied mathematical sciences*. Springer, 2001.

[72] B. J. McKeon and A. S. Sharma. A critical-layer framework for turbulent pipe flow. *Journal of Fluid Mechanics*, 658:336–382, 2010.

[73] X. Garnaud, L. Lesshafft, P. J. Schmid, and P. Huerre. The preferred mode of incompressible jets: linear frequency response analysis. *Journal of Fluid Mechanics*, 716:189–202, 2013.

[74] D. J. Bodony. Analysis of sponge zones for computational fluid mechanics. *Journal of Computational Physics*, 212(2):681–702, 2006.

[75] Y. Khalighi, A. Mani, F. Ham, and P. Moin. Prediction of sound generated by complex flows at low Mach numbers. *AIAA journal*, 48(2):306–316, 2010.

[76] A. Mani. Analysis and optimization of numerical sponge layers as a nonreflective boundary treatment. *Journal of Computational Physics*, 231(2):704–716, 2012.

[77] J. W. Nichols, S. K. Lele, and P. Moin. Global mode decomposition of supersonic jet noise. Annual research briefs, Center for Turbulence Reearch, Stanford University, 2009.

[78] J. W. Nichols and S. K. Lele. Global modes and transient response of a cold supersonic jet. *Journal of Fluid Mechanics*, 669:225–241, 2011.

[79] D. C. Hill. Adjoint systems and their role in the receptivity problem for boundary layers. *Journal of Fluid Mechanics*, 292:183–204, 1995.

[80] P. J. Schmid. Nonmodal stability theory. *Annu. Rev. Fluid Mech.*, 39:129–162, 2007.

[81] S. J. Leib and M. E. Goldstein. Hybrid source model for predicting high-speed jet noise. *AIAA journal*, 49(7):1324–1335, 2011.

[82] R. B. Lehoucq, D. C. Sorensen, and C. Yang. *Users' Guide: Solution of Large-Scale Eigenvalue Problems with Implicitly Restarted Arnoldi Methods*. SIAM, 1998.

[83] X. S. Li and J. W. Demmel. SuperLU DIST: A scalable distributed-memory sparse direct solver for unsymmetric linear systems. *ACM Transactions on Mathematical Software (TOMS)*, 29(2):110–140, 2003.

[84] A. Jameson. Aerodynamic design via control theory. *Journal of scientific computing*, 3(3):233–260, 1988.

[85] A. Jameson. Re-engineering the design process through computation. *Journal of Aircraft*, 36(1):36–50, 1999.

[86] J. C. Newman III, A. C. Taylor III, R. W. Barnwell, P. A. Newman, and G. J.-W. Hou. Overview of sensitivity analysis and shape optimization for complex aerodynamic configurations. *Journal of Aircraft*, 36(1):87–96, 1999.

[87] S. Nadarajah and A. Jameson. A comparison of the continuous and discrete adjoint approach to automatic aerodynamic optimization. *AIAA Paper 2000-0667*, 2000.

[88] G. J. Chandler, M. P. Juniper, J. W. Nichols, and P. J. Schmid. Adjoint algorithms for the Navier-Stokes equations in the low Mach number limit. *Journal of Computational Physics*, 231(4):1900–1916, 2012.

[89] M. L. Shur, P. R. Spalart, and M. Kh. Strelets. Noise prediction for increasingly complex jets. Part I: Methods and tests. *International journal of aeroacoustics*, 4(3):213–245, 2005.

[90] A. T. Thies and C. K. W. Tam. Computation of turbulent axisymmetric and nonaxisymmetric jet flows using the k-ε model. *AIAA journal*, 34(2):309–316, 1996.

[91] C. K. W. Tam. Supersonic jet noise. *Annual Review of Fluid Mechanics*, 27(1):17–43, 1995.

[92] X. Garnaud, R. D. Sandberg, and L. Lesshafft. Global response to forcing in a subsonic jet: instability wavepackets and acoustic radiation. *AIAA Paper 2013-2232*, 2013.

[93] C. K. W. Tam, M. Golebiowski, and J. M. Seiner. On the two components of turbulent mixing noise from supersonic jets. *AIAA Paper 96-1716*, 1996.

[94] J. Jeun and J. W. Nichols. Wavepacket modeling of turbulent jet noise generation using input-output analysis. *AIAA Paper 2017-3378*, 2017.

[95] D. P. Lockard and J. Casper. Permeable surface corrections for Ffowcs Williams and Hawkings integrals. *AIAA Paper 2005-2995*, 2005.

[96] V. Kopiev, S. Chernyshev, G. Faranosov, M. Zaitsev, and I. Belyaev. Correlations of jet noise azimuthal components and their role in source identification. *AIAA Paper 2010-4018*, 2010.

[97] D. Papamoschou. Wavepacket modeling of the jet noise source. *AIAA Paper 2011-2835*, 2011.

[98] C. Bogey, S. Barré, V. Fleury, C. Bailly, and D. Juvé. Experimental study of the spectral properties of near-field and far-field jet noise. *International Journal of Aeroacoustics*, 6(2):73–92, 2007.

[99] M. Zhang, P. Jordan, G. Lehnasch, A. V. G. Cavalieri, and A. Agarwal. Just enough jitter for jet noise. *AIAA Paper 2014-3061*, 2014.

[100] J. Jeun and J. W. Nichols. Non-compact sources of sound in high-speed turbulent jets using input-output analysis. *AIAA Paper 2018-####*, 2018.

[101] J. Jeun and J. W. Nichols. Modeling near-field wavepackets as acoustic sources in high-speed turbulent jets using input-output analysis. *In preparation*, 2018.

[102] A. Michalke. On the effect of spatial source coherence on the radiation of jet noise. *Journal of Sound and Vibration*, 55(3):377–394, 1977.

[103] D. G. Crighton and P. Huerre. Shear-layer pressure fluctuations and superdirective acoustic sources. *Journal of Fluid Mechanics*, 220:355–368, 1990.

[104] R. Serré, J.-C. Robinet, and F. Margnat. The influence of a pressure wavepacket′s characteristics on its acoustic radiation. *The Journal of the Acoustical Society of America*, 137(6):3178–3189, 2015.

[105] D. Papamoschou. Prediction of jet noise shielding. *AIAA paper 2010-653*, 2010.

[106] A. V. G. Cavalieri and A. Agarwal. Coherence decay and its impact on sound radiation by wavepackets. *Journal of Fluid Mechanics*, 748:399–415, 2014.

[107] C. K. W. Tam and F. Q. Hu. On the three families of instability waves of high-speed jets. *Journal of Fluid Mechanics*, 201:447–483, 1989.

[108] D. Obrist. Directivity of acoustic emissions from wave packets to the far field. *Journal of Fluid Mechanics*, 640:165–186, 2009.

[109] D. Papamoschou. On the connection between near and far pressure fields of a turbulent jet. *AIAA Paper 2018-1251*, 2018.

[110] J. Jeun, J. W. Nichols, and M. R. Jovanović. Input-output analysis of heated axisymmetric turbulent jets. *AIAA Paper 2016-2934*, 2016.

[111] E. Åkervik, U. Ehrenstein, F. Gallaire, and D. S. Henningson. Global two-dimensional stability measures of the flat plate boundary-layer flow. *European Journal of Mechanics-B/Fluids*, 27(5):501–513, 2008.

[112] C. K. W. Tam, K. Viswanathan, K. K. Ahuja, and J. Panda. The sources of jet noise: experimental evidence. *Journal of Fluid Mechanics*, 615:253–292, 2008.

[113] M. R. Jovanović and B. Bamieh. Modeling flow statistics using the linearized navier-stokes equations. In *Decision and Control, 2001. Proceedings of the 40th IEEE Conference on*, volume 5, pages 4944–4949. IEEE, 2001.

[114] R. Moarref and M. R. Jovanović. Model-based design of transverse wall oscillations for turbulent drag reduction. *Journal of Fluid Mechanics*, 707:205–240, 2012.

[115] A. Zare, M. R. Jovanović, and T. T. Georgiou. Colour of turbulence. *Journal of Fluid Mechanics*, 812:636–680, 2017.

[116] S. Beneddine, D. Sipp, A. Arnault, J. Dandois, and L. Lesshafft. Conditions for validity of mean flow stability analysis. *Journal of Fluid Mechanics*, 798:485–504, 2016.

Appendix A

Convergence test

A.1 Grid independence

Four different grid resolutions are tested to study the convergence of input-output analysis. For each resolution, grid points are distributed uniformly in the streamwise direction but are refined and stretched in the lateral direction to cluster grid points along the nozzle lipline. Figure A.1 shows singular values for the $M_j = 1.5$ supersonic jet for the four different grid resolutions. For sufficiently high grid resolutions, the singular values do not change significantly. We quantify this convergence in table A.1, which lists the magnitude of the largest singular value along with the percentage of sub-optimal energy (assuming white noise forcing). The number of grid points in the axial and radial directions are given by N_x and N_r, respectively, and these increase by a factor of 1.5 for each row. The final column lists the convergence factor defined as the ratio of the maximum gain to the maximum gain obtained on the previous, coarser mesh. For the higher mesh resolutions, we conclude that the results converge with respect to the mesh resolution. Throughout this dissertation we have used the grid with high resolution, unless otherwise stated.

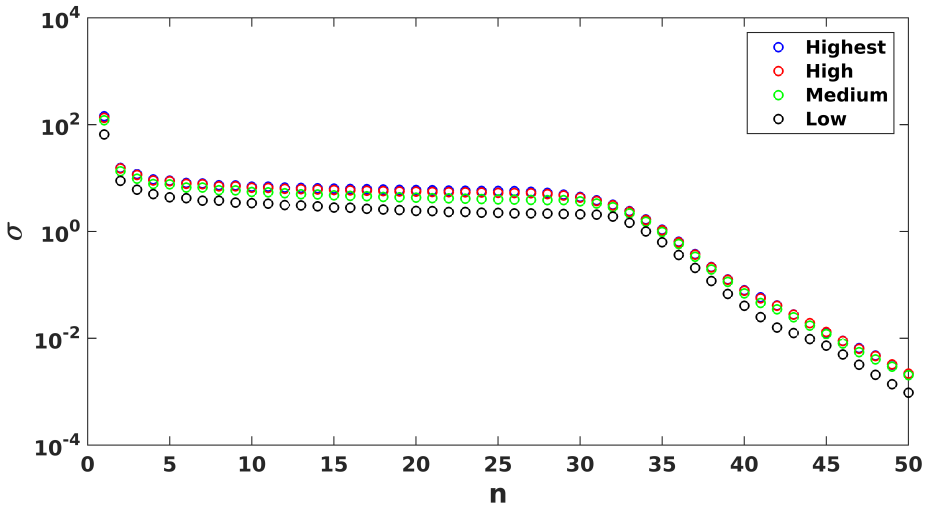

Figure A.1: Singular values using four different grid resolutions for the $M_j = 1.5$ supersonic jet at $St = 0.33$.

Table A.1: Optimal singular values, sub-optimal energy percentages, and convergence factors for four different grid resolutions for the $M_j = 1.5$ supersonic jet for forcing frequency $St = 0.33$.

Label	N_x	N_r	σ_1	$\frac{\sum \sigma^2_{sub-optimal}}{\sum \sigma^2_{total}}$	Convergence factor
low	256	128	6.56×10^1	0.0800	-
medium	384	192	1.21×10^2	0.0642	1.84
high	576	288	1.35×10^2	0.0732	1.12
highest	864	432	1.44×10^2	0.0711	1.06

Table A.2: Input and output domains and corresponding optimal singular values and sub-optimal energy percentages for the $M_j = 1.5$ supersonic jet for forcing frequency $St = 0.33$.

Label	x_{min}	x_{max}	r_{min}	r_{max}	σ_1	$\frac{\sum \sigma^2_{sub-optimal}}{\sum \sigma^2_{total}}$
I1	-10.0	60.0	0.29	2.90	1.35×10^2	0.0732
I2	-10.0	50.6	0.29	2.90	1.35×10^2	0.0669
I3	-10.0	30.2	0.29	2.90	1.35×10^2	0.0497
R1	-10.0	60.0	8.70	39.2	1.35×10^2	0.0732
R2	-10.0	50.6	8.70	39.2	1.15×10^2	0.0874
R3	-10.0	60.0	8.70	14.9	8.34×10^1	0.0544
R4	-10.0	50.6	8.70	14.9	8.09×10^1	0.0524
R5	-10.0	30.2	8.70	39.2	5.26×10^1	0.2181

A.2 Domain independence

To investigate the dependence of gains on the input and output domain sizes, we consider five different output domains and three different input domains. These domains are summarized in table A.2 and displayed graphically in figure A.2. The input domains (I1-I3) are restricted to the region close to the jet shear layer, whereas the output domains (R1-R5) are restricted to the far-field region. As mentioned in chapter 2, the input forcing is selected to choose velocity through the matrix B, while the matrix C selects pressure from the state vector. Specifically, the input and output domains defined in chapter 2 and used in chapter 3 correspond here to I1 and R1, respectively. Physically, this choice was made to capture the influence of velocity fluctuations inside the full jet on the far-field pressure fluctuations. By systematically varying the input and output domain sizes, however, we assess the robustness of our results to this particular choice.

The three different input domains were tested using the same output domain R1. For the optimal mode, figure A.3 shows that input-output analysis produces almost the same

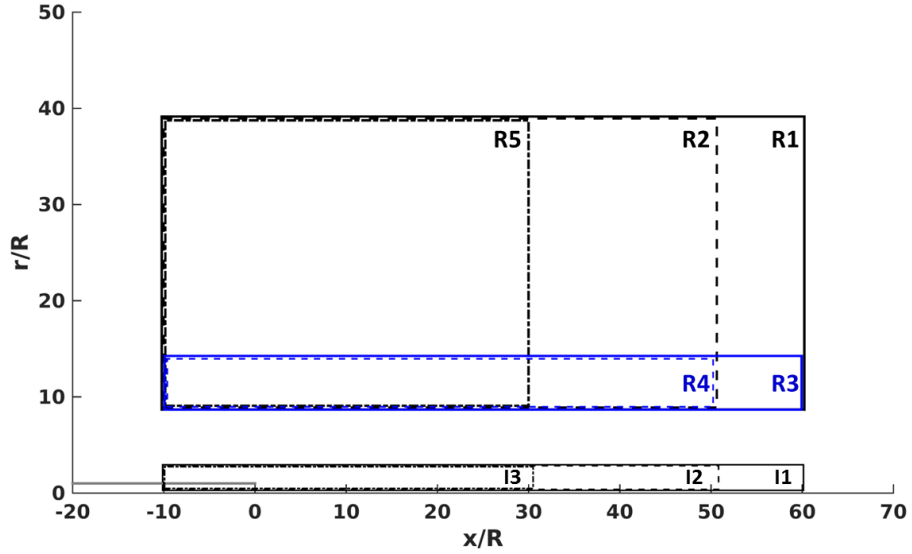

Figure A.2: Graphical representation of various input and output domains.

results regardless of the input domain sizes. Since the input mode shown in figure 3.3(a) fully resides inside all three input domains, this is not surprising. Because the sub-optimal modes extend farther downstream as mode number increases, the dropoff in singular values is affected by the length of the input domain.

The effect of the output domain size was examined in terms of the gains for the $M_j = 1.5$ jet. Each case used I1 as the input domain. As expected, output domains that extend farther in the lateral or the axial directions result in larger amplification than smaller domains. In figure A.4, however, the gains for output domain having the same axial extent follow the same curve, shifted vertically by a relatively constant offset. Again, the dropoff in singular values at high mode numbers is determined by the axial length of the output domain. Furthermore, as figure A.5 shows, the shape of the output modes remains unchanged in the areas where the output domains overlap. This means that the mode selected is not sensitive to the details of the chosen output domain. Rather, we observe the same physical mode through different windows.

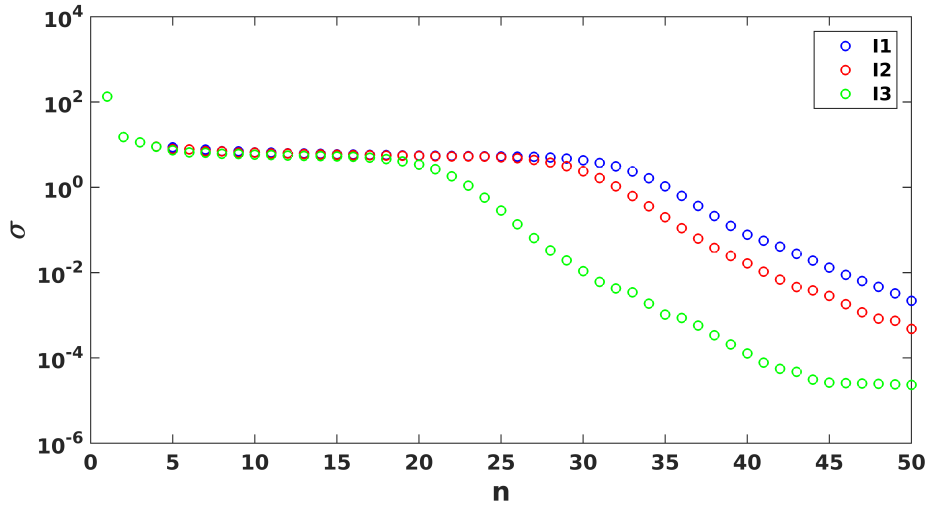

Figure A.3: Gains for various input domains for the $M_j = 1.5$ supersonic jet for forcing frequency $St = 0.33$.

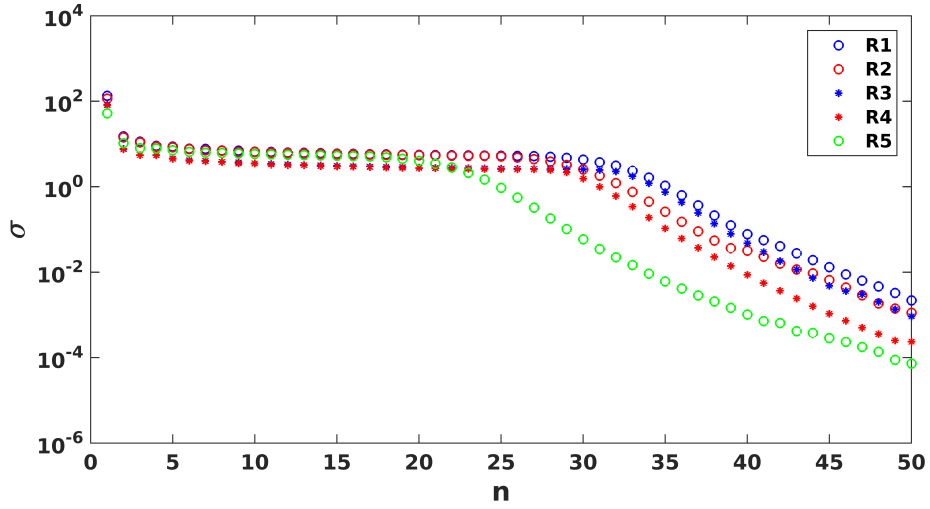

Figure A.4: Gains for various output domains for the $M_j = 1.5$ supersonic jet for forcing frequency $St = 0.33$.

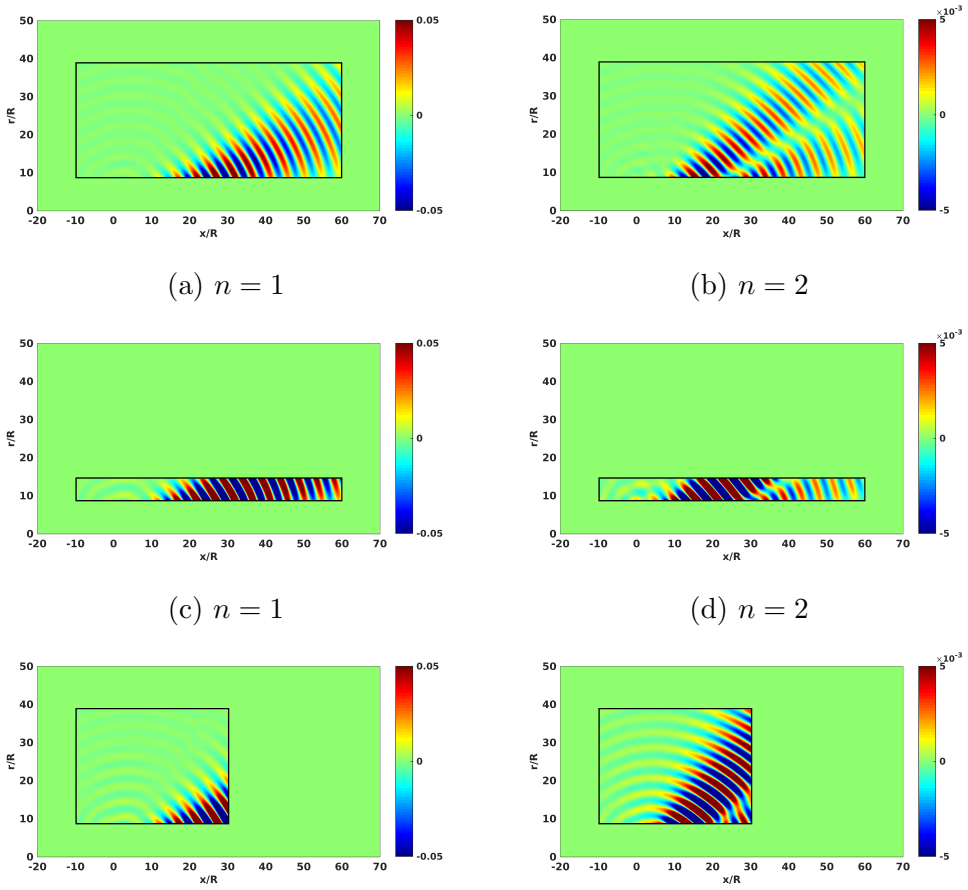

(a) $n = 1$ (b) $n = 2$

(c) $n = 1$ (d) $n = 2$

(e) $n = 1$ (f) $n = 2$

Figure A.5: The optimal and the first sub-optimal output modes of the $M_j = 1.5$ supersonic jet for forcing frequency $St = 0.33$ with the output domains (top) R1, (middle) R3, and (bottom) R5. (a,c,e) $n = 1$. (b,d,f) $n = 2$.

Appendix B

Verification of the linearized FW-H solver

B.1 Case 1: Monopole

In this appendix we verify the FW-H formulation that are directly implemented within input-output analysis framework as a linear operator inside the matrix C, by testing simple cases for which an analytic solution exists. We first consider a point monopole source located at the origin. The far-field pressure at r radiated from the source is exactly written as:

$$\frac{p_{exact}(r,\omega)}{p_{ref}} = \frac{e^{-\mathrm{i}kr}}{4\pi r}, \tag{B.1}$$

using the free-space Green's function given in equation (4.7). Being consistent with notations used in section 4.2.1, the distance between the source $\boldsymbol{y}$ and the observer $\boldsymbol{x}$ is given by $r = |\boldsymbol{x} - \boldsymbol{y}|$. The reference pressure is set to be $p_{ref} = 10^{-6}$. Furthermore, ω represents the frequency and k denotes the wavenumber such that $k = 2\pi/\lambda$. The wavelength λ is given as $1D$ and the speed of sound $c = 1/1.5 = 0.6667$. Note that sound

radiated from a monopole is omnidirectional so the exact solution above is independent of an azimuthal angle θ. The velocity field of a monopole source is obtained by substituting this into the conservation of momentum, and it is then used in the linearized FW-H formulation given in equation (4.6).

We place a straight cylindrical FW-H projection surface so that its axis lies along the x-axis as shown in figure B.1. We choose the projection surface with radius $R_s = 3D$, which extends from $x = -15D$ to $15D$ so that its length $L_s = 30D$. The number of grid points in the axial, radial, and azimuthal directions are given by $N_x = 481$, $N_r = 125$, and $N_\theta = 64$, respectively. The grid are uniform in the streamwise and azimuthal directions but stretched in the radial direction. In fact, the projection surface is discretized so that the grids exactly match to those we used in input-output analysis and an LES for the $M_j = 0.9$ subsonic jet described in chapter 5. Meanwhile, to assess the effects of open outflow disk, we test FW-H surfaces equipped with and without end-caps [89], when computing the far-field pressure fields. The results are summarized in figure B.2.

In figure B.2 the blue solid lines correspond to the exact far-field sound pressure, whereas red symbols represent solutions computed using the FW-H solver implemented as a linear operator. If they are left open, the numerical solutions at small radiation angles ($-20^\circ < \phi < 20^\circ$ and $160^\circ < \phi < 220^\circ$) deviate from the exact solution but agree fairly well elsewhere as shown in figure B.2(a). In contrast, by closing the outflow disks the projection surface, figure B.2(b) reproduces the exact solution at almost all observer angles.

Now, a monopole source is still placed at the origin, but the FW-H projection is centered at $x/D = 10D$ to mimic the flow configuration of turbulent jets we consider in this dissertation. Considering that in input-output analysis the numerical domain extends from $x/R = -20$ to 70, while turbulent jets enter to a quiescent fluid at $x/R =$

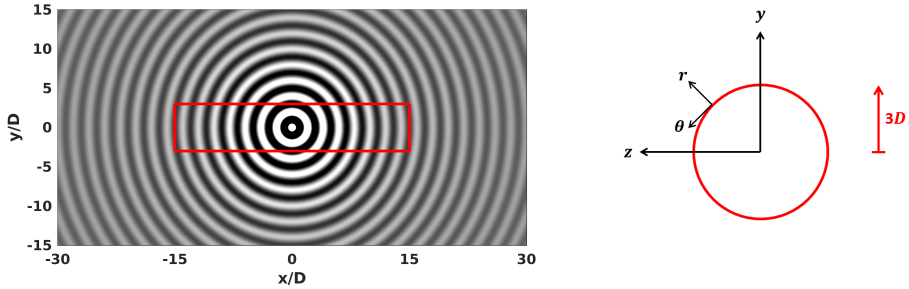

(a) (b)

Figure B.1: (a) A straight cylindrical FW-H surface (a red-outlined rectangle) placed in a monopole field on xy-plane cross-section at $z = 0$. The length of the projection surface is $30D$, and the diameter of its cross-section is $3D$. (b) A cross-sectional view of the projection surface on yz-plane is zoomed-in. The azimuthal angle θ is measured in a counter-clockwise direction.

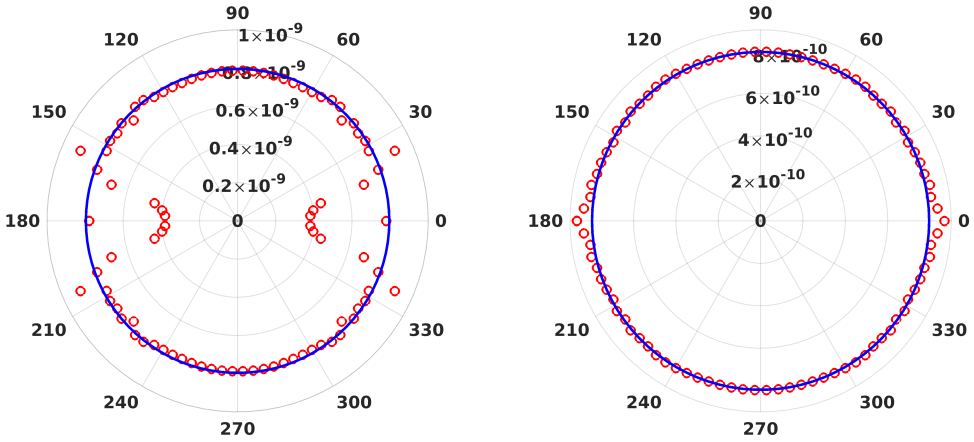

(a) Open outflow disks (b) Closed outflow disks

Figure B.2: Acoustic far-field measured at 100 diameters away from a monopole centered at the origin using the projection surfaces whose outflow disks are (a) left open and (b) closed with end-caps, respectively. In each figure blue solid line represents the exact solution, and red markers are computed using an FW-H formulation implemented inside input-output analysis framework.

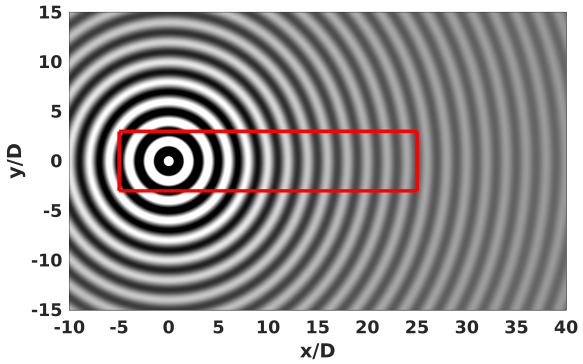

Figure B.3: A straight cylindrical FW-H surface (a red-outlined rectangle) is now asymmetric about a point monopole centered at the origin. The length and diameter of the projection surface remain unchanged as in the previous case.

0, new projection surface is not symmetric any longer about an acoustic source in streamwise direction. The schematic view of a point monopole source located at the origin and an asymmetric projection surface is given in figure B.3. Under this condition, the linearized FW-H solver recovers the far-field pressure very closely to the analytic solution at radiation angles of our interests as shown in figure B.4 regardless of the types of outflow disks. We lose the symmetry of the pressure field and compromise some accuracy at small observer angles, but the results are still within acceptable accuracy at angles of our interest.

B.2 Case 2: Dipole

As seen in equation 4.6 the far-field sound is represented by surface integrals of monopole and dipole sources. In this sense we also test the linearized FW-H solver with sound radiation from a dipole source. We consider a dipole source located along the y-axis as shown in figure B.5. The analytic solution for the pressure field is then derived by

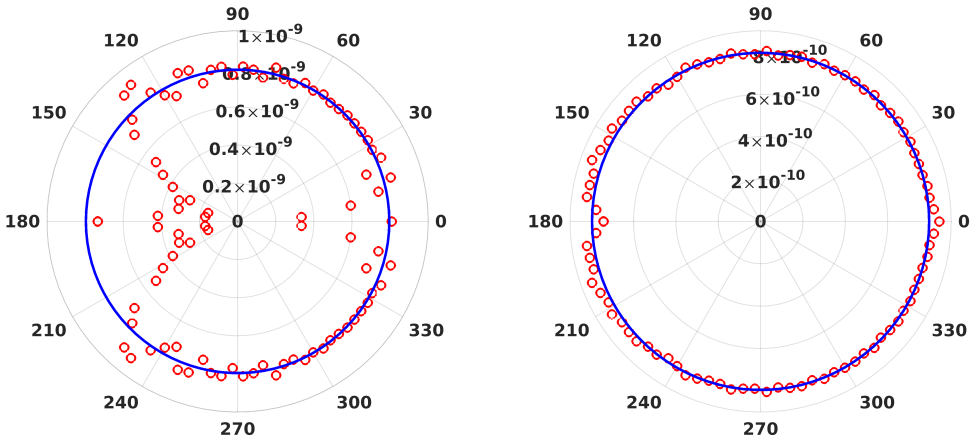

(a) Open outflow disks

(b) Closed outflow disks

Figure B.4: Acoustic far-field measured at 100 diameters away from a monopole placed at 5 diameters away from the left-end of the FW-H projection surface. Pressures (red markers) are predicted using (a) open and (b) closed outflow disks, respectively, and compared to the analytic solution represented by blue solid lines.

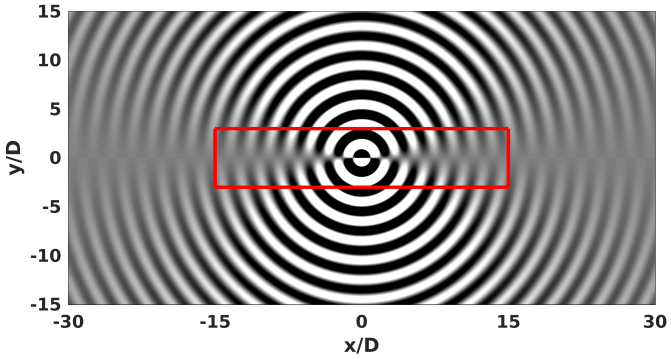

Figure B.5: A straight cylindrical FW-H surface for sound radiation of a dipole centered at the origin.

differentiating the free-space Green's function (4.7) in y such as:

$$\frac{p_{exact}(r,\omega)}{p_{ref}} = \frac{\partial G}{\partial y} = \frac{\partial G}{\partial r}\frac{\partial r}{\partial y} = \frac{e^{-\mathrm{i}kr}}{4\pi r}\left(-\mathrm{i}k - \frac{1}{r}\right)\frac{\partial r}{\partial y}. \tag{B.2}$$

In cylindrical coordinates we use here, $\frac{\partial r}{\partial y}$ is conveniently computed as $\frac{y}{r}$. The reference pressure remain unchanged as $p_{ref} = 10^{-6}$. The wavelength λ is still given as $1D$, but at this time we change the speed of sound to $c = 1/0.9 = 1.111$.

We use the same FW-H projection surface, which was used in the previous section to test sound radiation from a monopole acoustic source. Again, a cylindrical projection surface may be either open or closed at $x/D = 30$. The resulting dipole fields are compared with the exact solution (denoted by blue solid lines) in figure B.6. The far-field acoustic predictions in all cases show reasonably good agreements with the exact solution except for the observers very close to the x-axis.

Similarly in the case of a point monopole, we investigate the effect of asymmetric projection surface about a point dipole centered at the origin. In figure B.7, the predictions by the linearized FW-H solver are in good agreement with the analytic solution. Errors around upstream jet centerline are decreased significantly with end-caps

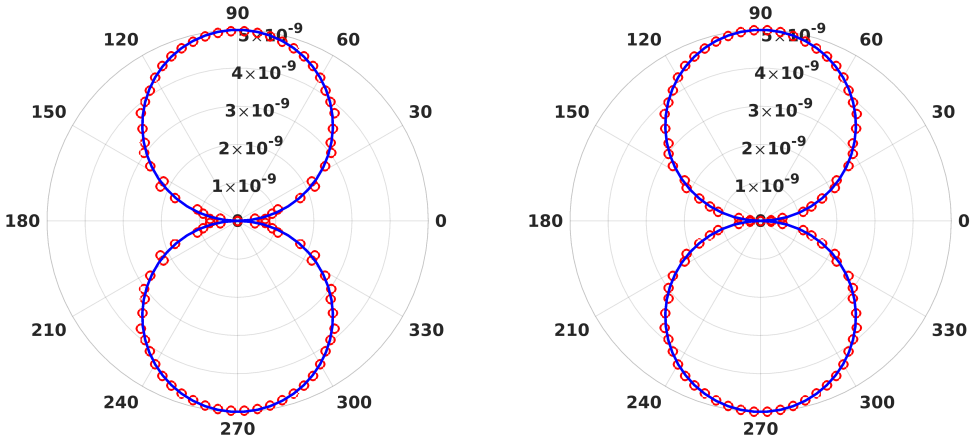

(a) Open outflow disks

(b) Closed outflow disks

Figure B.6: Dipole field is measured in terms of pressure at 100 diameters away from the origin. The outflow disks of the projection surfaces are (a) left open and (b) closed with end-caps. In each figure blue solid line represents the exact solution, and red markers are computed using the FW-H formulation implemented within input-output analysis framework.

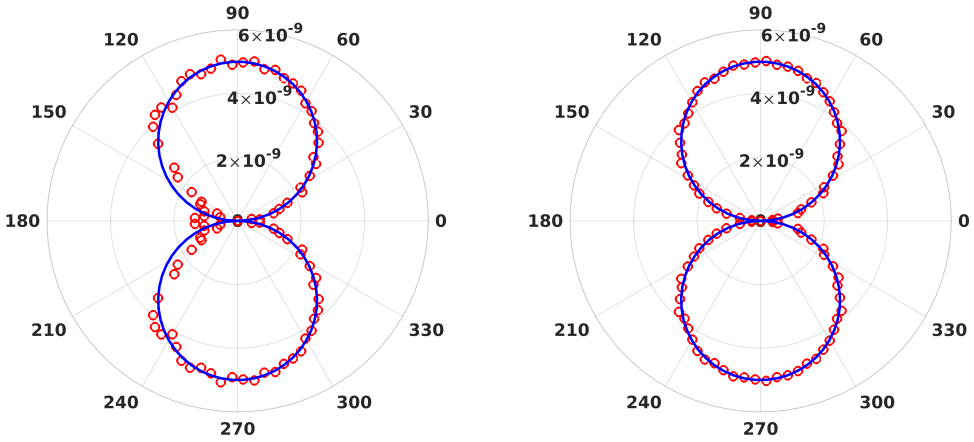

(a) Open outflow disks (b) Closed outflow disks

Figure B.7: Acoustic far-field measured at 100 diameters away from a dipole placed at 5 diameters away from the left-end of the FW-H projection surface along y-axis. Pressures (red markers) are predicted using (a) open and (b) closed outflow disks, respectively, and compared to the analytic solution represented by blue solid lines. Equipped with end-caps at both ends of the projection surface, the predictions are significantly enhanced.

at $x/D = -5$ and $x/D = 25$ even with the asymmetric projection surface.

In sum, for turbulent jets, regions of low radiation angles correspond to regions that are close to the jet centerline, and we do not expect much output sound there. Based on the tests given in the previous and the present sections, we thus conclude that for a long and lean enough cylindrical projection surface, the FW-H formulation implemented inside the input matrix C would work even without end-cap treatments. From this, a linearized FW-H solver employs an open FW-H projection surface, for simplicity. The LES database projections in chapters 3–5 are also performed with the same type of projection surface.